TiO$_2$-Based Nanomaterials: Design, Synthesis, and Applications
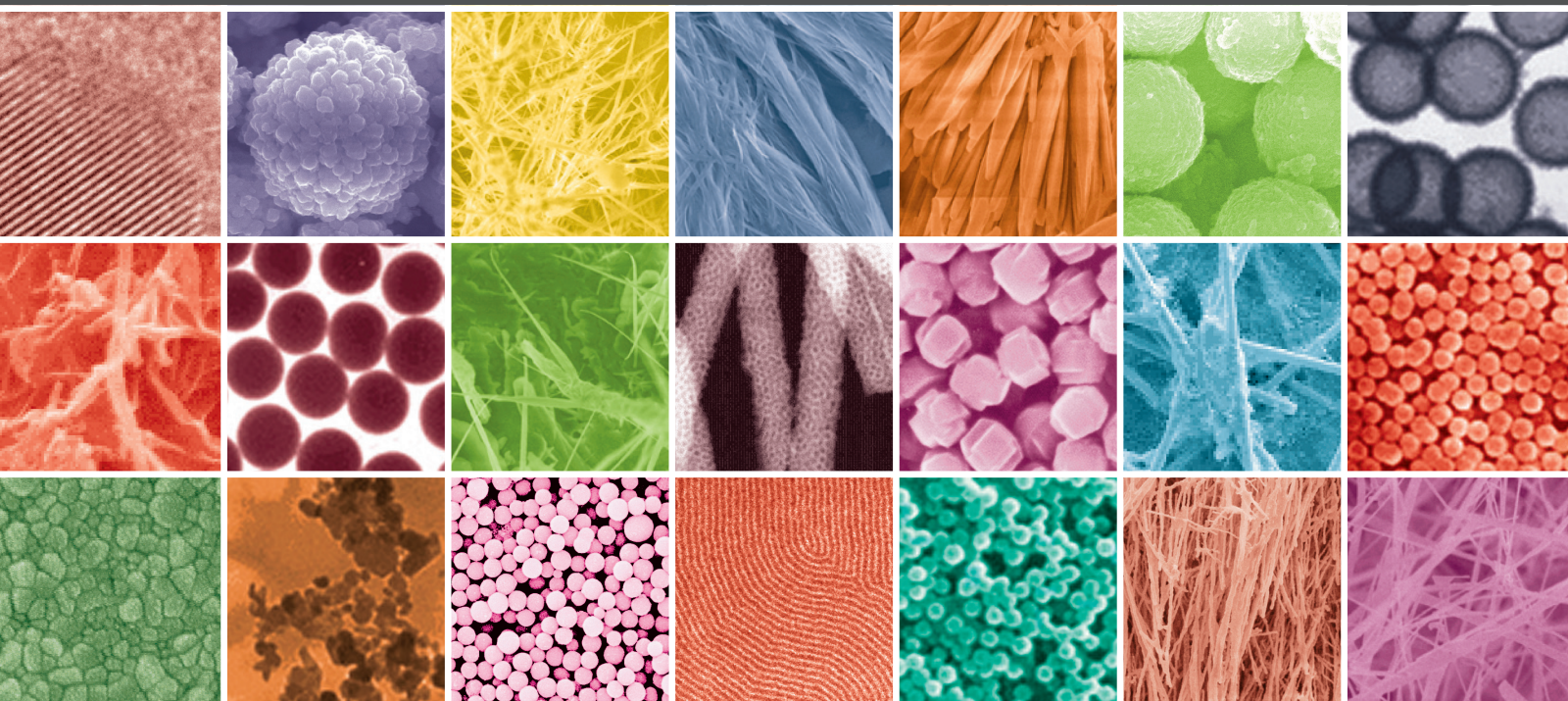
Guest Editors: Yuekun Lai, Luning Wang, Dawei Liu, Zhong Chen, and Changjian Lin

TiO$_2$-Based Nanomaterials: Design, Synthesis, and Applications

TiO$_2$-Based Nanomaterials: Design, Synthesis, and Applications

Guest Editors: Yuekun Lai, Luning Wang, Dawei Liu, Zhong Chen, and Changjian Lin

Huaiyu Shao, Japan
Prashant Sharma, USA
Donglu Shi, USA
Bhanu P. Singh, India
Surinder Singh, USA
Vladimir Sivakov, Germany
Yanlin Song, China
Ashok Sood, USA
Marinella Striccoli, Italy
Jing Sun, China
Xuping Sun, Saudi Arabia
A. K. Sundramoorthy, USA
Sabine Szunerits, France
Nyan-Hwa Tai, Taiwan

Bo Tan, Canada
Ion Tiginyanu, Moldova
Valeri P. Tolstoy, Russia
M. S. Toprak, Sweden
Ramon Torrecillas, Spain
Takuya Tsuzuki, Australia
Tamer Uyar, Turkey
Bala Vaidhyanathan, UK
Luca Valentini, Italy
Rajender S. Varma, USA
Antonio Villaverde, Spain
Ajayan Vinu, Australia
Shiren Wang, USA
Yong Wang, USA

Ruibing Wang, Macau
Magnus Willander, Sweden
Ping Xiao, UK
Zhi Li Xiao, USA
Yangchuan Xing, USA
Doron Yadlovker, Israel
Piaoping Yang, China
Yoke K. Yap, USA
Ramin Yousefi, Iran
William W. Yu, USA
Kui Yu, Canada
Renyun Zhang, Sweden

Contents

Editorial

TiO$_2$-Based Nanomaterials: Design, Synthesis, and Applications

Yuekun Lai,[1] Luning Wang,[2] Dawei Liu,[3] Zhong Chen,[4] and Changjian Lin[5]

[1]*National Engineering Laboratory of Modern Silk, College of Textile and Clothing Engineering, Soochow University, Suzhou 215123, China*

[2]*School of Materials Science and Engineering, University of Science and Technology Beijing, Beijing 100083, China*

[3]*Kazuo Inamori School of Engineering, Alfred University, Alfred, NY 14802, USA*

[4]*School of Materials Science and Engineering, Nanyang Technological University, 50 Nanyang Avenue, Singapore 639798*

[5]*State Key Laboratory of Physical Chemistry of Solid Surfaces, College of Chemistry and Chemical Engineering, Xiamen University, Xiamen 361005, China*

Correspondence should be addressed to Yuekun Lai; yklai@suda.edu.cn

Nanostructure materials with specific properties or activities are not expected in bulk phase and have already led to a breakthrough in various fields of research and application. Within these nanomaterials, TiO$_2$-based nanomaterials attracted great interest and intensive researches due to their merits of high specific surface area, proper electronic band structure, high quantum efficiency, chemical innerness, and stability (Figure 1). Over the past decades, derivations from TiO$_2$-based nanostructures materials constructed by various techniques, for example, assisted-template method [1, 2], hydrothermal treatment [3–5], and electrochemical anodic oxidation [6–9], have extensively been investigated for many potential applications, including environmental photocatalysis/adsorbent, dye-sensitized solar cell, and biomedical implants [10–13].

This special issue is focused on the rational design, environmental-friendly synthesis strategies and promising applications based on hierarchical TiO$_2$-based nanostructured materials. Some of researched works collected by this issue are as follows.

Z. H. Luo et al. in "Correlation between the Photocatalytic Degradability of PAHs over Pt/TiO$_2$-SiO$_2$ in Water and Their Quantitative Molecular Structure" reported photocatalytic character and kinetics of six polycyclic aromatic hydrocarbons (PAHs) in Pt/TiO$_2$-SiO$_2$ suspension. The results show that the degradation of high molecular weight (HMW) PAHs, PYR, BaP, and DahA were accelerated significantly in the presence of Pt/TiO$_2$-SiO$_2$, while the degradation efficiency of low molecular weight (LMW) PAHs, NP, FL, and PHE were inhibited under the same experimental conditions. More impressing, the photocatalytic degradability of 67 PAHs was predicted and verified in a way by comparing against the maximum GAP of PAHs that could be photocatalytically degraded and the minimum GAP of PAHs that could not be photocatalytically degraded in this study.

A. Asghar et al. in "Comparison of Adsorption Capability of Activated Carbon and Metal Doped TiO$_2$ for Geosmin and 2-MIB Removal from Water" presented a facile method to synthesis of the Fe doped and Pt doped TiO$_2$ nanoparticles. Compared with granular activated carbon which is the most widely used water purification, such doped TiO$_2$ nanoparticles demonstrated their potential application for Geosmin and 2-MIB adsorbent because of their smaller size, larger surface, and more active adsorption site. The present experimental results suggest that metal doped titania nanoparticles demonstrate significant adsorption potential for the accelerated removal for earthy-musty odor producing compounds in the drinking water.

Y. H. Lin et al. in "Facile Synthesis and Characterization of N-Doped TiO$_2$ Photocatalyst and Its Visible-Light Activity for Photo-Oxidation of Ethylene" adopted a facile wet chemical method to construct highly photoactive nitrogen doped TiO$_2$ (N-TiO$_2$) powders with visible responsive capability, and utilized the N-TiO$_2$ powder for the visible-light
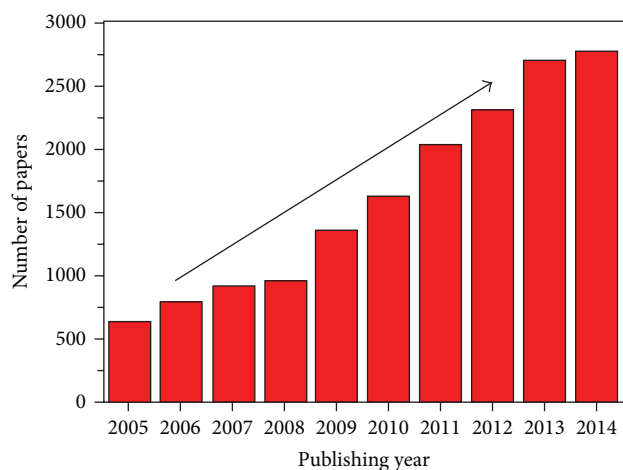
Figure 1: The number of papers published with "nano∗ and TiO$_2$" or "nano∗ and titanate" as the keywords in the article title from 2005 to 2014.

photocatalytic degradation of ethylene pollutant. Compared to commercial P25, the photocatalytic results demonstrated that the TiO$_2$ powder with or without N-doping was a higher efficient photocatalyst. Moreover, the author deeply studied and discussed the photocatalytic mechanism under visible-light irradiation.

M. Fujita et al. in "Preparation of Oleyl Phosphate-Modified TiO$_2$/Poly(methyl methacrylate) Hybrid Thin Films for Investigation of Their Optical Properties" employed oleylphosphate modified TiO$_2$ nanoparticles to prepare polymethylmethacrylate- (PMMA-) based hybrid materials via the ex situ route. The hydrophobic modification of TiO$_2$ nanoparticle surfaces through stable Ti-O-P bonds was verified to effectively suppress the aggregation of TiO$_2$ nanoparticle in polymer matrices to achieve high refractive index. The composite thin film exhibited the highest refractive index ($n = 1.86$) with 20 vol% content of TiO$_2$ and still kept excellent optical transparency even with a TiO$_2$ content up to 70 mass%. We believe that the strategy with the ex situ route for preparation of TiO$_2$/polymer hybrids after surface modification enables us to control the refractive indices easier than the in situ route and would have huge impact in optical films related to TiO$_2$ nanoparticles.

W. Guan et al. in "Preparation and Photocatalytic Performance of Nano-TiO$_2$ Codoped with Iron III and Lanthanum III" synthesized metal (Fe^{3+}, La^{3+}) doping nanoscale titanium dioxide (nano-TiO$_2$) via sol-gel method to improve its photocatalytic activity and utilization of visible light. The modified sol-gel method was verified to be an effective technique for codoping the TiO$_2$ lattice with Fe^{3+} and La^{3+} and restricted the growth of doped TiO$_2$ crystal. Furthermore, the catalytic mechanism which was revealed for metal doping of nano-TiO$_2$ was proposed. Codoping of nano-TiO$_2$ with the tombarthite metal mixture had a synergistic effect on the photodegradation reaction of methyl orange. The codoped nano-TiO$_2$ exhibited superior photocatalytic activity compared to the sum of the single-doped nano-TiO$_2$ samples. This work provided a potentially attractive and effective approach for TiO$_2$ photocatalysis to resolve the environmental problem.

X. H. Dai et al. in "Attenuating Immune Response of Macrophage by Enhancing Hydrophilicity of Ti Surface" constructed Ti samples with high contrast of surfaces hydrophilicity. Experimental results showed that highly hydrophilic Ti surface (Ti-H$_2$O$_2$) yielded good biocompatibility and less multinucleated cells formation in vitro. The secretion of TNF-α and IL-10 quantified by ELISA revealed that more hydrophilic Ti surface leads to lower activation status of macrophages. Moreover, the NF-κB assay revealed that NF-κB/TNF-α might be the possible mechanism underlying behind surface hydrophilicity modulating immune response. All these results suggested that hydrophilic Ti surface might be more favorable in attenuating macrophage immune response via NF-κB signaling, which may provide new insight in surface-designing of novel implant devices.

Acknowledgments

Yuekun Lai
Luning Wang
Dawei Liu
Zhong Chen
Changjian Lin

References

[1] J. C. Hulteen and C. R. Martin, "A general template-based method for the preparation of nanomaterials," *Journal of Materials Chemistry*, vol. 7, no. 7, pp. 1075–1087, 1997.

[2] M. S. Sander, M. J. Côté, W. Gu, B. M. Kile, and C. P. Tripp, "Template-assisted fabrication of dense, aligned arrays of titania nanotubes with well-controlled dimensions on substrates," *Advanced Materials*, vol. 16, no. 22, pp. 2052–2057, 2004.

[3] D. V. Bavykin, J. M. Friedrich, and F. C. Walsh, "Protonated titanates and TiO$_2$ nanostructured materials: synthesis, properties, and applications," *Advanced Materials*, vol. 18, no. 21, pp. 2807–2824, 2006.

[4] X. Sun and Y. Li, "Synthesis and characterization of ion-exchangeable titanate nanotubes," *Chemistry A: European Journal*, vol. 9, no. 10, pp. 2229–2238, 2003.

[5] T. Kasuga, M. Hiramatsu, A. Hoson, T. Sekino, and K. Niihara, "Formation of titanium oxide nanotube," *Langmuir*, vol. 14, no. 12, pp. 3160–3163, 1998.

[6] C. A. Grimes, "Synthesis and application of highly ordered arrays of TiO$_2$ nanotubes," *Journal of Materials Chemistry*, vol. 17, no. 15, pp. 1451–1457, 2007.

[7] P. Roy, S. Berger, and P. Schmuki, "TiO$_2$ nanotubes: Synthesis and applications," *Angewandte Chemie—International Edition*, vol. 50, no. 13, pp. 2904–2939, 2011.

[8] J.-Y. Huang, K.-Q. Zhang, and Y.-K. Lai, "Fabrication, modification, and emerging applications of TiO$_2$ nanotube arrays

by electrochemical synthesis: a review," *International Journal of Photoenergy*, vol. 2013, Article ID 761971, 12 pages, 2013.

[9] Ki. Lee, A. Mazare, and P. Schmuki, "One-dimensional titanium dioxide nanomaterials: nanotubes," *Chemical Reviews*, vol. 114, no. 19, pp. 9385–9454, 2014.

[10] Y. Lai, L. Sun, Y. Chen, H. Zhuang, C. Lin, and J. W. Chin, "Effects of the structure of TiO$_2$ nanotube array on Ti substrate on its photocatalytic activity," *Journal of the Electrochemical Society*, vol. 153, no. 7, pp. D123–D127, 2006.

[11] Y.-K. Lai, J.-Y. Huang, H.-F. Zhang et al., "Nitrogen-doped TiO$_2$ nanotube array films with enhanced photocatalytic activity under various light sources," *Journal of Hazardous Materials*, vol. 184, no. 1–3, pp. 855–863, 2010.

[12] M. Ye, J. J. Gong, Y. K. Lai, C. J. Lin, and Z. Q. Lin, "High-efficiency photoelectrocatalytic hydrogen generation enabled by palladium quantum dots-sensitized TiO$_2$ nanotube arrays," *Journal of the American Chemical Society*, vol. 134, no. 38, pp. 15720–15723, 2012.

[13] Y. K. Lai, L. X. Lin, F. Pan et al., "Bioinspired patterning with extreme wettability contrast on TiO$_2$ nanotube array surface: a versatile platform for biomedical applications," *Small*, vol. 9, no. 17, pp. 2945–2953, 2013.

Research Article

Correlation between the Photocatalytic Degradability of PAHs over Pt/TiO$_2$-SiO$_2$ in Water and Their Quantitative Molecular Structure

Zhao-hui Luo,[1] Chuan-ling Wei,[1] Nan-nan He,[1] Zhi-guo Sun,[1] Hui-xin Li,[1] and Dan Chen[2]

[1]*College of Resources and Environmental Science, Nanjing Agricultural University, Nanjing 210095, China*
[2]*Key Laboratory of Efficient Irrigation-Drainage and Agricultural Soil-Water Environment in Southern China (Ministry of Education),
 College of Water Conservancy and Hydropower Engineering, Hohai University, Nanjing 210098, China*

Correspondence should be addressed to Zhao-hui Luo; lzhui@njau.edu.cn

The correlation between the photocatalytic degradability of polycyclic aromatic hydrocarbons (PAHs) over Pt/TiO$_2$-SiO$_2$ in water and their quantitative molecular structure was studied. Six PAHs, namely, naphthalene, fluorene, phenanthrene, pyrene, benzo[a]pyrene, and dibenzo[a,h]anthracene, were tested in Pt/TiO$_2$-SiO$_2$ suspension under UV irradiation. The results showed that the degradation efficiencies of the higher molecular weight PAHs were enhanced significantly in the presence of Pt/TiO$_2$-SiO$_2$, while the degradation efficiencies of the lower molecular weight PAHs were decreased in the presence of Pt/TiO$_2$-SiO$_2$. Both the photolysis and photocatalysis of all PAHs fit the pseudo-first-order equation very well, except FL. Quantitative analysis of molecular descriptors of energy of the highest occupied molecular orbital (E_{homo}), energy of the lowest unoccupied molecular orbital (E_{lumo}), and the difference between E_{lumo} and E_{homo}, GAP (GAP $= E_{\text{lumo}} - E_{\text{homo}}$), suggested that the GAP was significant for predicting a PAHs' photocatalytic degradability. Through comparison against the maximum GAP (7.4529 eV) of PAHs (dibenzo[a,h]anthracene) that could be photocatalytically degraded and the minimum GAP (8.2086 eV) of PAHs (pyrene) that could not be photocatalytically degraded in this study, the photocatalytic degradability of 67 PAHs was predicted. The predictions were partly verified by experimental photocatalytic degradation of anthracene and Indeno[1.2.3.cd]pyrene.

1. Introduction

Polycyclic aromatic hydrocarbons (PAHs) are a large group of organic compounds with two or more fused aromatic rings. PAHs are produced mainly by the incomplete combustion of fossil fuels. They are widespread contaminants found in natural bodies of water [1, 2]. Many PAHs have a variety of mutagenic and carcinogenic effects in organisms. It is reported that low molecular weight PAHs (LMW PAHs, compounds containing three or less fused benzene rings) are more susceptible to biodegradation, while high molecular weight PAHs (HMW PAHs, compounds containing four or more fused benzene rings), which are highly mutagenic and carcinogenic, are more recalcitrant [3, 4]. Therefore, it is difficult to eliminate PAHs through traditional biological water treatment [5].

An advanced oxidation technique called TiO$_2$-photocatalyzed degradation has attracted attention as a method of eliminating a variety of organic compounds because the process can achieve effective mineralization under mild temperature and pressure conditions [6, 7]. Some biorefractory substances, such as norfloxacin [8], dyes [9–11], and 4-chlorocatechol [12], have been reported to degrade successfully using this technique. Some PAHs were also reported to be photocatalytically degraded successfully with the presence of TiO$_2$ in aqueous environment. Wen et al. [13] examined the photocatalytic degradation of pyrene (PYR) that preadsorbed onto TiO$_2$ surface before UV irradiation. They found that the pH of the dispersion and the ratio of PYR/TiO$_2$: water had little effect on the photooxidation rate of PYR, while the extent of surface coverage and the addition of Fe^{3+} affected it greatly. Lin and Valsaraj [14]

studied the degradation of PYR and phenanthrene (PHE) in a dilute water stream by an annular photocatalytic reactor with TiO_2 immobilized on a quartz tube. They found that both PAHs degrade to CO_2 and H_2O in the presence of quinone. Dass et al. [15] found that acenaphthene, anthracene (AN), fluorine (FL), and naphthalene (NP) undergo efficient photocatalytic oxidation in aqueous suspensions of TiO_2 upon irradiation with a 500 W super-high pressure mercury lamp as well as sunlight. Lair et al. [16] studied the degradation of NP in water by photocatalysis in UV-irradiated TiO_2 suspensions. They found that the optimum TiO_2 was $2.5\,g\,L^{-1}$. They also observed that CO_3^{2-} strongly inhibited NP adsorption and removal, while pH had insignificant effect upon the NP removal, and temperature slightly accelerated the NP degradation. Through the identification of the main intermediates of NP photodegradation, they proposed that NP degraded by oxygenated radicals and by direct oxidation in the holes formed. Woo et al. [17] investigated the effects of acetone on the photocatalytic degradation efficiency and pathways of NP, acenaphthylene (ACN), PHE, AN, and benzo[a]anthracene in synthetic water. They observed that PAHs photolysis generated toxic intermediate products, especially in the case of ACN and PHE. However, all PAHs complete detoxification was achieved in a 24 h of UV/TiO_2 system by $100\,mg\,L^{-1}$ of catalyst. They also found that acetone enhanced PAHs degradation, but 16% acetone addition significantly altered the degradation pathway of NP and ACN. Vela et al. [18] investigated the removal of a mixture of six PAHs (BaP, benzo[b]fluoranthene, benzo[ghi]perylene, benzo[k]fluoranthene, fluoranthene, and InP) from groundwater by ZnO and TiO_2 photocatalysis in tandem with $Na_2S_2O_8$ as oxidant under natural sunlight. The photocatalytic experiments showed that the addition of photocatalyst strongly improved the elimination of PAHs in comparison with photolytic tests. The time required for 90% degradation in the condition of the study was in the ranges 7–15 min and 18–76 min for ZnO and TiO_2 systems, respectively.

Although the TiO_2-photocatalyzed degradation technology has been extensively investigated in pollutant treatment in the last two decades, its practical application is limited because of the disadvantages of TiO_2, such as its low surface area, low adsorbability for pollutants, fast recombination of photogenerated electrons-hole pair, the maximum absorption in the ultraviolet light region, and the difficulty of separation from treated water [19, 20]. Numerous approaches, such as composite semiconductor, noble metal loading, ion doping, nanotube formation, and sensitization, have been used to modify TiO_2 to overcome the above disadvantages [21–24]. SiO_2 is one of the most popular coupled materials in composite semiconductors. Mixed TiO_2-SiO_2 has been reported to be three times more photoactive than TiO_2 alone [25]. The addition of SiO_2 particles not only alters the size and shape of the TiO_2 particles, but also increases the thermal stability and adsorbability of TiO_2 particles [26, 27]. Platinum (Pt) is one of the most common noble metals loading on TiO_2. Ishibai et al. [28] reported their Pt-TiO_2 possessed high photocatalytic activity under visible light irradiation, as well as under UV light irradiation.
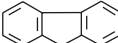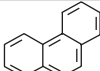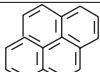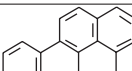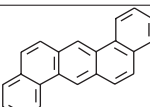
They suggested that the surface complex formation associated with Ti-O-Pt chemisorption dominated the visible light reactivity. Devipriya et al. [29] prepared Pt-TiO_2 and immobilized it on ceramic tiles. They found that the catalyst was effective for the solar photocatalytic removal of chemical and bacterial pollutants from water. The optimum loading of Pt on TiO_2 was found to be 0.5%. Ahmed et al. [30] reported that their Pt-TiO_2 samples are more active than the corresponding bare TiO_2 for both methanol oxidation and dehydrogenation processes. The particle size of Pt-TiO_2 was decreased with the increasing of platinum loading. Some researchers attributed the enhanced photocatalytic activity to the increased light absorption and the retardation of the photogenerated electron-hole recombination [30, 31]. As the Fermi level of Pt is lower than that of TiO_2, photoexcited electrons can be transferred from conduction band to Pt particles deposited on the surface of TiO_2, while photogenerated valence band holes remain on the TiO_2. These activities greatly reduce the possibility of electron-hole recombination, resulting in stronger photocatalytic reactions [31].

Our previous works proved that a porous photocatalyst Pt/TiO_2-SiO_2 could efficiently decompose PYR, a four-ring PAH [34, 35]. It was also interesting to know the efficiency of Pt/TiO_2-SiO_2 for decomposing other PAHs. However, the PAH group of organic compounds is very large (over 100 toxic compounds). It would consume much time and money to identify the degradability of all PAHs in Pt/TiO_2-SiO_2 suspension. To solve this problem, quantitative structure activity relationships (QSAR) modeling, which correlates and predicts transport and transformation process data of organic pollution from their structural descriptors, may be used to study photocatalysis mechanisms and generate predicted photocatalysis process data efficiently [36, 37].

It is greatly important to develop QSAR models in which quantum chemical descriptors are used. Quantum chemical descriptors clearly describe defined molecular properties. They can easily be obtained by computation. Lu et al. [38] studied QSAR of phenols and anilines for predicting the toxicity of these compounds to algae. Hu and Aizawa [39] studied the QSAR for the estrogen receptor binding affinity of phenolic chemicals. de Lima Ribeiro and Ferreira [40] studied the QSAR of 67 PAHs in order to predict the phototoxicity of these compounds. Chen et al. [41–44] studied the QSAR in order to predict the photolysis of PAHs and dibenzo-p-dioxin. In the above studies, the quantum chemical descriptors of energy of the highest occupied molecular orbital (E_{homo}), the energy of the lowest unoccupied molecular orbital (E_{lumo}), and the GAP, the difference between E_{lumo} and E_{homo} (GAP = $E_{lumo} - E_{homo}$), were proven to be significant for PAH photochemical QSAR studies [43, 45, 46]. E_{lumo} and E_{homo} can serve as measures of the molecular capacity to donate or to accept an electron pair, respectively. The GAP expresses the necessary energy to excite an electron from HOMO to LUMO [40]. These descriptors can be obtained by semiempirical molecular orbital algorithms [40, 47].

The present study aimed to further understand the function of Pt/TiO_2-SiO_2 and to investigate the photocatalytic degradation character and kinetics of PAHs. Six PAHs were tested in Pt/TiO_2-SiO_2 suspension. The PAHs included three

TABLE 1: Physicochemical properties of NP, FL, PHE, PYR, BaP, and DahA [32, 33].

PAHs	Chemical structures	Mr	Molecular formula	CAS number	Solubility $(mmol\ L^{-1})$	$\log K_{ow}$	Vapor pressure $25°C$ (Pa)	K_H $(amt\ m^3\ mol^{-1})$
NP		128	$C_{10}H_8$	91-20-3	2.4×10^{-1}	3.37	10.9	4.5×10^{-3}
FL		166	$C_{13}H_{10}$	86-73-7	1.2×10^{-2}	4.18	8.81×10^{-2}	7.4×10^{-5}
PHE		178	$C_{14}H_{10}$	85-01-8	7.2×10^{-3}	4.45	1.6×10^{-2}	2.7×10^{-4}
PYR		202	$C_{16}H_{10}$	129-00-0	7.2×10^{-4}	4.88	8.86×10^{-4}	1.3×10^{-5}
BaP		252	$C_{20}H_{12}$	50-32-8	8.4×10^{-7}	6.06	1.5×10^{-5}	7.4×10^{-5}
DahA		278	$C_{22}H_{12}$	53-70-3	$(3.7 \pm 1.8) \times 10^{-10}$	6.50	0.8×10^{-6}	2.0×10^{-9}

(a)

(b)
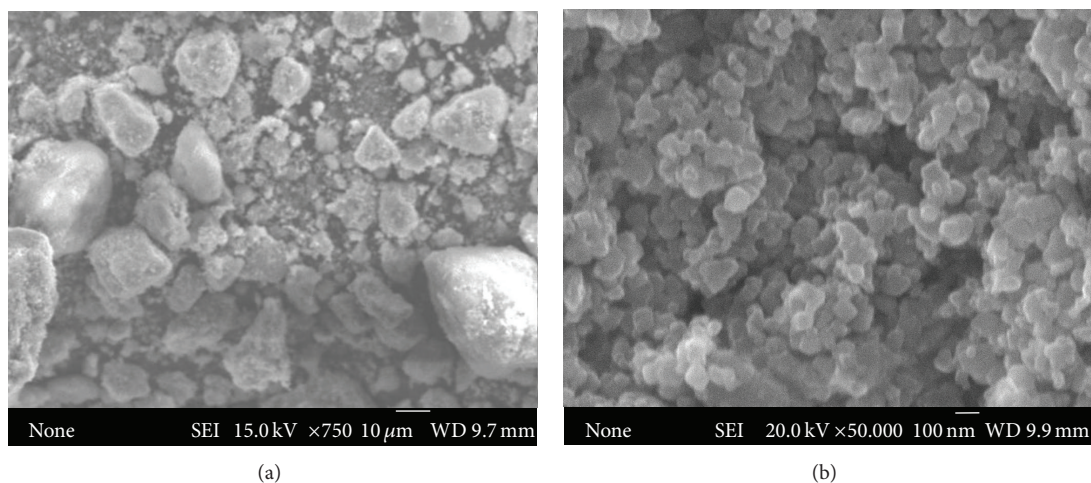
FIGURE 1: SEM images of Pt/TiO$_2$-SiO$_2$: magnification power is (a) 750 and (b) 50,000.

LMW PAHs, NP, FL, and PHE, and three HMW PAHs, PYR, benzo[a]pyrene (BaP), and dibenzo[a,h]anthracene (DahA). The selected PAHs are frequently detected in natural bodies of water [1, 2, 48]. The HMW PAHs are all acutely carcinogenic PAHs. The physicochemical properties of the selected PAHs are listed in Table 1. The degradation kinetics for photocatalytically degradable PAHs were also studied. E_{lumo}, E_{homo}, and GAP were adopted as the molecular descriptors for NP, FL, PHE, PYR, BaP, and DahA. They have been calculated in a previous research [40]. Based upon the results, the primary correlation between the photocatalytic degradability of PAHs over Pt/TiO$_2$-SiO$_2$ in water and their quantitative molecular structure was studied. Based upon the analysis of correlation, the photocatalytic degradability of 67 PAHs was predicted, and the predictions were partly verified by experiments of photocatalytic degradation of anthracene (AN) and Indeno[1.2.3.cd]pyrene (InP).

2. Experimental Section

2.1. Materials and Reagents. All reagents were of analytical quality, and all solvents were of HPLC grade. All PAHs were purchased from Kanto Chemical Co., Inc., (Japan). The Pt/TiO$_2$-SiO$_2$ used in the present study was synthesized by the method presented in previous work [35] under a compaction pressure of 1.83×10^5 kPa, Pt coating ratio of 0.4 wt%, TiO$_2$: SiO$_2$ of 1 : 1, and calcination temperature of 973 K. The scanning electron microscopy (SEM) images (Figure 1) show the surface roughness and morphology of Pt/TiO$_2$-SiO$_2$. The X-ray diffraction (XRD) and the energy-dispersive analysis of the X-ray (EDAX) analysis could give some interesting information of the structure of Pt/TiO$_2$-SiO$_2$. The XRD spectrum (Figure 2) indicates that TiO$_2$ in Pt/TiO$_2$-SiO$_2$ is in anatase form, and EDAX spectrum (Figure 3) shows the compositions of Pt/TiO$_2$-SiO$_2$.
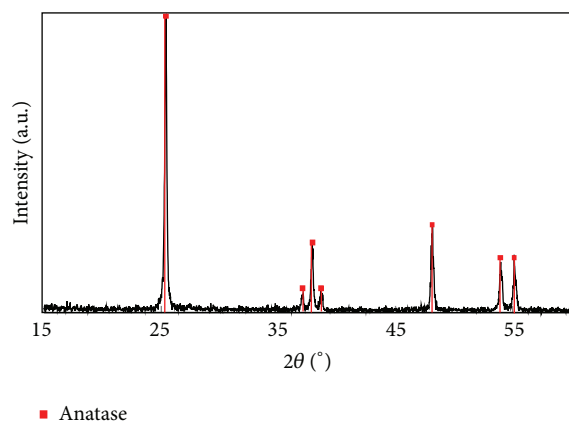
FIGURE 2: XRD spectrum of Pt/TiO$_2$-SiO$_2$.
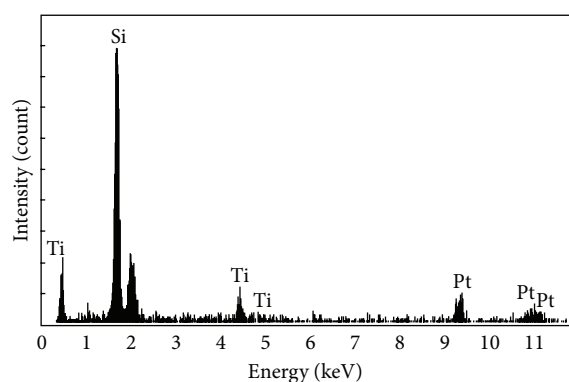
FIGURE 3: EDAX spectrum of Pt/TiO$_2$-SiO$_2$.

2.2. Photocatalytic Degradation of PAHs. The reaction solutions were prepared by introducing a proper volume of stock solution (50 mg L^{-1}) into a water/methanol (99/1) solvent to achieve a required final concentration. Water was purified by Milli-Q Plus system (Millipore). Methanol (1%) was added to minimize the adsorption of PAHs to the glassware walls. The reaction mixture was 100 mL of initial concentration of PAHs at 5×10^{-8} M and 0.3 g L^{-1} of Pt/TiO$_2$-SiO$_2$ in a glass beaker, continuously mixed with a magnetic stirrer. A black-light lamp (27 w) emitting monochromatic radiation at 368 nm was placed above the reaction solution. The distance between the lamp and the surface of the solution was 5 cm. Before irradiation, the solution was stirred in the dark for 30 min to allow the system to reach adsorption equilibrium.

A sample approximately 2 mL was taken at the designed time interval during irradiation. The same volume of ethanol was added to the sample to prevent the loss of PAHs on wall of glassware, and then it was centrifuged and filtered through a 0.45 μm cellulose filter to remove all solid particles. The treated sample was analyzed by high-performance liquid chromatography (HPLC; Hitachi L-7300 HPLC) with a fluorescence detector Hitachi L-7485. The chromatography equipment was equipped with a C-18-reversed phase separation column and the mobile phase was a 90/10 volumetric ratio mixture of methanol/water. The detecting wavelengths for NA, FL, PHE, PYR, BaP, DahA, AN, and InP were 216/308,

210/310, 248/365, 245/390, 297/430, 286/430, 297/390, and 300/500 nm (excitation/emission nm), respectively.

2.3. Photocatalytic Degradation Kinetics of PAHs. Pseudo-first-order kinetics (1) is normally assumed for PAH photolysis [12, 49]:

$$-\frac{d(C)}{dt} = kC. \tag{1}$$

Therefore, the rate constant and half-life time of PAHs degradation were calculated using the following equations:

$$
\begin{aligned}
\ln \frac{C_0}{C} &= kt, \\
t_{1/2} &= \frac{\ln 2}{K},
\end{aligned}
\tag{2}
$$

where C_0 and C are PAHs' concentration at times zero and t, respectively, k is the rate constant, and $t_{1/2}$ is the half-life time.

2.4. Data Set of Quantitative Molecular Structure of PAHs. The present work studied 67 nonsubstituted PAHs containing 2–7 rings with 5 and 6 carbon atoms (Figure 4). The electronic descriptors of E_{lumo}, E_{homo}, and the GAP for PAHs obtained using the AM1 algorithm reported by de Lima Ribeiro and Ferreira [40] were selected in this study.

3. Results and Discussion

3.1. Photocatalytic Degradation of PAHs in Pt/TiO$_2$-SiO$_2$ Suspension. The photolysis and photocatalysis of the selected PAHs are shown in Figure 5. It was observed that Pt/TiO$_2$-SiO$_2$ played a very different role in photocatalysis of LMW PAHs and HMW PAHs. The presence of Pt/TiO$_2$-SiO$_2$ increased the degradation rates of HMW PAHs efficiently, while the presence of Pt/TiO$_2$-SiO$_2$ inhibited the degradation rates of LMW PAHs. Similar results were obtained in previous research, which confirms that the presence of TiO$_2$ resulted in a slower photooxidation rate of FL [50]. This difference is considered to be related to the PAHs' molecular structure, which determines the reactivity of a PAH.

3.2. Kinetics of Photocatalytic Degradation of PAHs. The pseudo-first-order kinetics equation, rate constant, half-life time, correlation coefficients, and total removal efficiency of photolysis and photocatalysis of selected PAHs are summarized in Table 2. The results show that the total removal efficiencies of photocatalysis for NP, FL, and PHE are 4.8%, 24.7%, and 34.5%, respectively, lower than the photolysis removal efficiencies of 46.6%, 41.5%, and 41.9%, respectively. On the other hand, the total removal efficiencies of photocatalysis for PYR, BaP, and DahA were 81.4%, 99.7%, and 88.6%, respectively, all higher than the photolysis removal efficiency of 37.8%, 99.0%, and 71.8%, respectively. The rate constant of the tested PAHs presents the same phenomenon. The rate constant of photocatalysis of NP, FL, and PHE is 0.0006, 0.0021, and 0.0038, respectively, lower than the photolysis removal efficiency of 0.0054, 0.0035, and 0.0046.
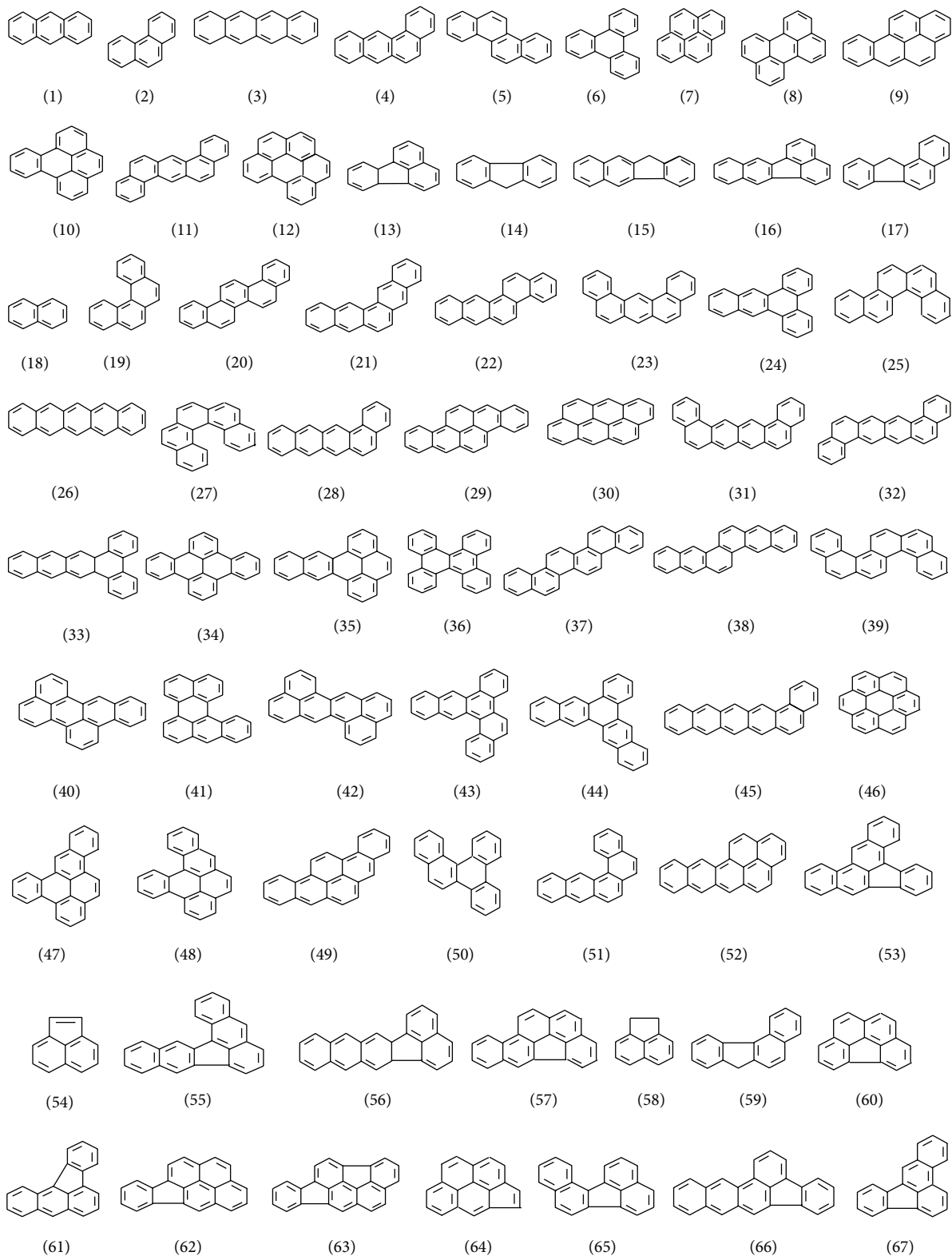
FIGURE 4: Chemical structures of PAHs [40].
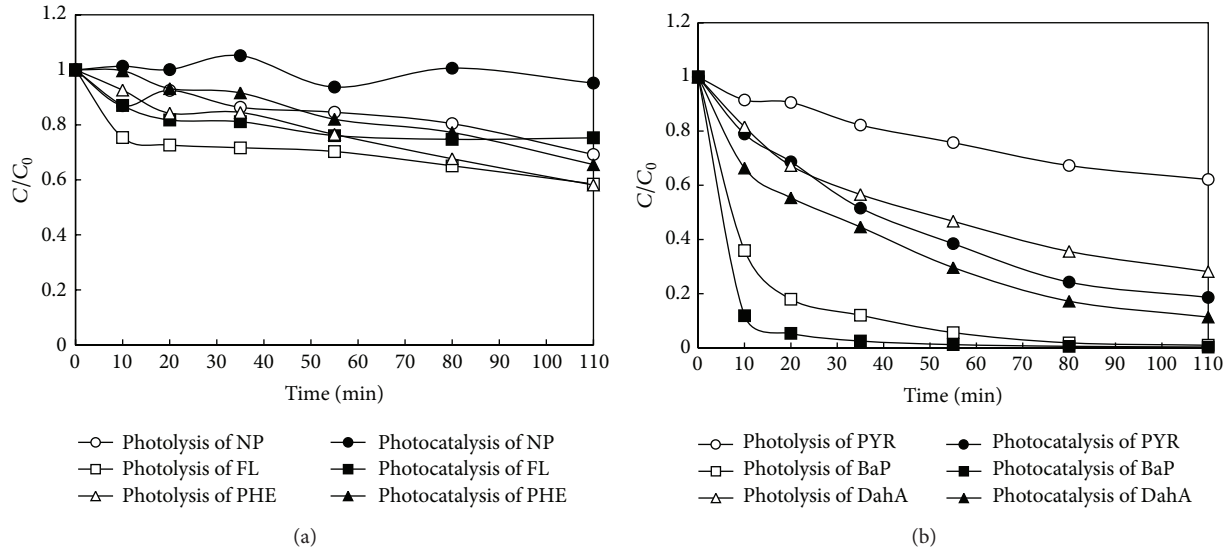
FIGURE 5: The photolysis and photocatalysis of (a) LMW PAHs: NP, FL, and PHE and (b) HMW PAHs: PYR, BaP, and DahA.

TABLE 2: Pseudo-first-order regression equation, correlation coefficient, rate constant, half-life time, and the total removal efficiency of photolysis and photocatalysis of PYR, BaP, and DahA (initial concentration: 5×10^{-8} M).

Treatment	PAHs	Regression equation	$t_{1/2}$ (min)	K (min^{-1})	R^2	Removal efficiency (%)
Photolysis	NP	$y = 0.0054x + 0.0259$	128.4	0.0054	0.9905	46.6
	FL	$y = 0.0035x + 0.1646$	198.0	0.0035	0.7332	41.5
	PHE	$y = 0.0046x + 0.0258$	150.7	0.0046	0.9802	41.9
	PYR	$y = 0.0043x + 0.0278$	161.2	0.0043	0.9833	37.8
	BaP	$y = 0.0398x + 0.5683$	17.4	0.0398	0.958	99.0
	DahA	$y = 0.0112x + 0.1094$	61.9	0.0112	0.9767	71.8
Photocatalysis	NP	$y = 0.0006x - 0.0111$	1155.2	0.0006	0.9093	4.8
	FL	$y = 0.0021x + 0.1047$	330.1	0.0021	0.6774	24.7
	PHE	$y = 0.0038x - 0.0211$	182.4	0.0038	0.9803	34.5
	PYR	$y = 0.0155x + 0.0731$	44.7	0.0155	0.9878	81.4
	BaP	$y = 0.0452x + 1.433$	15.3	0.0452	0.8443	99.7
	DahA	$y = 0.0192x + 0.1435$	36.1	0.0192	0.9878	88.6

On the contrary, the rate constant of photocatalysis for PYR, BaP, and DahA of 0.0155, 0.0452, and 0.0192, respectively, is all higher than the rate constant of 0.0043, 0.0398, and 0.0112, respectively.

The correlation coefficients indicate that both the photolysis and photocatalysis of PAHs fit the pseudo-first-order equation very well, except FL, for which the R^2 for photolysis and photocatalysis are 0.7332 and 0.6774, respectively. This might be attributed to the special molecular structure of FL, which is the only PAH with a 5-carbon ring structure and which has the largest GAP value of 8.5021 eV among the tested PAHs (see Section 3.3), resulting in a more difficult photoinduced reaction for FL. The results indicate that the photolytic and photocatalytic degradation mechanisms of FL are different from that of other tested PAHs.

3.3. E_{lumo}, E_{homo}, and GAP of PAHs.

The E_{lumo}, E_{homo}, and GAP of NP, FL, PHE, PYR, BaP, and DahA obtained by AM1

algorithm in de Lima Ribeiro and Ferreira research [40] are summarized in Table 3.

It is observed that the values of E_{homo} of HMW PAHs are all higher than those of LMW PAHs. On the contrary, the GAP values of HMW PAHs molecular are all lower than those of LMW PAHs. The GAP values of the PAHs for which degradation could be accelerated by Pt/TiO$_2$-SiO$_2$ are all smaller than or equal to 7.4529 eV; on the other hand, the GAP values of PAHs for which degradation was inhibited by Pt/TiO$_2$-SiO$_2$ are all larger than or equal to 8.2086 eV. These results indicate that more photoenergy is required for triggering the degradation of LMW PAHs than that of HMW PAHs. It can be understood that GAP values can serve as a measure of the excitability of the molecule: the smaller the GAP of a PAH, the easier it will be excited.

3.4. Prediction of the Photocatalytic Degradability of 67 PAHs.

The photochemical properties of PAHs undoubtedly depend

TABLE 3: Summary of E_{lumo}, E_{homo}, and GAP for NP, FL, PHE, PYR, BaP, and DahA.

	NP	FL	PHE	PYR	BaP	DahA
HOMO (eV)	−8.7099	−8.7109	−8.6171	−8.0692	−7.9173	−8.2570
LUMO (eV)	−0.2650	−0.2088	−0.4085	−0.9225	−1.1142	−0.8041
GAP (eV)	8.4449	8.5021	8.2086	7.1467	6.8031	7.4529
Degradation accelerated by Pt/TiO$_2$-SiO$_2$	No	No	No	Yes	Yes	Yes

upon their molecule excitability; therefore, the GAP value is expected to predict the photocatalytic degradability of other PAHs in Pt/TiO$_2$-SiO$_2$ suspension.

As mentioned above, the maximum GAP of DahA of tested PAHs for which degradation could be accelerated by Pt/TiO$_2$-SiO$_2$ was 7.4529 eV, and the minimum GAP of PHE of tested PAHs for which degradation was accelerated by Pt/TiO$_2$-SiO$_2$ was 8.2086 eV. Therefore, one can deduce that when the GAP of a PAH is less than or equal to 7.4529 eV, this PAH can be degraded in Pt/TiO$_2$-SiO$_2$-UV system. On the other hand, when the GAP of a PAH is larger than or equal to 8.2086 eV, this PAH cannot be degraded in Pt/TiO$_2$-SiO$_2$-UV system. When the GAP of a PAH is between 7.4529 eV and 8.2086 eV, the degradation potential of this PAH is uncertain in the experimental condition of our study.

Following the above approach, the photocatalytic degradability of 67 PAHs was predicted and is listed in Table 4. The results show that 46 PAHs are potentially photocatalytically degradable. All of these 46 PAHs, except AN (anthracene, labelled no. 1), were all HMW PAHs. There were four PAHs for which no photocatalytic degradability was predicted. All four of these PAHs were LMW PAHs (labelled nos. 2, 14, 18, and 58). For these LMW PAHs, biological treatment can be a very good complement [51, 52]. The photocatalytic degradability of another seventeen PAHs was determined to be uncertain, most of which were 4~6-ring PAHs.

3.5. Verification of Prediction. To verify the above prediction, the photolysis and photocatalysis of AN (number 1, 3-ring PAH) and InP (number 62, 6-ring PAH), whose GAPs are 7.2795 eV and 6.8528 eV, respectively, were examined in Pt/TiO$_2$-SiO$_2$-UV system. We selected AN and InP because they are also PAHs commonly found in water [18, 53], and AN is the only LMW PAH which is assumed to be photocatalytically degradable. If the prediction was right, the degradation of these two PAHs should be accelerated in the Pt/TiO$_2$-SiO$_2$-UV system. It is shown clearly in Figure 6 that the degradation rate of AN and InP is indeed improved with the presence of Pt/TiO$_2$-SiO$_2$. The photocatalytic degradation of AN and InP in the Pt/TiO$_2$-SiO$_2$-UV system can also be described by the first-order kinetic model. The rate constant, half-life time, and the total removal efficiency of photocatalysis for AN are 0.0766 min^{-1}, 9.05 min, and 100%, respectively, while those for InP were 0.0079 min^{-1}, 87.74 min, and 63.11%, respectively. Therefore, the prediction is verified in a way.

For further study, the determination of photocatalytic degradability for the remaining PAHs can be identified by setting a new boundary value of GAP, which can be obtained by appropriate testing of the uncertain PAHs.

(a)

(b)
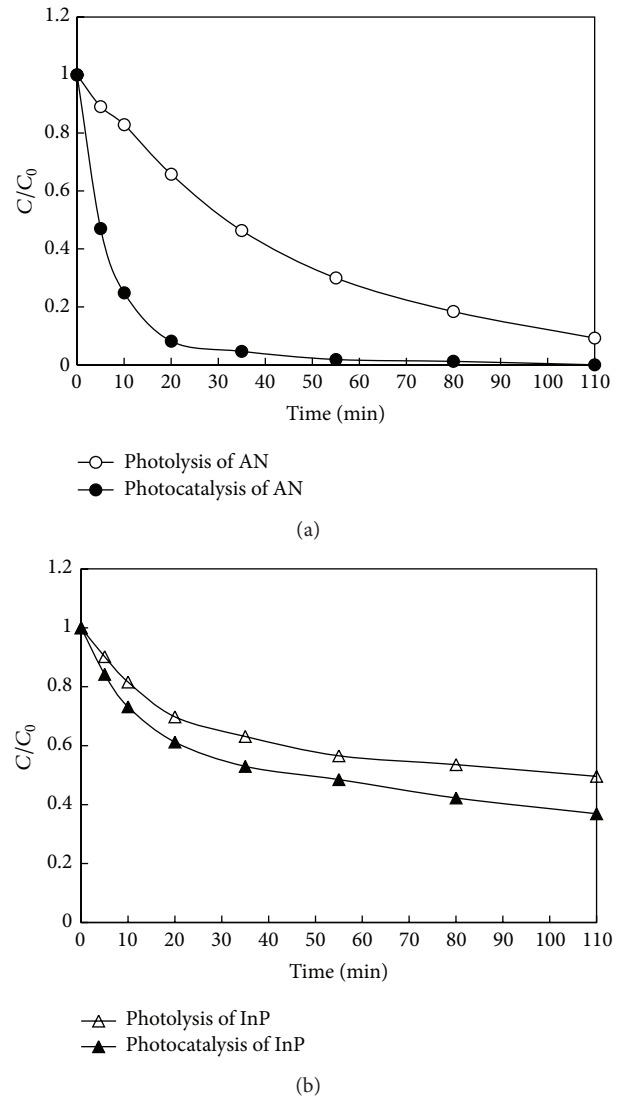
FIGURE 6: The photolysis and photocatalysis of (a) AN and (b) InP. Initial concentration is 5×10^{-8} M.

The prediction is significant for realistic water treatment. By knowing the value of GAP, the photocatalytic degradability of some pollutants in the photocatalyst suspension might be known without doing any experimentation. The GAP value can be obtained easily from previous research or by computation. Therefore, large expenditures of time and money required for the determination can be avoided.

TABLE 4: Evaluation of photocatalytic degradability of 67 PAHs.

	PAHs name	E_{lumo} (eV)	E_{homo} (eV)	GAP (eV)		Photocatalytic degradability	
1	*Anthracene*	−0.8417	−8.1212	7.2795	○		
2	**Phenanthrene**	**−0.4085**	**−8.6171**	**8.2086**			×
3	Naphthacene	−1.2321	−7.7488	6.5167	○		
4	Benz[a]anthracene	−0.8116	−8.2079	7.3963	○		
5	Chrysene	−0.6762	−8.3697	7.6935		△	
6	Triphenylene	−0.4532	−8.6584	8.2052		△	
7	**Pyrene**	**−0.9225**	**−8.0692**	**7.1467**	○		
8	Perylene	−1.1508	−7.8598	6.7090	○		
9	**Benzo[a]pyrene**	**−1.1142**	**−7.9173**	**6.8031**	○		
10	Benzo[e]pyrene	−0.8580	−8.2149	7.3569	○		
11	**Dibenz[a.h]anthracene**	**−0.8041**	**−8.257**	**7.4529**	○		
12	Benzo[ghi]perylene	−1.0662	−8.0235	6.9573	○		
13	Fluoranthene	−0.9294	−8.6301	7.7007		△	
14	**Fluorene**	**−0.2088**	**−8.7109**	**8.5021**			×
15	Benzo[b]fluorene	−0.4880	−8.4783	7.9903		△	
16	Benzo[k]fluoranthene	−1.1769	−8.3164	7.1395	○		
17	Benzo[a]fluorene	−0.5607	−8.3656	7.8049		△	
18	**Naphthalene**	**−0.2650**	**−8.7099**	**8.4449**			×
19	Benzo[c]phenanthrene	−0.6456	−8.4438	7.7982		△	
20	Picene	−0.7209	−8.3487	7.6278		△	
21	Pentaphene	−0.8400	−8.2022	7.3622	○		
22	Benzo[b]chrysene	−0.9948	−8.0511	7.0563	○		
23	Dibenz[a. j]anthracene	−0.8736	−8.1916	7.3180	○		
24	Benzo[b]triphenylene	−0.8319	−8.2255	7.3936	○		
25	Benzo[c]chrysene	−0.6931	−8.3898	7.6967		△	
26	Pentacene	−1.5500	−7.4414	5.8914	○		
27	Dibenzo[c. g]phenanthrene	−0.6732	−8.3498	7.6766		△	
28	Benzo[a]naphthacene	−1.1857	−7.8407	6.6550	○		
29	Dibenzo[b. def]chrysene	−1.3630	−7.6784	6.3154	○		
30	Dibenzo[def. mno]chrysene	−1.4067	−7.6315	6.2248	○		
31	Dibenzo[a.j]naphthacene	−1.1349	−7.9321	6.7972	○		
32	Dibenzo[a.l]naphthacene	−1.1352	−7.9345	6.7993	○		
33	Dibenzo[a.c]naphthacene	−1.1564	−7.9148	6.7584	○		
34	Dibenzo[el]naphthacene	−0.8276	−8.2948	7.4672		△	
35	Dibenzo[de.gr]naphthacene	−0.8336	−8.2774	7.4438	○		
36	Dibenzo[g.p]chrysene	−0.8832	−8.1128	7.2296	○		
37	Benzo[c]picene	−0.8279	−8.2597	7.4318	○		
38	Dibenzo[b.k]chrysene	−1.1775	−7.8832	6.7057	○		
39	Dibenzo[cl]chrysene	−0.7827	−8.2649	7.4822		△	
40	Benzo[b]perylene	−1.1806	−7.8666	6.686	○		
41	Benzo[a]perylene	−1.4836	−7.5284	6.0448	○		
42	Dibenzo[de.mn]naphthacene	−1.5482	−7.4305	5.8823	○		
43	Naphtho[2.3-g]chrysene	−0.9944	−8.1177	7.1233	○		
44	Benzo[h]pentaphene	−0.8089	−8.3009	7.4920		△	
45	Benzo[a]pentacene	−1.4685	−7.5763	6.1078	○		
46	Coronene	−1.0021	−8.1438	7.1417	○		
47	Naphtho[1.2.3.4-def]chrysene	−1.0583	−8.0233	6.9650	○		
48	Dibenzo[def.p]chrysene	−1.1022	−7.9553	6.8531	○		
49	Benzo[rst]pentaphene	−1.1838	−7.865	6.6812	○		
50	Benzo[g]chrysene	−0.7660	−8.2705	7.5045		△	

TABLE 4: Continued.

	PAHs name	E_{lumo} (eV)	E_{homo} (eV)	GAP (eV)	Photocatalytic degradability		
51	2.3:5.6-Dibenzophenanthrene	−0.9636	−8.0436	7.0800	○		
52	Naphtho[2.1.8-qra]-naphthacene	−1.3169	−7.7299	6.4130	○		
53	Dibenz[a.e]aceanthrylene	−1.2806	−8.1423	6.8617	○		
54	Acenaphthylene	−0.9359	−8.9429	8.0070		△	
55	Dibenzo[a.k]fluoranthene	−1.2992	−7.9435	6.6443	○		
56	Naphtho[2.3-k]fluoranthene	−0.9127	−7.9781	7.0654	○		
57	Dibenzo[k.mno]fluoranthene	−0.9755	−8.4001	7.4246	○		
58	1.2-Dihydroacenaphthylene	−0.2132	−8.4945	8.2813			×
59	Benzo[c]fluorene	−0.6415	−8.2836	7.6421		△	
60	Benzo[ghi]fluoranthene	−0.9911	−8.6996	7.7085		△	
61	Benzo[a]aceanthrylene	−1.3219	−8.085	6.7631	○		
62	*Indeno[1.2.3.cd]pyrene*	−1.2835	−8.1363	6.8528	○		
63	Indeno[1.2.3.*cd*]fluoranthene	−1.3350	−8.5435	7.2085	○		
64	Cyclopenta[cd]pyrene	−1.3123	−8.2727	6.9604	○		
65	Benzo[j]fluoranthene	−1.1767	−8.3165	7.1398	○		
66	Dibenz[e.k]acephenanthrylene	−1.0702	−8.2215	7.1513	○		
67	Benzo[b]fluoranthene	−0.9654	−8.6166	7.6512		△	
Total		—	—	—	46	17	4

(○) means having photocatalytic degradability (GAP ≤ 7.4529 eV); (△) means having indeterminate photocatalytic degradability (7.4529 ev ≤ GAP ≤ 8.2086 eV); (×) means having nonphotocatalytic degradability.

4. Conclusions

The present study was undertaken to probe the correlation between the photocatalytic degradability of PAHs over Pt/TiO$_2$-SiO$_2$ in water and their quantitative molecular structure. Six PAHs, NP, FL, PHE, PYR, BaP, and DahA, were experimentally tested in a Pt/TiO$_2$-SiO$_2$ suspension under UV irradiation. The results show that the degradation of HMW PAHs, PYR, BaP, and DahA, was accelerated significantly in the presence of Pt/TiO$_2$-SiO$_2$, while the degradation efficiency of low molecular weight PAHs, NP, FL and PHE, was inhibited under the same experimental conditions. Both the photolysis and photocatalysis of PAHs fit the pseudo-first-order equation very well, except FL. This might be attributed to FL's 5-carbon ring structure. Quantitative analysis of molecular descriptors of E_{lumo}, E_{homo}, and GAP suggested that GAP was significant for predicting PAHs' photocatalytic degradability. By comparing to the maximum GAP (7.4529 eV) of PAHs (DahA) that could be photocatalytically degraded and the minimum GAP (8.2086 eV) of PAHs (PHE) that could not be photocatalytically degraded in this study, the photocatalytic degradability of 67 PAHs was predicted: 46 PAHs were potentially photocatalytically degradable, 4 PAHs were predicted to be not photocatalytically degradable, and 17 PAHs were predicted to exhibit indeterminate photocatalytic degradation. The experiments of photocatalytic degradation of AN and InP verified the above prediction. This prediction indicates that Pt/TiO$_2$-SiO$_2$ can offer a very promising method for biorefractory HMW PAHs removal. It can also be a very good complement for biological treatment of PAH contaminated water.

Conflict of Interests

The authors of the paper do not have a direct financial relation with the commercial identity mentioned in this paper that might lead to a conflict of interests.

Acknowledgments

References

[1] G. Guo, F. Wu, H. He, R. Zhang, H. Li, and C. Feng, "Distribution characteristics and ecological risk assessment of PAHs in surface waters of China," *Science China Earth Sciences*, vol. 55, no. 6, pp. 914–925, 2012.

[2] N. U. Benson, J. P. Essien, F. E. Asuquo, and A. L. Eritobor, "Occurrence and distribution of polycyclic aromatic hydrocarbons in surface microlayer and subsurface seawater of Lagos Lagoon, Nigeria," *Environmental Monitoring and Assessment*, vol. 186, no. 9, pp. 5519–5529, 2014.

[3] L. N. Ukiwe, U. U. Egereonu, P. C. Njoku, C. I. A. Nwoko, and J. I. Allinor, "Polycyclic aromatic hydrocarbons degradation techniques: a review," *International Journal of Chemistry*, vol. 5, no. 4, pp. 43–55, 2013.

[4] K. M. Koran, M. T. Suidan, A. P. Khodadoust, G. A. Sorial, and R. C. Brenner, "Effectiveness of an anaerobic granular activated carbon fluidized-bed bioreactor to treat soil wash fluids: a proposed strategy for remediating PCP/PAH contaminated soils," *Water Research*, vol. 35, no. 10, pp. 2363–2370, 2001.

[5] A. Rubio-Clemente, R. A. Torres-Palma, and G. A. Peñuela, "Removal of polycyclic aromatic hydrocarbons in aqueous environment by chemical treatments: a review," *Science of the Total Environment*, vol. 478, pp. 201–225, 2014.

[6] A. di Paola, E. García-López, G. Marcì, and L. Palmisano, "A survey of photocatalytic materials for environmental remediation," *Journal of Hazardous Materials*, vol. 211-212, pp. 3–29, 2012.

[7] I. Fechete, Y. Wang, and J. C. Védrine, "The past, present and future of heterogeneous catalysis," *Catalysis Today*, vol. 189, no. 1, pp. 2–27, 2012.

[8] M. R. Haque and M. Muneer, "Photodegradation of norfloxacin in aqueous suspensions of titanium dioxide," *Journal of Hazardous Materials*, vol. 145, no. 1-2, pp. 51–57, 2007.

[9] T. Jagadale, M. Kulkarni, D. Pravarthana, W. Ramadan, and P. Thakur, "Photocatalytic degradation of azo dyes using Au:TiO$_2$, γ-Fe$_3$O$_3$:TiO$_2$ functional nanosystems," *Journal of Nanoscience and Nanotechnology*, vol. 12, no. 2, pp. 928–936, 2012.

[10] N. Muhd Julkapli, S. Bagheri, and S. Abd Hamid, "Recent advances in heterogeneous photocatalytic decolorization of synthetic dyes," *The Scientific World Journal*, vol. 2014, Article ID 692307, 25 pages, 2014.

[11] S. Kurinobu, K. Tsurusaki, Y. Natui, M. Kimata, and M. Hasegawa, "Decomposition of pollutants in wastewater using magnetic photocatalyst particles," *Journal of Magnetism and Magnetic Materials*, vol. 310, no. 2, part 3, pp. e1025–e1027, 2007.

[12] A. Dhir, N. T. Prakash, and D. Sud, "Comparative studies on TiO$_2$/ZnO photocatalyzed degradation of 4-chlorocatechol and bleach mill effluents," *Desalination and Water Treatment*, vol. 46, no. 1–3, pp. 196–204, 2012.

[13] S. Wen, J. Zhao, G. Sheng, J. Fu, and P. Peng, "Photocatalytic reactions of pyrene at TiO$_2$/water interfaces," *Chemosphere*, vol. 50, no. 1, pp. 111–119, 2003.

[14] H. F. Lin and K. T. Valsaraj, "A titania thin film annular photocatalytic reactor for the degradation of polycyclic aromatic hydrocarbons in dilute water streams," *Journal of Hazardous Materials*, vol. 99, no. 2, pp. 203–219, 2003.

[15] S. Dass, M. Muneer, and K. R. Gopidas, "Photocatalytic degradation of wastewater pollutants. Titanium-dioxide-mediated oxidation of polynuclear aromatic hydrocarbons," *Journal of Photochemistry and Photobiology A: Chemistry*, vol. 77, no. 1, pp. 83–88, 1994.

[16] A. Lair, C. Ferronato, J.-M. Chovelon, and J.-M. Herrmann, "Naphthalene degradation in water by heterogeneous photocatalysis: an investigation of the influence of inorganic anions," *Journal of Photochemistry and Photobiology A: Chemistry*, vol. 193, no. 2-3, pp. 193–203, 2008.

[17] O. T. Woo, W. K. Chung, K. H. Wong, A. T. Chow, and P. K. Wong, "Photocatalytic oxidation of polycyclic aromatic hydrocarbons: intermediates identification and toxicity testing," *Journal of Hazardous Materials*, vol. 168, no. 2-3, pp. 1192–1199, 2009.

[18] N. Vela, M. Martínez-Menchón, G. Navarro, G. Pérez-Lucas, and S. Navarro, "Removal of polycyclic aromatic hydrocarbons (PAHs) from groundwater by heterogeneous photocatalysis under natural sunlight," *Journal of Photochemistry and Photobiology A: Chemistry*, vol. 232, pp. 32–40, 2012.

[19] H. Tong, S. Ouyang, Y. Bi, N. Umezawa, M. Oshikiri, and J. Ye, "Nano-photocatalytic materials: possibilities and challenges," *Advanced Materials*, vol. 24, no. 2, pp. 229–251, 2012.

[20] D. Bahnemann, "Photocatalytic water treatment: solar energy applications," *Solar Energy*, vol. 77, no. 5, pp. 445–459, 2004.

[21] A. Matsuda, S. Sreekantan, and W. Krengvirat, "Well-aligned TiO$_2$ nanotube arrays for energy-related applications under solar irradiation," *Journal of Asian Ceramic Societies*, vol. 1, no. 3, pp. 203–219, 2013.

[22] Y.-K. Lai, J.-Y. Huang, H.-F. Zhang et al., "Nitrogen-doped TiO$_2$ nanotube array films with enhanced photocatalytic activity under various light sources," *Journal of Hazardous Materials*, vol. 184, no. 1–3, pp. 855–863, 2010.

[23] Y. Lai, L. Sun, Y. Chen, H. Zhuang, C. Lin, and J. W. Chin, "Effects of the structure of TiO$_2$ nanotube array on Ti substrate on its photocatalytic activity," *Journal of the Electrochemical Society*, vol. 153, no. 7, pp. D123–D127, 2006.

[24] D. Yu, B. Bo, and Y. He, "Fabrication of TiO$_2$ yeast-carbon hybrid composites with the raspberry-like structure and their synergistic adsorption-photocatalysis performance," *Journal of Nanomaterials*, vol. 2013, Article ID 851417, 8 pages, 2013.

[25] C. Hu, Y. Wang, and H. Tang, "Preparation and characterization of surface bond-conjugated TiO$_2$/SiO$_2$ and photocatalysis for azo dyes," *Applied Catalysis B: Environmental*, vol. 30, pp. 277–285, 2001.

[26] K. Balachandaran, R. Venckatesh, and R. Sivaraj, "Synthesis of nano TiO$_2$-SiO$_2$ composite using sol-gel method: effect on size, surface morphology and thermal stability," *International Journal of Engineering Science and Technology*, vol. 2, no. 8, pp. 3695–3700, 2010.

[27] Y. Guo, S. Yang, X. Zhou, C. Lin, Y. Wang, and W. Zhang, "Enhanced photocatalytic activity for degradation of methyl orange over silica-titania," *Journal of Nanomaterials*, vol. 2011, Article ID 296953, 9 pages, 2011.

[28] Y. Ishibai, J. Sato, S. Akita, T. Nishikawa, and S. Miyagishi, "Photocatalytic oxidation of NOx by Pt-modified TiO$_2$ under visible light irradiation," *Journal of Photochemistry and Photobiology A: Chemistry*, vol. 188, no. 1, pp. 106–111, 2007.

[29] S. P. Devipriya, S. Yesodharan, and E. P. Yesodharan, "Solar photocatalytic removal of chemical and bacterial pollutants from water using Pt/TiO$_2$-coated ceramic tiles," *International Journal of Photoenergy*, vol. 2012, Article ID 970474, 8 pages, 2012.

[30] L. M. Ahmed, I. Ivanova, F. H. Hussein, and D. W. Bahnemann, "Role of platinum deposited on TiO$_2$ in photocatalytic methanol oxidation and dehydrogenation reactions," *International Journal of Photoenergy*, vol. 2014, Article ID 503516, 9 pages, 2014.

[31] M. Ni, M. K. H. Leung, D. Y. C. Leung, and K. Sumathy, "A review and recent developments in photocatalytic water-splitting using TiO$_2$ for hydrogen production," *Renewable and Sustainable Energy Reviews*, vol. 11, no. 3, pp. 401–425, 2007.

[32] NCB, "The National Center for Biotechnology-PubChem Compound," http://pubchem.ncbi.nlm.nih.gov/summary/summary.cgi?cid=995#itabs-3d.

[33] E. Martinez, M. Gros, S. Lacorte, and D. Barceló, "Simplified procedures for the analysis of polycyclic aromatic hydrocarbons in water, sediments and mussels," *Journal of Chromatography A*, vol. 1047, no. 2, pp. 181–188, 2004.

[34] Z. Luo, K. Katayama-Hirayama, T. Akitsu, and H. Kaneko, "Photocatalytic degradation of pyrene in porous Pt/TiO$_2$-SiO$_2$ photocatalyst suspension under UV irradiation," *Nano*, vol. 3, no. 5, pp. 317–322, 2008.

[35] Z. Luo, K. Katayama-Hirayama, K. Hirayama, T. Akitsu, and H. Kaneko, "Preparation of porous Pt/TiO$_2$-SiO$_2$ photocatalyst and its performance in photocatalytic degradation of pyrene," *International Journal of Plasma Environmental Science & Technology*, vol. 2, no. 2, pp. 77–81, 2008.

[36] J. Chen, W. J. G. M. Peijnenburg, X. Quan et al., "Is it possible to develop a QSPR model for direct photolysis half-lives of PAHs under irradiation of sunlight?" *Environmental Pollution*, vol. 114, no. 1, pp. 137–143, 2001.

[37] C. Raillard, V. Héquet, B. Gao et al., "Correlations between molecular descriptors from various volatile organic compounds and photocatalytic oxidation kinetic constants," *International Journal of Chemical Reactor Engineering*, vol. 11, no. 2, pp. 799–813, 2013.

[38] G.-H. Lu, C. Wang, and X.-L. Guo, "Prediction of toxicity of phenols and anilines to algae by quantitative structure-activity relationship," *Biomedical and Environmental Sciences*, vol. 21, no. 3, pp. 193–196, 2008.

[39] J.-Y. Hu and T. Aizawa, "Quantitative structure-activity relationships for estrogen receptor binding affinity of phenolic chemicals," *Water Research*, vol. 37, no. 6, pp. 1213–1222, 2003.

[40] F. A. de Lima Ribeiro and M. M. C. Ferreira, "QSAR model of the phototoxicity of polycyclic aromatic hydrocarbons," *Journal of Molecular Structure: THEOCHEM*, vol. 719, no. 1–3, pp. 191–200, 2005.

[41] J. Chen, X. Quan, W. J. G. M. Peijnenburg, and F. Yang, "Quantitative structure-property relationships (QSPRs) on direct photolysis quantum yields of PCDDs," *Chemosphere*, vol. 43, no. 2, pp. 235–241, 2001.

[42] J. Chen, X. Quan, Y. Yan, F. Yang, and W. J. G. M. Peijnenburg, "Quantitative structure-property relationship studies on direct photolysis of selected polycyclic aromatic hydrocarbons in atmospheric aerosol," *Chemosphere*, vol. 42, no. 3, pp. 263–270, 2001.

[43] J. Chen, W. J. G. M. Peijnenburg, X. Quan, and F. Yang, "Quantitative structure-property relationships for direct photolysis quantum yields of selected polycyclic aromatic hydrocarbons," *Science of The Total Environment*, vol. 246, no. 1, pp. 11–20, 2000.

[44] J. Chen, D. Wang, S. Wang, X. Qiao, and L. Huang, "Quantitative structure-property relationships for direct photolysis of polybrominated diphenyl ethers," *Ecotoxicology and Environmental Safety*, vol. 66, no. 3, pp. 348–352, 2007.

[45] G. D. Veith, O. G. Mekenyan, G. T. Ankley, and D. J. Call, "A QSAR analysis of substituent effects on the photoinduced acute toxicity of PAHs," *Chemosphere*, vol. 30, no. 11, pp. 2129–2142, 1995.

[46] O. G. Mekenyan, G. T. Ankley, G. D. Veith, and D. J. Call, "QSARs for photo-induced toxicity: I—acute lethality of polycyclic aromatic hydrocarbons to Daphnia magna," *Chemosphere*, vol. 28, no. 3, pp. 567–582, 1994.

[47] B.-C. Wang, J.-C. Chang, H.-C. Tso, H.-F. Hsu, and C.-Y. Cheng, "Theoretical investigation the electroluminescence characteristics of pyrene and its derivatives," *Journal of Molecular Structure: THEOCHEM*, vol. 629, no. 1–3, pp. 11–20, 2003.

[48] H. Wang, C. Wang, W. Wu, Z. Mo, and Z. Wang, "Persistent organic pollutants in water and surface sediments of Taihu Lake, China and risk assessment," *Chemosphere*, vol. 50, no. 4, pp. 557–562, 2003.

[49] Y. Li, J. Niu, L. Yin et al., "Photocatalytic degradation kinetics and mechanism of pentachlorophenol based on Superoxide radicals," *Journal of Environmental Sciences*, vol. 23, no. 11, pp. 1911–1918, 2011.

[50] J. Sabaté, J. M. Bayona, and A. M. Solanas, "Photolysis of PAHs in aqueous phase by UV irradiation," *Chemosphere*, vol. 44, no. 2, pp. 119–124, 2001.

[51] N. Das and P. Chandran, "Microbial degradation of petroleum hydrocarbon contaminants: an overview," *Biotechnology Research International*, vol. 2011, Article ID 941810, 13 pages, 2011.

[52] J.-S. Seo, Y.-S. Keum, and Q. X. Li, "Bacterial degradation of aromatic compounds," *International Journal of Environmental Research and Public Health*, vol. 6, no. 1, pp. 278–309, 2009.

[53] Y. Mei, F. Wu, L. Wang, Y. Bai, W. Li, and H. Liao, "Binding characteristics of perylene, phenanthrene and anthracene to different DOM fractions from lake water," *Journal of Environmental Sciences*, vol. 21, no. 4, pp. 414–423, 2009.

Research Article

Facile Synthesis and Characterization of N-Doped TiO$_2$ Photocatalyst and Its Visible-Light Activity for Photo-Oxidation of Ethylene

Yu-Hao Lin,[1] **Chih-Huang Weng,**[2] **Arun Lal Srivastav,**[3]
Yao-Tung Lin,[3] **and Jing-Hua Tzeng**[3]

[1]*Centre for Environmental Restoration and Disaster Reduction, National Chung Hsing University, 250 Kuo Kuang Road, Taichung 40227, Taiwan*
[2]*Department of Civil and Ecological Engineering, I-Shou University, Kaohsiung City 84008, Taiwan*
[3]*Department of Soil and Environmental Sciences, National Chung Hsing University, 250 Kuo Kuang Road, Taichung 40227, Taiwan*

Correspondence should be addressed to Yao-Tung Lin; yaotung@nchu.edu.tw

A facile wet chemical method was adopted for preparing highly photoactive nitrogen doped TiO$_2$ (N-TiO$_2$) powders with visible responsive capability, which could be achieved by the hydrolysis of titanium isopropoxide (TTIP) in the ammonium hydroxide precursor solution in various concentrations and then calcined at different temperatures. The N-TiO$_2$ powders were characterized, and the photocatalytic activity was evaluated for the photocatalytic oxidation of ethylene gas under visible light irradiation to optimize the synthesizing conditions of N-TiO$_2$ catalyst. The N-TiO$_2$ photocatalytic powders were calcined in a range of temperatures from 300 to 600°C and obviously found to have greater photocatalytic activities than commercial TiO$_2$ P25. The strong absorption in the visible light region could be ascribed to good crystallization and adapted sinter temperature of as prepared sample. XPS test demonstrated that the N was doped into TiO$_2$ lattice and made an interstitial formation (Ti-O-N), and N doping also retarded the phase transformation from anatase to rutile as well. The N-TiO$_2$ catalyst prepared with 150 mL ammonium hydroxide added and calcined at 500°C showed the best photocatalytic activity. The experimental results also proved the enhanced photoactivity of N-TiO$_2$ material depends on the synthesizing conditions.

1. Introduction

Recently, the nanomaterial, such as nanoiron, titanium dioxide photocatalysts (TiO$_2$), has applied for groundwater remediation, degradation of hazardous materials, and environment cleanup [1–3]. However, the wide band gap of TiO$_2$ for anatase crystal structure requires UV light and occupied less than 10% energy in solar spectrum for the excitation of electron-hole pairs [4], which restricts the application of TiO$_2$ because of low photo quantum efficiency.

Various metals such as Ag have been doped into the TiO$_2$ lattice to shift its absorption from UV to visible light, and doping improved their photocatalytic activities [5]. In addition, literatures also fabricated the nanotube array or hybrid structures of element-doped-TiO$_2$ to enhance

the photocatalytic activity [6, 7]. However, none of them gave satisfactory results due to their thermally instability and increased carrier trapping [8]. Relatively, the doping of anion on TiO$_2$ such as nitrogen and carbon element doped and codoped has considerable effect on increasing its photocatalytic activity [9–14], in which, the nitrogen seems to be the most effective dopant due to its similar size to oxygen and metastable defect complex, as well as small ionization energy [15], and N-doped TiO$_2$ (N-TiO$_2$) has an advantage on photocatalytic activity [16, 17]. Hence, literatures focused on discussing the structure of N-TiO$_2$ using the X-ray photoelectron spectroscopy (XPS), electron spin resonance, or X-ray absorption near edge structure. Some reports claim that the band gap of the N-TiO$_2$ is reduced due to a rigid valence band shift upon doping [18], others attributed the observed

absorption of visible light by N-TiO$_2$ to the excitation of electrons from localized N-impurity states in the band-gap [8, 19]. In general, the change in banding structure of N-TiO$_2$ was attributed to the N interstitial doping, N substitution, and O vacancy [20–22]. However, till now the structure of N-TiO$_2$ is still under debate. The preparatory methods and conditions such as nitrogen precursor and sintering temperature may considerably affect the nitrogen state in the doped TiO$_2$ [19, 23]. But, only few systematic discussions have been found regarding the dominated factor ratio of N to Ti and calcination temperature for the activity of N-TiO$_2$, simultaneously.

In other words, it is necessary to understand the chemical fine-tuning and further optimization of the visible-light photocatalytic activity of N-TiO$_2$. The goal of this study is (1) to develop a simple method for the synthesis of N-TiO$_2$ nanomaterials using facie method at various conditions of nitrogen precursor amounts and composite calcination temperatures, (2) characterization of N-TiO$_2$ composite materials, (3) carried out the photocatalytic activity of as prepared N-TiO$_2$ under visible light.

Ethylene is a plant hormone that controls many plant responses, and its higher concentration can affect the food and horticultural product industry [24], safe handling, and the parent compound of important environmental contaminants, and the photocatalytic activity for the degradation was quite different from that of volatile chlorinated organic compounds such as trichloroethylene [25]. Therefore, batch experiments were conducted for the removal of ethylene to evaluate the N-TiO$_2$ photoactivity under visible light irradiation and have also been compared with that of commercial photocatalysts Degussa P25. Materials characterizations have been performed through specific surface area analysis, X-ray diffraction (XRD), scanning electron microscope (SEM), electron Spectroscopy for Chemical Analysis (ESCA), and diffuse reflectance ultraviolet-visible absorption spectra (DRS UV-vis).

2. Materials and Methods

2.1. Chemicals and Synthesis of N-TiO$_2$ Composite. All the chemicals were used as procured without further purification. Commercial photocatalyst P25 was purchased from Degussa. Ammonium hydroxide (NH$_4$OH, 33 wt%), titanium tetraisopropoxide (TTIP), and absolute ethanol (99.8%) were procured from J. T. Baker. Synthesis procedure of N-TiO$_2$ composite was modified as reported in literatures [16, 26], and ammonium hydroxide was chosen as a nitrogen precursor. Different amounts of ammonium hydroxide (0–200 mL) and DI water (200–0 mL) were mixed with absolute ethanol (200 mL) in a flask, and then a 400 mL ammonia solution (concentration 0–8.4 M) was obtained. The 10 ml TTIP was added dropwise into the ammonia solution and stirred vigorously for 4 h at 4°C in a water bath. After that the hydrolysis and condensation reaction was kept on stirring for 24 h at room temperature, and then the sol-gel solutions stood to 24 h in aged conditions. The ensuing colloid was then centrifuged and washed thoroughly with distilled water to remove the residual reactants. The final precipitate was dried

at 105°C overnight in air and calcined at various temperatures for 5 h to obtain the final N-TiO$_2$ composite. The synthesized N-TiO$_2$ composites were labeled as N_xT_y, where x and y represent the amount (mL) of ammonium hydroxide added during the synthesis procedure and calcinations temperature (unit is 100°C per scale), respectively. For example, the $N_{150}T_5$ catalyst indicates the addition of 150 mL ammonium hydroxide during the sol-gel procedure of amorphous N-TiO$_2$ catalyst, followed by its calcination at 500°C temperature. Pure TiO$_2$ catalyst was named as $N_{00}T_y$ (x means "zero"), and there was not any addition of ammonium hydroxide during synthesis procedure, such that N_0T_3 refers to the pure TiO$_2$ catalyst which was calcined at 300°C temperature.

2.2. Characterization of Composite. The composite was characterized by means of XRD, DRS UV-vis, XPS, and specific surface area. XPS were recorded on an ESCA spectrometer (ULVAC-PHI, PHI 5000, Japan) operated at 150 W and were used to investigate the surface properties in the valence band of the composite. The shift of the binding energy due to relative surface charging was corrected using the C 1s as an internal standard. The optical absorption responses of composite were obtained from the pressed disk composite using UV-vis (Hitachi, U-3900H, Japan) equipped with an integrated sphere, and BaSO$_4$ was used as a reference. Specific surface areas of samples were obtained by the Brunauer-Emmett-Teller (BET) method using nitrogen adsorption apparatus (Micromeritics ASAP 2020, USA). Samples were degassed at 150°C for 2 h prior to the measurements. The crystal phases of the composites were analyzed by XRD (PANalytical X'Pert Pro MRD, USA) with Cu-Ka radiation and diffraction angle range of 2θ which is 20° to 80°. The crystal size was determined according to Scherrer's equation and fraction of anatase phase in the mixture was calculated by formula proposed by Spurr [27].

2.3. Photocatalytic Activity of N-TiO$_2$. During this study, removal ethylene was studied in batch experiment modes to evaluate the photocatalytic activity of N-TiO$_2$ samples as well as commercial photocatalyst P25. All the powders (0.5 g) were coated onto the flask bottle (catalyst film was kept at 1 mg/cm^2) and caped with sleeve stoppers. The constant ethylene was injected into the flask to get initial ethylene concentration (about 140 or 85 ppmv in different test); a 150 μL aliquot regularly was withdrawn and injected into gas chromatograph equipment equipped with flame ionization detector (PerkinElmer Clarus 500, USA) to analyze the ethylene concentration. The visible illumination was provided by six three-colored fluorescent lamps (March T5-8W/865), located above the flasks equipped with a filter to cut the UV light region. The visible irradiance 610 nm was determined by detector (international light SED005) and about 0.62 mW/cm^2 at the bottom of flask.

3. Result and Discussions

3.1. BET, XRD, and SEM Analysis. The characteristics of composites including surface area, anatase phases, and crystallite size are summarized in Table 1 and Figure 1, in which, the

TABLE 1: Characteristics and rate constant of N-doped TiO_2 prepared at various N/Ti ratio and calcinations temperature.

| Sample | BET | | | | XRD | | SEM | UV-vis | | Activity |
	Specific surface area m²/g	Pore size nm	Pore volume cm³/g	Adsorption type[a] cm³/g	Phase content[b] A/R/B (%)	Crystalline size[c] nm	Size nm	Band gap[d] Eg1 (eV)	Eg2 (eV)	Rate constant ×10⁻² h⁻¹
$N_{00}T_2$	258.9	3.4	0.28	IV	78/00/22	14	—	—	—	—
$N_{00}T_3$	144.7	4.8	0.24	IV	79/00/22	17	—	2.03	2.99	—
$N_{00}T_4$	70.1	5.3	0.25	IV	82/00/18	24	—	—	3.04	—
$N_{00}T_5$	65.8	6.2	0.17	IV	86/00/14	55	22	—	3.05	0.63*
$N_{00}T_6$	19.5	9.6	0.08	IV	92/08/00	113	—	—	2.91	—
$N_{00}T_7$	0.5	18.3	0.01	V	28/72/00	138	—	—	2.87	—
$N_{00}T_8$	0.2	25.9	0.00	V	06/94/00	155	—	—	—	—
$N_{50}T_3$	144.8	4.8	0.24	IV	100/00/0	31	—	2.51	3.18	1.72#
$N_{100}T_3$	231.7	3.9	0.28	IV	100/00/0	28	—	2.51	3.06	1.09#
$N_{150}T_3$	186.1	4.0	0.27	IV	100/00/0	27	—	2.46	3.12	1.93# 0.87*
$N_{200}T_3$	260.4	3.5	0.27	IV	100/00/0	25	—	2.52	3.05	1.29*
$N_{150}T_2$	319.9	3.2	0.22	IV	—	—[e]	—	—	—	—
$N_{150}T_4$	61.0	6.6	0.16	IV	100/00/0	36	—	2.38	3.10	1.50*
$N_{150}T_5$	45.3	6.9	0.13	IV	100/00/0	37	21.3	2.39	3.13	1.76*
$N_{150}T_6$	34.2	9.3	0.11	IV	100/00/0	62	—	—	3.01	1.54*
$N_{150}T_7$	0.8	29.5	0.03	V	78/22/00	108	—	—	2.92	0.01*
$N_{150}T_8$	1.6	39.7	0.04	V	58/42/00	113	—	—	2.92	0.00*
P25	51.2	18.7	0.25	IV	82/18/00	62	—	—	3.04	0.47*

[a] Adsorption isotherm type and hysteresis loop were based on the IUPAC manual; [b] A, R, and B denote anatase, rutile, and brookite, respectively; [c] from XRD data using Scherer formula; [d] the band gap is determined by the plot of $(\alpha h\nu)^{1/2}$ versus photon energy, as shown in Figure 4; [e] no obvious characteristic pattern of crystal to calculate the size; * experimental conditions: reaction temp. = 20°C, R.H. = 53%, $[C_2H_4]_{initial}$ = 85 ppmv, light intensity = 0.62 mW/cm²; # experimental conditions: reaction temp. = 20°C, R.H. = 63%, $[C_2H_4]_{initial}$ = 140 ppmv, light intensity = 0.62 mW/cm².
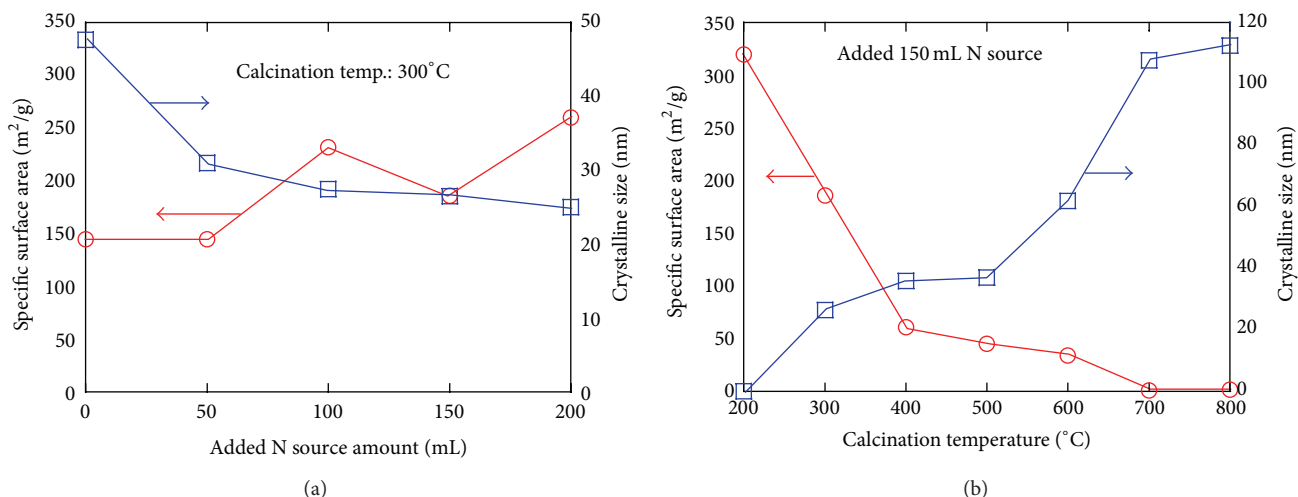
FIGURE 1: The specific surface area of N-TiO$_2$ samples as a function of (a) the various ammonium hydroxide amounts added and (b) calcinations temperature.

crystallite size and phase content of sample is calculated using the Scherrer equation from XRD peak position and full width half maximum [27]. Comparing Figure 1(a) with Figure 1(b), the unobvious change in the BET surface area and crystalline size of samples were observed after the addition of N precursor amounts. However, the clear changes in composites at different calcination temperatures depicted that the dominant factor for surface area and crystalline size of catalysts are calcination temperature, not the addition of N amounts. The pore size and pore volume of composite relative to surface area decreased with the increase of the calcination temperature, and this result is attributed to the pores collapsed and bigger crystallites aggregation of catalyst [28].

The XRD patterns of N-TiO$_2$ samples in different conditions are shown in Figure 2. The diffraction peaks marked with letters "A" and "R" on the figure corresponds to the anatase and rutile phase, respectively. In Figure 2(a), the major peak of 2 theta at about 25.5° corresponding to crystal plane (101) of anatase, which became thinner and the relative intensity was increased with calcination temperature. Such stronger crystalline flair of catalyst would enhance its photoactivity. The XRD patterns of N-TiO$_2$ synthesized with different nitrogen precursors presented in Figure 2(b) have also shown the similar results. It was also depicted that the nitrogen precursor amount did not significantly affect the N-TiO$_2$ crystal phase and crystal size.

The N-TiO$_2$ catalyst (N$_{150}$T$_3$) shows great effect on the photoactivity and also prevents the conversion of N-doped amount into nitrogen gas during calcination process. This sample synthesized with 150 mL N precursor was tested to investigate the effects of calcination temperature and the result is presented in Figure 2(c).

In Figures 2(a) and 2(c), the anatase phase on pure and N-doped TiO$_2$ sample started to appear at 200°C and 300°C calcination temperatures, respectively. The phase transformation from anatase to rutile was observed after the 600°C and 700°C calcination temperatures. This result can be implied that the nitrogen-doped catalyst retarded the phase transformation [10]. Such higher thermal stability could elevate the

anatase crystallinity and promoted the photo-induced charge separation and transportation [29]. The interesting brookite phase was only observed in pure TiO$_2$ (see Figure 2(a)) and disappeared as the beginning of rutile phase, and further the inhibited form of the brookite phase in the N-TiO$_2$ was implied (Figure 2(c)), since the addition of nitrogen in N-TiO$_2$ catalyst. Figures 2(b) and 2(c) showed that the N-doped TiO$_2$ samples had typical peaks of polycrystalline anatase structure and rutile without any detectable dopant related peaks, such as TiN, which was possibly due to the movement of dopant ions either into interstitial positions or substitutional sites of the TiO$_2$ structure or ion concentration, was detected to be too low [30].

The morphology and particle size of the N-TiO$_2$ (N$_{150}$T$_5$) and pure TiO$_2$ (N$_{00}$T$_5$) samples can be obtained from an examination of the SEM image (Figure 3). Single particle in agglomerates in both of them exhibited uniform spherical shape; the size was in range from 20 to 25 nm and a narrow size distribution appeared. Both of these sizes were slightly smaller than the crystallite sizes determined from the XRD in Figure 1(b). The results of similar size and morphology also indicated that the N precursor did not have significant effect on the particle size and shape of TiO$_2$ catalyst.

3.2. DRS UV-Vis and ESCA. In this study, the N-TiO$_2$ powders sintered below 600°C, all exhibited a pale yellow color which suggests its ability to absorb light in the visible region [31]. However, Qiu and Burda infer that the obtained UV-vis spectra that localized defect states may also play a role in providing visible light activity [32]. Optical absorption spectra of the N-TiO$_2$ and Degussa P25 samples are shown in Figure 4, and the absorption at wavelengths shorter than 400 nm can be assigned to the intrinsic band gap absorption of TiO$_2$. A significant shift of the absorption edge to a lower energy in the visible-light region was observed for N-doped TiO$_2$. This result indicates that band-gap narrowing has successfully been achieved by the doping of N into the TiO$_2$ lattice, presumably due to the modification of the band structure
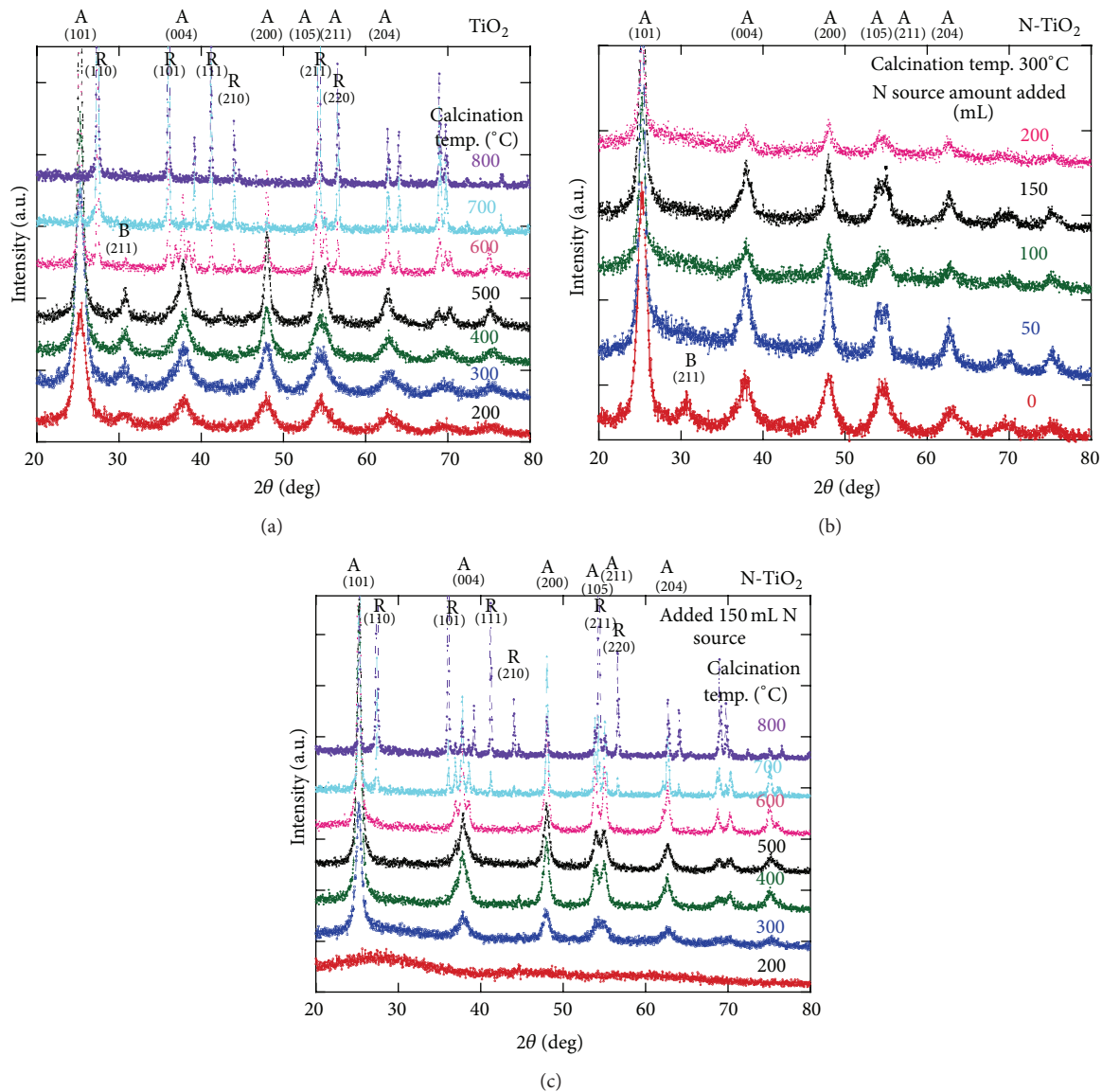
(a)

(b)

(c)

FIGURE 2: XRD pattern of (a) pure TiO_2 calcined at different temperature, (b) N-TiO_2 samples synthesized in different loading of ammonium hydroxide amounts, and (c) N-TiO_2 samples calcined at different temperature.
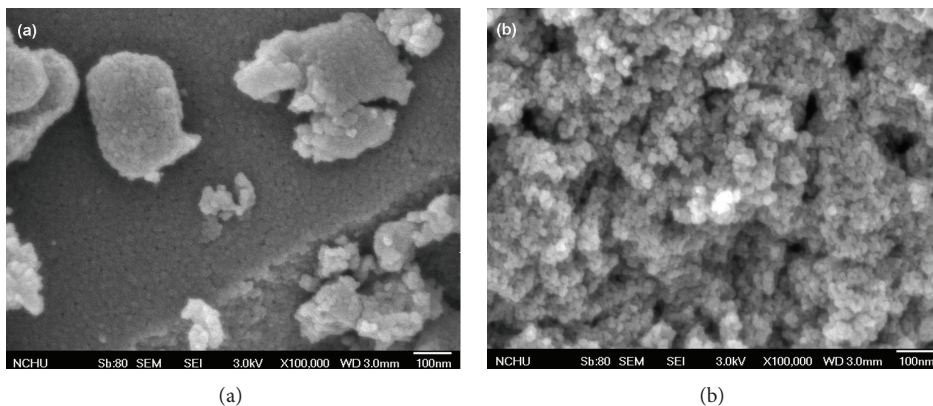

(a)

(b)

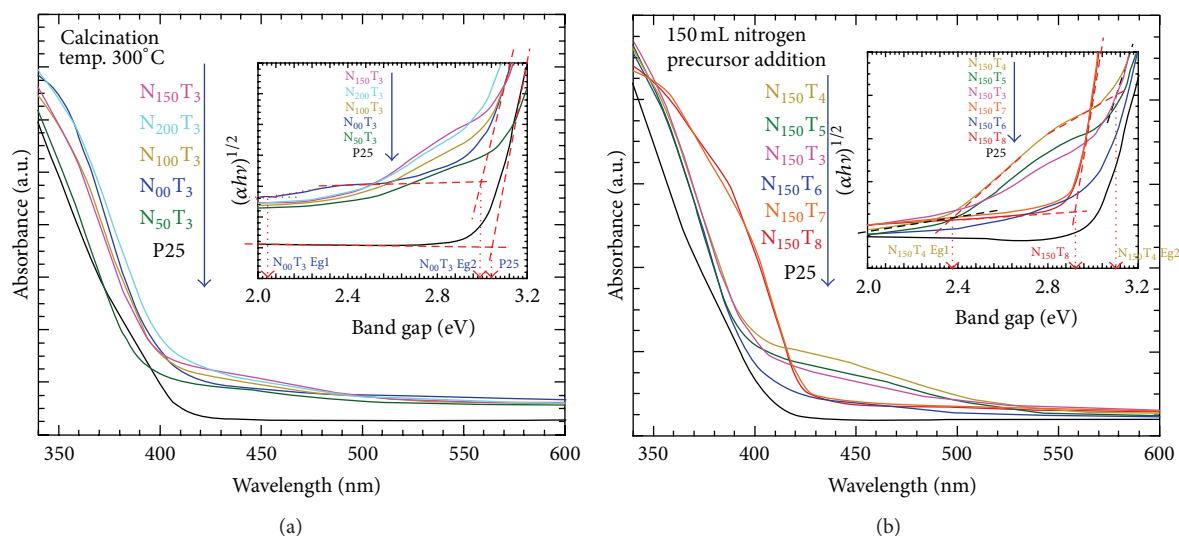FIGURE 3: SEM images of (a) pure TiO_2 and (b) N-TiO_2 catalyst.

FIGURE 4: The UV-vis adoption pattern of N-TiO$_2$ (a) prepared with various ammonium hydroxide amount added and (b) calcined at different temperature.

[33]. The absorption spectra of the N-doped TiO$_2$ samples show a stronger absorption than undoped TiO$_2$ as well as P25 in the UV-vis light region and a red shift in the band gap transition except N$_{50}$T$_3$ sample. The red shift is ascribed possibly to the oxygen vacancy [34] or the fact that N doping can narrow the band gap of the TiO$_2$ [35, 36]. Generally, the photocatalytic activity is proportional to the photo numbers absorbed by photocatalyst per second and the efficiency of the band gap transition [28], the N doping expand the wavelength response range of TiO$_2$ into the visible region and also increased the number of photo-generated electrons and holes to enhance the photocatalytic performance of N-TiO$_2$. The enhanced activity in N-TiO$_2$ catalysts also was demonstrated in Figure 6. Figure 4(a) revealed that the absorbance increases with increasing added nitrogen precursor amounts of N-TiO$_2$ synthesized condition.

Unfortunately, such absorbance is not proportional to its photoactivity. Further, the UV-vis absorbance spectra of appropriate samples with different calcined temperature are shown in Figure 4(b). The absorbance of all N-TiO$_2$ samples in the visible region is higher than that of P25 and may be ascribed to the fact that the narrowing of band gap as well as localized defect resulted from N doping and calcination. Higher than 700°C calcination, the N-TiO$_2$ powders show a significant red shift in the band gap transition due to the formation of rutile phase and growth of TiO$_2$ crystallite. However, interestingly, amorphous N$_{150}$T$_2$ powders also showed a greatest red shift. As the calcination temperature increased from 300°C to 600°C, the intensive absorption of N$_{150}$T$_4$, N$_{150}$T$_3$, and N$_{150}$T$_5$ were observed in the visible region between 400 and 500 nm, which is the typical absorption feature of nitrogen doped TiO$_2$ [10], whereas it was not observed on N$_{150}$T$_6$ sample even if N$_{150}$T$_6$ appeared better photoactivity than N$_{150}$T$_3$. However, the aforementioned result could not possibly provide a definite relation between absorbance and photoactivity of as-prepared sample, which is due to that the absorption features in the visible range

originated from color centers through doping processes or posttreatments rather than by narrowing of the band gap [32, 37]. Literature also reports the intensive absorption of ion doped TiO$_2$ that can be assigned to oxygen vacancies produced by thermal treatment, which form localization levels within the band gap [34]. Moreover, the origin of visible light absorption originated from N and O vacancies suggested that the N dopants can only affect the absorption below 500 nm wavelength, while the O vacancies are responsible for the induced absorption at wavelengths above 500 nm [38].

ESCA analyses of N 1s and Ti 2p were performed on pure TiO$_2$, P25, and N-TiO$_2$ catalysts and results are shown in Figure 5. In Figure 5(a), the binding energy (BE) peaks corresponding to N 1s core-levels for N-TiO$_2$ samples prepared with various amounts of N precursor and calcined at 300°C are observed one major peak at 398–402 eV. However, sometime the binding energy observed at 400 eV is ascribed to N atoms which are incorporated into the TiO$_2$ lattice as N$_2$ molecules [33]. Saha and Tompkins investigated the N 1s ESCA spectra during the oxidation of TiN and assigned the peaks as atomic β-N (396 eV) and molecularly chemisorbed γ-N2 (400 eV and 402 eV) [31]. Those different N 1s spectral features are still debated and dependent on different preparation methods and conditions [35]. Further, the Ti 2p$_{1/2}$ and Ti 2p$_{3/2}$ spin-orbital splitting photoelectrons for anatase TiO$_2$ were located at binding energies of about 464.0 and 458.2 eV, respectively, which were assigned to the presence of typical Ti^{4+}. Same Ti 2p peaks are located at same binding energy and distribution (Figure 5(b)), because the N precursor amount was not a dominating factor in the electronic structure of N-TiO$_2$, although the different activity of N-TiO$_2$ synthesized in N precursor amount is shown in Figure 6(a).

The content of nitrogen were maintained in all the composites smaller than 1% and found decreased with increasing calcination temperature as shown in Figure 5(c), which may be due to the replacement of N in the matrix by O and
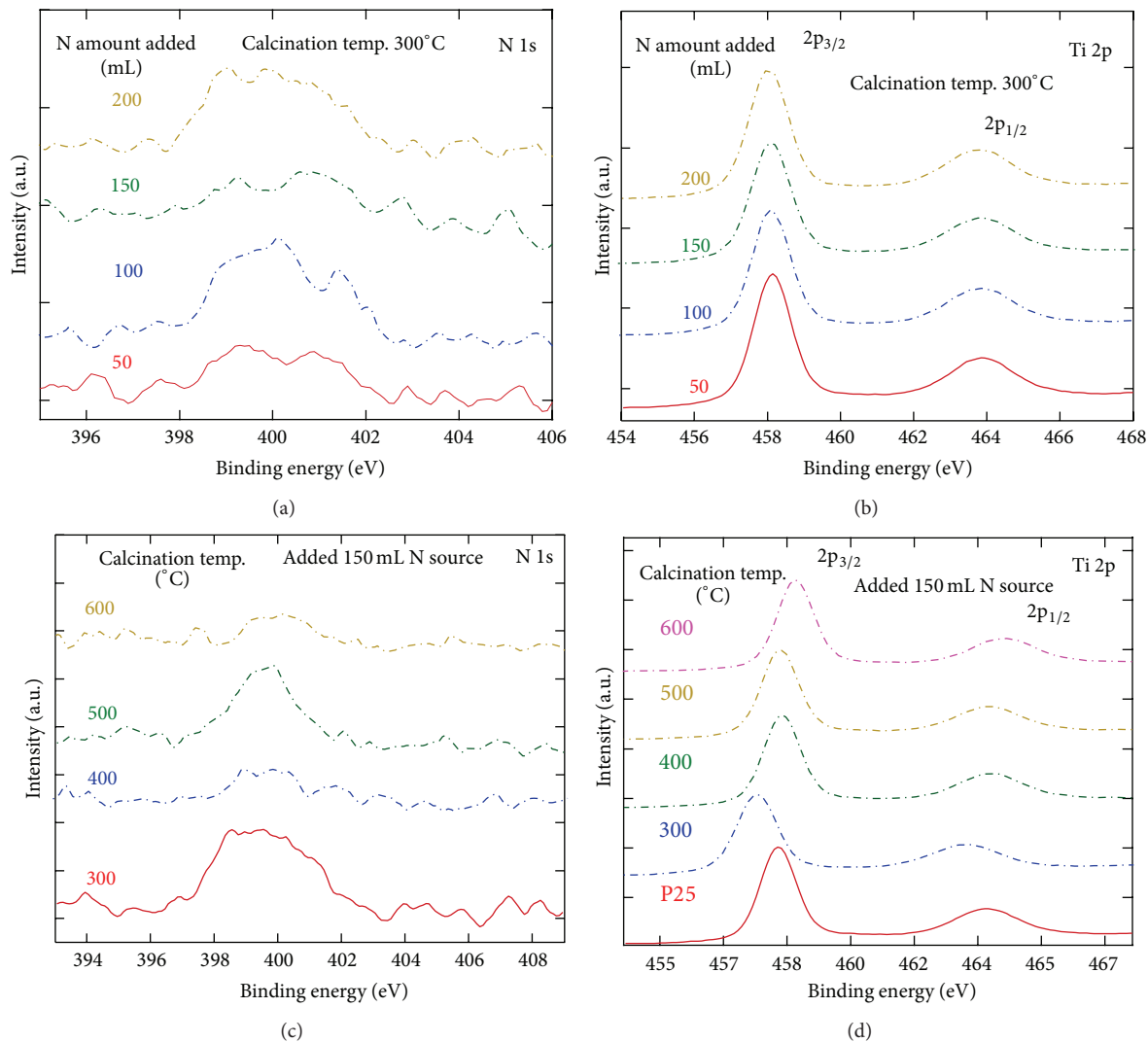
(a)

(b)

(c)

(d)

FIGURE 5: The XPS spectra for N-TiO$_2$ samples, ((a) and (c)) N 1s and ((b) and (d)) Ti 2p.
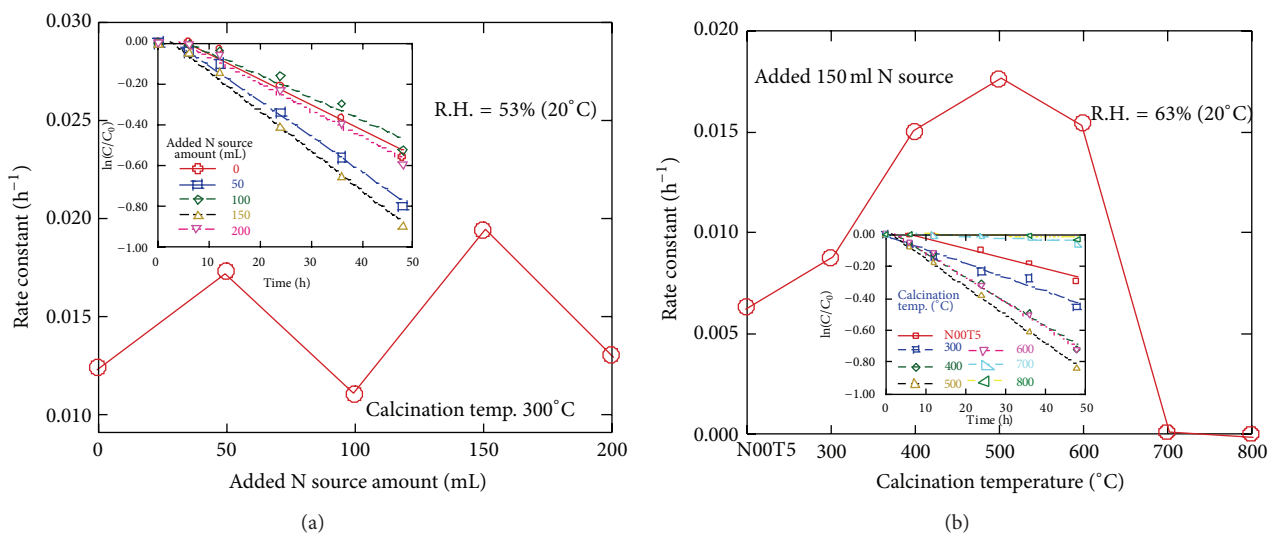

(a)

(b)

FIGURE 6: Photocatalytic reaction of N-TiO$_2$ samples as a function of (a) the various ammonium hydroxide amount added and (b) the various calcination temperature.

transform to nitride result in lower N concentrations [32]. Literature reports that the N dopant was adsorbed NO or bond to oxygen vacancy site in interstitial formation (Ti-O-N), especially at such low N doping concentrations [39]. The N 1s peaks also shifted towards higher binding energy with increasing calcination temperature level and appeared as different distribution. However, high sintering temperature can also cause the loss of dopants from N-TiO$_2$ catalyst. Therefore, an appropriate sintering temperature would be more important to the activity of N-doped TiO$_2$ [32]. At the same time, in Figure 5(d), the Ti 2p peaks undergone a shift towards higher binding energy with increasing calcination temperatures. This indicates the lowering of electronic density around the central Ti ion by introducing more O next to Ti [32]. The above mentioned binding energy shift pointed out that the calcination temperature may be a dominating factor in the electronic structure of N-TiO$_2$, and this is found consistent with XRD and BET analyses, and thus the calcination temperature would be key factor for the characteristics of N-TiO$_2$ based on synthesized method of this study.

3.3. Photoactivity of N-TiO$_2$ under Visible Light Illumination. Figure 6 shows the photocatalytic performances for ethylene removal over the various N-TiO$_2$ and pure TiO$_2$ in batch reactions under the visible light irradiation. The rate of photocatalytic oxidation has been described by a pseudo-first-order equation, as presented in (1) [24] and the rate constant values are given in Table 1. Consider

$$\ln\left(\frac{C_0}{C_t}\right) = -kt, \tag{1}$$

where C_0 is the initial concentration of ethylene, C_t is the ethylene at time t, and k is the apparent pseudo first photocatalytic oxidation rate constant. Examination of (1) suggests that the apparent pseudo first photocatalytic oxidation rate constant k can be determined experimentally from a plot of $\ln(C_0/C_t)$ versus time, which has a slope of $-k$. All the photocatalytic oxidation rate constants (k) of catalysts are summarized in Table 1. Figure 6(a) shows the effect of N-TiO$_2$ synthesized at different nitrogen precursor with 300°C calcination temperature, and the order of the reaction rates (Table 1) was N$_{150}$T$_3$, N$_{50}$T$_3$, N$_{200}$T$_3$, N$_{00}$T$_3$, and N$_{100}$T$_3$. Then, the N-TiO$_2$ catalyst was synthesized at 150 mL nitrogen precursor and sintered from 300°C to 800°C temperatures to investigate the effects of sintering temperature on N-TiO$_2$ photoactivity. In Figure 6(b), the activity of N$_{00}$T$_5$ (Pure TiO$_2$ sintered at 500°C temperature) was found better than commercial TiO$_2$ P25 under visible light irradiation due to the transfer of electron and hole between two phases (mix phase of anatase with few fraction of brookite) which is ascribed to the oxygen vacancy resulted from the calcination at 500°C [40].

Moreover, the optimized N$_{150}$T$_5$ photocatalyst has shown better ethylene degradation than undoped N$_{00}$T$_5$ and others. Based on the experimental results, the nitrogen doping would improve the photoactivity of undoped TiO$_2$ under visible light irradiation. Both N$_{150}$T$_7$ and N$_{150}$T$_8$ showed less photoactivity due to the existence of rutile phases and the tiny

BET surface area as shown in Figure 1(b). However, the largest specific surface area of N$_{150}$T$_3$ should have theoretically better photoactivity for the removal of ethylene due to the abundance of active sites. More effectiveness of N$_{150}$T$_5$ was also observed for visible region of solar illumination and there are some other facts that may affect photoactivity of TiO$_2$ under visible illumination such as O vacancy resulted from calcination and N impurity acted as light sensitization [41, 42]. We have found that not only is the N-TiO$_2$ sample oxygen-deficient but also it involves a small amount of N-doped. N doping in TiO$_2$ was in interstitial formation (Ti-O-N) and that function retarded the reoxidation of oxygen deficient TiO$_2$, which is essentially indispensable for visible light sensitization [36].

4. Conclusions

N-TiO$_2$ nanocatalysts can be developed directly by so-gel method under the conditions: 150 mL ammonium hydroxide precursor added and 500°C calcination temperature. The ethylene removal efficiency was dependent on the optimal contents of nitrogen precursor, surface area, and oxygen vacancy and good crystallization resulted from the adapted calcination temperatures [32, 43]. The N-TiO$_2$ powders showed a stronger absorption in the visible light region from 400 to 500 nm wavelength, which was possibly due to narrow band gap by mixing of N 2p states with O 2p states on the top of the valence band or a creation of N-induced mid-gap level. Other more intensive absorption in the visible light region longer than 500 nm wavelength is ascribed to oxygen vacancy resulted from the calcination and N doping. The N-doping wet-method has an advantage on photocatalytic activity as compared to metal ion doping (thermally instability). In addition, the doped TiO$_2$ enhanced the photoactivity may be further investigated in depth [32], such as use of first principle calculations, origin of the enhanced visible light absorption in N-doped anatase TiO$_2$ [44], or approaches to combine TiO$_2$ with another mineral such as schorl.

Conflict of Interests

The authors declare that there is no conflict of interests regarding the publication of this paper.

Acknowledgment

References

[1] Y.-H. Lin, H.-H. Tseng, M.-Y. Wey, and M.-D. Lin, "Characteristics, morphology, and stabilization mechanism of PAA250K-stabilized bimetal nanoparticles," *Colloids and Surfaces A: Physicochemical and Engineering Aspects*, vol. 349, no. 1–3, pp. 137–144, 2009.

[2] Y.-H. Lin, H.-H. Tseng, M.-Y. Wey, and M.-D. Lin, "Characteristics of two types of stabilized nano zero-valent iron and transport in porous media," *Science of the Total Environment*, vol. 408, no. 10, pp. 2260–2267, 2010.

[3] Y.-T. Lin, C.-H. Weng, and T. W. Tzeng, "Photocatalysis and catalytic properties of nano-sized N-TiO$_2$ Catalyst synthesized by Sol-gel methods," *Journal of Advanced Oxidation Technologies*, vol. 13, no. 3, pp. 297–304, 2010.

[4] T. C. Jagadale, S. P. Takale, R. S. Sonawane et al., "N-doped TiO$_2$ nanoparticle based visible light photocatalyst by modified peroxide sol-gel method," *Journal of Physical Chemistry C*, vol. 112, no. 37, pp. 14595–14602, 2008.

[5] L. Sun, J. Li, C. Wang et al., "Ultrasound aided photochemical synthesis of Ag loaded TiO$_2$ nanotube arrays to enhance photocatalytic activity," *Journal of Hazardous Materials*, vol. 171, no. 1–3, pp. 1045–1050, 2009.

[6] Y.-K. Lai, J.-Y. Huang, H.-F. Zhang et al., "Nitrogen-doped TiO$_2$ nanotube array films with enhanced photocatalytic activity under various light sources," *Journal of Hazardous Materials*, vol. 184, no. 1–3, pp. 855–863, 2010.

[7] Y. Tang, P. Wee, Y. Lai et al., "Hierarchical TiO$_2$ nanoflakes and nanoparticles hybrid structure for improved photocatalytic activity," *The Journal of Physical Chemistry C*, vol. 116, no. 4, pp. 2772–2780, 2012.

[8] M. Sathish, B. Viswanathan, R. P. Viswanath, and C. S. Gopinath, "Synthesis, characterization, electronic structure, and photocatalytic activity of nitrogen-doped TiO$_2$ nanocatalyst," *Chemistry of Materials*, vol. 17, no. 25, pp. 6349–6353, 2005.

[9] B. F. Abramović, D. V. Šojić, V. B. Anderluh, N. D. Abazović, and M. I. Čomor, "Nitrogen-doped TiO$_2$ suspensions in photocatalytic degradation of mecoprop and (4-chloro-2-methylphenoxy)acetic acid herbicides using various light sources," *Desalination*, vol. 244, no. 1–3, pp. 293–302, 2009.

[10] Y. Ma, J. Zhang, B. Tian, F. Chen, and L. Wang, "Synthesis and characterization of thermally stable Sm,N co-doped TiO$_2$ with highly visible light activity," *Journal of Hazardous Materials*, vol. 182, no. 1–3, pp. 386–393, 2010.

[11] S.-I. In, P. C. K. Vesborg, B. L. Abrams, Y. Hou, and I. Chorkendorff, "A comparative study of two techniques for determining photocatalytic activity of nitrogen doped TiO$_2$ nanotubes under visible light irradiation: photocatalytic reduction of dye and photocatalytic oxidation of organic molecules," *Journal of Photochemistry and Photobiology A: Chemistry*, vol. 222, no. 1, pp. 258–262, 2011.

[12] Z. Xie, Y. Zhang, X. Liu et al., "Visible light photoelectrochemical properties of N-doped TiO$_2$-nanorod arrays from TiN," *Journal of Nanomaterials*, vol. 2013, Article ID 930950, 8 pages, 2013.

[13] Y.-T. Lin, C.-H. Weng, Y.-H. Lin, C.-C. Shiesh, and F.-Y. Chen, "Effect of C content and calcination temperature on the photocatalytic activity of C-doped TiO$_2$ catalyst," *Separation and Purification Technology*, vol. 116, pp. 114–123, 2013.

[14] X. Cheng, H. Liu, Q. Chen, J. Li, and P. Wang, "Construction of N, S codoped TiO$_2$ NCs decorated TiO$_2$ nano-tube array photoelectrode and its enhanced visible light photocatalytic mechanism," *Electrochimica Acta*, vol. 103, pp. 134–142, 2013.

[15] C. H. Park, S. B. Zhang, and S.-H. Wei, "Origin of p-type doping difficulty in ZnO: the impurity perspective," *Physical Review B*, vol. 66, no. 7, Article ID 073202, 2002.

[16] S. Sato, R. Nakamura, and S. Abe, "Visible-light sensitization of TiO$_2$ photocatalysts by wet-method N doping," *Applied Catalysis A: General*, vol. 284, no. 1-2, pp. 131–137, 2005.

[17] Y.-T. Lin, C.-H. Weng, H.-J. Hsu, Y.-H. Lin, and C.-C. Shiesh, "The synergistic effect of nitrogen dopant and calcination temperature on the visible-light-induced photoactivity of N-doped TiO$_2$," *International Journal of Photoenergy*, vol. 2013, Article ID 268723, 13 pages, 2013.

[18] R. Asahi, T. Morikawa, T. Ohwaki, K. Aoki, and Y. Taga, "Visible-light photocatalysis in nitrogen-doped titanium oxides," *Science*, vol. 293, no. 5528, pp. 269–271, 2001.

[19] C. Di Valentin, E. Finazzi, G. Pacchioni et al., "N-doped TiO$_2$: theory and experiment," *Chemical Physics*, vol. 339, no. 1–3, pp. 44–56, 2007.

[20] O. Diwald, T. L. Thompson, T. Zubkov, E. G. Goralski, S. D. Walck, and J. T. Yates Jr., "Photochemical activity of nitrogen-doped rutile TiO$_2$ (110) in visible light," *Journal of Physical Chemistry B*, vol. 108, no. 19, pp. 6004–6008, 2004.

[21] X. Chen and C. Burda, "Photoelectron spectroscopic investigation of nitrogen-doped titania nanoparticles," *Journal of Physical Chemistry B*, vol. 108, no. 40, pp. 15446–15449, 2004.

[22] S. Hu, A. Wang, X. Li, and H. Löwe, "Hydrothermal synthesis of well-dispersed ultrafine N-doped TiO$_2$ nanoparticles with enhanced photocatalytic activity under visible light," *Journal of Physics and Chemistry of Solids*, vol. 71, no. 3, pp. 156–162, 2010.

[23] Y. Zhao, X. Qiu, and C. Burda, "The effects of sintering on the photocatalytic activity of N-Doped TiO$_2$ nanoparticles," *Chemistry of Materials*, vol. 20, no. 8, pp. 2629–2636, 2008.

[24] S. Y. Ye, Q. M. Tian, X. L. Song, and S. C. Luo, "Photoelectrocatalytic degradation of ethylene by a combination of TiO$_2$ and activated carbon felts," *Journal of Photochemistry and Photobiology A: Chemistry*, vol. 208, no. 1, pp. 27–35, 2010.

[25] S. Yamazaki, S. Tanaka, and H. Tsukamoto, "Kinetic studies of oxidation of ethylene over a TiO$_2$ photocatalyst," *Journal of Photochemistry and Photobiology A: Chemistry*, vol. 121, no. 1, pp. 55–61, 1999.

[26] S. Sato, "Photocatalytic activity of NO$_x$-doped TiO$_2$ in the visible light region," *Chemical Physics Letters*, vol. 123, no. 1-2, pp. 126–128, 1986.

[27] R. A. Spurr, "Quantitative analysis of anatase-rutile mixtures with an X-ray diffractometer," *Analytical Chemistry*, vol. 29, no. 5, pp. 760–762, 1957.

[28] J. Yu, M. Zhou, B. Cheng, and X. Zhao, "Preparation, characterization and photocatalytic activity of in situ N,S-codoped TiO$_2$ powders," *Journal of Molecular Catalysis A: Chemical*, vol. 246, no. 1-2, pp. 176–184, 2006.

[29] Y. Luan, L. Jing, M. Xie et al., "Synthesis of efficient N-containing TiO$_2$ photocatalysts with high anatase thermal stability and the effects of the nitrogen residue on the photoinduced charge separation," *Physical Chemistry Chemical Physics*, vol. 14, no. 4, pp. 1352–1359, 2012.

[30] N. D. Abazović, A. Montone, L. Mirenghi, I. A. Janković, and M. I. Čomor, "TiO$_2$ doped with nitrogen: synthesis and characterization," *Journal of Nanoscience and Nanotechnology*, vol. 8, no. 2, pp. 613–618, 2008.

[31] N. C. Saha and H. G. Tompkins, "Titanium nitride oxidation chemistry: an x-ray photoelectron spectroscopy study," *Journal of Applied Physics*, vol. 72, no. 7, pp. 3072–3079, 1992.

[32] X. Qiu and C. Burda, "Chemically synthesized nitrogen-doped metal oxide nanoparticles," *Chemical Physics*, vol. 339, no. 1–3, pp. 1–10, 2007.

[33] T. Morikawa, R. Asahi, T. Ohwaki, K. Aoki, and Y. Taga, "Bandgap narrowing of titanium dioxide by nitrogen doping," *Japanese Journal of Applied Physics*, vol. 40, no. 6, pp. L561–L563, 2001.

[34] I. Nakamura, N. Negishi, S. Kutsuna, T. Ihara, S. Sugihara, and K. Takeuchi, "Role of oxygen vacancy in the plasma-treated TiO$_2$ photocatalyst with visible light activity for NO removal," *Journal of Molecular Catalysis A: Chemical*, vol. 161, no. 1-2, pp. 205–212, 2000.

[35] Z. Wu, F. Dong, W. Zhao, and S. Guo, "Visible light induced electron transfer process over nitrogen doped TiO$_2$ nanocrystals prepared by oxidation of titanium nitride," *Journal of Hazardous Materials*, vol. 157, no. 1, pp. 57–63, 2008.

[36] T. Ihara, M. Miyoshi, Y. Iriyama, O. Matsumoto, and S. Sugihara, "Visible-light-active titanium oxide photocatalyst realized by an oxygen-deficient structure and by nitrogen doping," *Applied Catalysis B: Environmental*, vol. 42, no. 4, pp. 403–409, 2003.

[37] N. Serpone, "Is the band gap of pristine TiO$_2$ narrowed by anion- and cation-doping of titanium dioxide in second-generation photocatalysts?" *The Journal of Physical Chemistry B*, vol. 110, no. 48, pp. 24287–24293, 2006.

[38] Z. Lin, A. Orlov, R. M. Lambert, and M. C. Payne, "New insights into the origin of visible light photocatalytic activity of nitrogen-doped and oxygen-deficient anatase TiO$_2$," *Journal of Physical Chemistry B*, vol. 109, no. 44, pp. 20948–20952, 2005.

[39] A. Nambu, J. Graciani, J. A. Rodriguez, Q. Wu, E. Fujita, and J. F. Sanz, "N doping of TiO$_2$(110): photoemission and density-functional studies," *Journal of Chemical Physics*, vol. 125, no. 9, Article ID 094706, 2006.

[40] T. Ozawa, M. Iwasaki, H. Tada, T. Akita, K. Tanaka, and S. Ito, "Low-temperature synthesis of anatase-brookite composite nanocrystals: the junction effect on photocatalytic activity," *Journal of Colloid and Interface Science*, vol. 281, no. 2, pp. 510–513, 2005.

[41] M. Batzill, E. H. Morales, and U. Diebold, "Influence of nitrogen doping on the defect formation and surface properties of TiO$_2$ rutile and anatase," *Physical Review Letters*, vol. 96, no. 2, Article ID 026103, 2006.

[42] H. Chen, A. Nambu, W. Wen et al., "Reaction of NH$_3$ with titania: N-doping of the oxide and TiN formation," *The Journal of Physical Chemistry C*, vol. 111, no. 3, pp. 1366–1372, 2007.

[43] H. Fu, L. Zhang, S. Zhang, Y. Zhu, and J. Zhao, "Electron spin resonance spin-trapping detection of radical intermediates in N-doped TiO$_2$-assisted photodegradation of 4-chlorophenol," *Journal of Physical Chemistry B*, vol. 110, no. 7, pp. 3061–3065, 2006.

[44] M. Harb, P. Sautet, and P. Raybaud, "Origin of the enhanced visible-light absorption in N-doped bulk anatase TiO$_2$ from first-principles calculations," *The Journal of Physical Chemistry C*, vol. 115, no. 39, pp. 19394–19404, 2011.

Research Article

Comparison of Adsorption Capability of Activated Carbon and Metal Doped TiO$_2$ for Geosmin and 2-MIB Removal from Water

Aisha Asghar, Zahiruddin Khan, Nida Maqbool, Ishtiaq A. Qazi, and Muhammad Ali Awan

School of Civil and Environmental Engineering, Institute of Environmental Science and Engineering (IESE),
National University of Science and Technology (NUST), Islamabad 44000, Pakistan

Correspondence should be addressed to Zahiruddin Khan; zahirkhan61@gmail.com

This study stemmed from consumer complaints about earthy and musty off-flavours in treated water of Rawal Lake Filtration Plant. In recent years, several novel adsorbents have been developed from nanomaterials for enhancing the contaminant removal efficiency. This paper presents preparation and the use of new adsorbents Pt doped titania and Fe doped titania, for the adsorption capacity of Geosmin and 2-MIB from water under laboratory conditions and their comparison, with most widely used activated carbon, under batch and column experiments. Stock solutions were prepared by using Geosmin and 2-MIB standards, procured by Sigma Aldrich (England). Samples were analysed using SPME-GC-FID. The adsorption of Geosmin and 2-MIB on GAC conformed to the Freundlich isotherm, while that of adsorption on metal doped titania fit equally well to both Langmuir and Freundlich isotherms. Moreover, data, generated for the kinetic isotherm, confirmed that Geosmin and 2-MIB removal is a function of contact time. Breakthrough column tests using 125 mg/L Pt doped titania nanoparticles, coated on glass beads against 700 ng/L of off-flavours, attained later breakthrough and exhaustion points and removed 98% of Geosmin and 97% of 2-MIB at room temperature. All columns could be regenerated using 50 mL 0.1 molar sodium hydroxide.

1. Introduction

Supply of safe and aesthetically pleasing water, for human consumption, is essential for all treatment facilities. A common and recurrent problem in drinking water is the formation of earthy-musty taste and odor [1]. Taste and odor episodes in drinking water are the cause for most consumer complaints [2]. There is growing concern about off-flavour in Rawal Lake Filtration Plant, which intensifies in summer months [3–5]. Sensory analysis detected earthy and musty off-flavours in raw, as well as in treated supplies from this facility. This study focused on Geosmin ($C_{12}H_{22}O$) and 2-MIB ($C_{11}H_{20}O$) as surrogate for earthy and musty off-flavours. Earthy and musty off-flavours are produced as secondary metabolite by two groups of aquatic microorganism: (i) *anabaena* for Geosmin and (ii) *Phormidium* spp. for 2-MIB [6]. Both compounds are semivolatile, saturated tertiary alcohols that can be detected at extremely low concentrations of 6–20 ng/L [7]. The main problem with the presence

of Geosmin/2-MIB is that conventional water treatment processes including coagulation, flocculation, and filtration are inadequate for their removal [8]. Oxidants including $KMnO_4$, ozonation, and UV/H_2O_2 have been tested for removal of odorous compounds [9, 10] but due to the complex tertiary structures of Geosmin and 2-MIB, these are resistant toward oxidation and most aquatic oxidants [11]. Activated carbon in combination with sand media in filtration plants is considered as one of the best available practice for the removal of off-flavours from water, but at relatively higher amount of pollutant levels, its adsorption efficiency drops [12–14]. Literature review reveals that nanoparticles have some advantages in using adsorption processes to solve many environmental issues due to their unique surface and structural properties [15]. A number of studies have been reported on photo catalysis of Geosmin and 2-MIB [16]; however, to the best of our knowledge no previous study has been reported on adsorption of Geosmin and 2-MIB using

Table 1: Method of metal doped-Titania nanoparticles preparation.

Type of doping	Doped element	Method of preparation
Metal doping	Pt	150 mL deionized water + 25 gm. titania + 1 molar ratio PtCl$_4$ Stirred at 250 rpm for 24 hours Suspensions removed and oven dried at 110°C Calcinated at 400°C for 6 hours, grounded, and stored in dark
	Fe	150 mL deionized water + 25 gm titania + 1.5 molar ratio FeCl$_2$ Stirred at 250 rpm for 24 hours Suspensions removed and oven dried at 100°C Calcinated at 350°C for 8 hours, grounded, and stored in dark

metal doped titania nanoparticles. Since metal doping further enhances the adsorption efficiency of nanoparticles [17, 18], this study aimed at comparing activated carbon, Fe-TiO$_2$, and Pt-TiO$_2$ nanoparticles for Geosmin/2-MIB removal, using breakthrough column studies, from synthetic and Rawal Lake Filtration Plant (RLFP), Pakistan, treated water samples.

2. Materials and Methods

2.1. Material Systems. The GC standard of Geosmin and 2-MIB were purchased from Sigma-Aldrich (Germany) at a concentration of 2 mg/L and 10 mg/L in methanol, respectively. Stock solutions were prepared in 10 mL methanol. General purpose reagent titanium (IV) oxide (Riedel-De Haen) was used as a source of titania nanoparticles; ferrous chloride and platinum chloride were purchased from Merck, Germany. Other chemicals including GC grade methanol, dichloromethane (DCM), and wood based granular and powdered activated carbon (Norit C1A) were procured from Acros, Organics, USA.

3. Experimentation

3.1. Synthesis of Nanoparticles. Liquid impregnation method was used to prepare metal doped titania nanoparticles [19] as described in Table 1.

3.2. Scanning Electron Microscopy of Adsorbents. SEM images were measured using JEOL JSM 6460 scanning electron microscope. Microscope operated at an acceleration voltage of 5, 10, and 15 kV and filament current of 60 mA. SEM was performed to find the surface morphology, topography, microstructure, and composition of adsorbents. The porous texture characterization of the samples was obtained by physical adsorption of gases. From N$_2$ adsorption data at −196°C (Autosorb-6B apparatus from Quantachrome [20]) the specific BET surface area (S_{BET}) was determined by applying the Brunauer-Emmett-Teller (BET) equation.

3.3. Analytical Method. Geosmin and 2-MIB were analysed using solid phase microextraction coupled with gas chromatograph-flame ionized detector (SPME-GC-FID). One gram of sodium chloride was placed in a 15 mL vial containing 3 mL of the aqueous sample. The vial was sealed with Teflon-lined septum. The samples were heated to 65°C, and the SPME fiber (divinylbenzene-carboxen-polydimethylsiloxane SPME fiber) was inserted into heads space for 15 min equilibrium adsorption period. The fiber was then withdrawn from the sample and injected into the injection port of Shimadzu 2010 series Gas Chromatograph coupled with FID. The column used was fused silica capillary column with a length of 30 m, inner diameter of 0.32 mm, and wall thickness of 0.5 μm. The column temperature was set at 60°C for 1 min and then raised to 160°C @ 15°C/min, held at 160°C for 1 min, then raised to 200°C @ 10°C/min, again held at 200°C for 1 min, and finally temperature was raised to 260°C and held constant for 1 min. Total program time was 16.67 min. Detector temperature was 280°C while injector was set at 300°C. Split ratio was zero. Nitrogen was the makeup gas and Helium was used as carrier gas. Total flow rate was 6.6 mL/min. The extracts were stable and could be stored for up to two months with no apparent loss of analytes and concentrations as low as 1 ng/L could be detected.

3.4. Synthetic Solutions Preparation. Geosmin and 2-MIB solutions used in this study were prepared in the laboratory by dissolving stock solutions in ultrapure water. This study was aimed at testing adsorbents for their ability to adsorb earthy-musty odorants for the concentrations which are present in lake water. For this reason, sampling was performed from Rawal Lake Filtration Plant (RLFP) in the month of July, when taste and odor episode in treated water was at their maximum levels. RLFP draws raw water from Rawal Lake, Pakistan. Its treatment processes include coagulation, flocculation, sedimentation, sand filtration, and disinfection, which were inadequate to remove taste and odor from water. Average concentration of Geosmin and 2-MIB in treated water samples was 690 ng/L and 678 ng/L, respectively; hence, synthetic solution with 700 ng/L of odorants was prepared for batch adsorption and column adsorption experiments. All reactors were wrapped with aluminium foil during nanoparticle experiments, to restrict photo catalytic activity and to ensure adsorption as the only mechanism of odorant removal.

3.5. Batch Experiments

3.5.1. Adsorption Conditions Optimization. In this study, adsorbent dose, contact time, and stirring rate per minute for Geosmin and 2-MIB were optimized. For optimization of adsorbent dose for Geosmin and 2-MIB removal, adsorption experiments were performed by varying adsorbents doses between 40 mg/L and 200 mg/L in test solutions, containing 700 ng/L initial odorants concentration. In order to determine the equilibrium adsorption time, flasks containing 700 ng/L initial Geosmin and 2-MIB concentrations with optimized adsorbent dose were agitated on the orbital shaker for different time intervals (5, 15, 30, 45, 60, 75, 90, and 120 minutes). Similarly, test solutions were tested for the

Manual flow control valves

Peristaltic pump

Water above media 12 cm

GAC 12 cm

Fe-TiO$_2$ 12 cm

Pt-TiO$_2$ 12 cm

Outlet

Teflon can containing Geosmin and 2-MIB solution
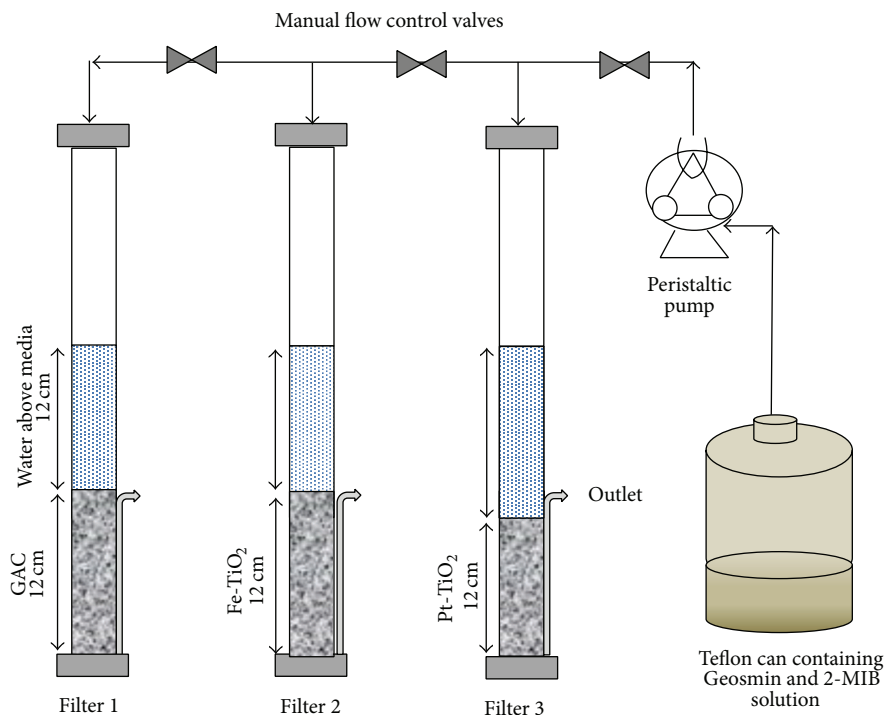
Filter 1

Filter 2

Filter 3

Figure 1: Schematics of the pilot column setup.

best stirring rate (between 25 and 200 rpm), with optimised adsorbent doses and contact time.

3.5.2. Removal Efficiency Calculation. To determine the removal efficiency of selected adsorbents, 100 mL of test solution with initial off-flavours concentration of 700 ng/L was taken in 250 mL conical flask at room temperature. 125 mg of the adsorbents (GAC, Fe, and Pt doped nanoparticles) were added in each test solution and stirred at orbital shaker at 100 rpm for one hour. All the samples were stored in dark brown vials, till final concentration analysis. Samples were subjected to filtration through prewashed 0.45 μm filters, to remove any solid adsorbents residue, prior to the gas chromatographic analysis.

Amount of Geosmin and 2-MIB adsorbed (ng/g) was calculated using [21]

$$q_e = \frac{(C_i - C_s) V}{m},$$

where C_i is the initial analyte concentration, C_s is the residual equilibrium analyte concentrations (ng/L), V is the volume of the solution (mL), and m is the mass of adsorbent (mg) used in test solution.

3.5.3. Adsorption Isotherm Studies. For adsorption studies, 100 mL of the initial test solution of odorant concentrations, varying between 200 and 1200 ng/L, was taken in 1000 mL volumetric flasks and experiments were performed with all optimized conditions. 125 mg metal doped nanoparticles and 160 mg GAC were added to the test solutions and then placed

on an orbital shaker at 100 rpm for 60 minutes and final concentrations were determined, in all removal experiments.

3.5.4. Kinetic Studies. Several models are available to express the mechanism of adsorption of solute onto the adsorbent. For kinetic studies, 500 mg of adsorbent doses was introduced into 1000 mL solutions with initial analytes concentration of 700 ng/L and placed at an orbital shaker at a rotation speed of 100 rpm. Samples were taken at predetermined intervals up to 120 min. The kinetic analysis was carried out at room temperature (25 ± 1°C).

3.6. Pilot Scale Column Experiments. These experiments were designed to investigate efficiency of granular activated carbon and metal doped titania nanoparticles in fixed bed columns. Column design was based on study by Tang et al. [19]. Pilot setup consisted of three glass columns each having internal diameter 1.5 cm and empty bed contact time was 10.5 min. Media depth for all columns was 12 cm. Column one is comprised of granular activated carbon having 0.56 mm mean particle size. Other two columns were filled by glass beads coated with Fe and Pt doped titania nanoparticles. Each column had glass wool at their base, as the supporting media. Flowrate through these columns was controlled using a peristaltic pump attached to the three-way manifold. 700 ng/L Geosmin and 2-MIB solutions were passed through these columns at 2 mL/min. Figure 1 shows schematic of the pilot column setup.

3.6.1. Glass Beads Etching and Coating. Nanoparticles coated glass beads were used in filter columns. Sterilized glass beads
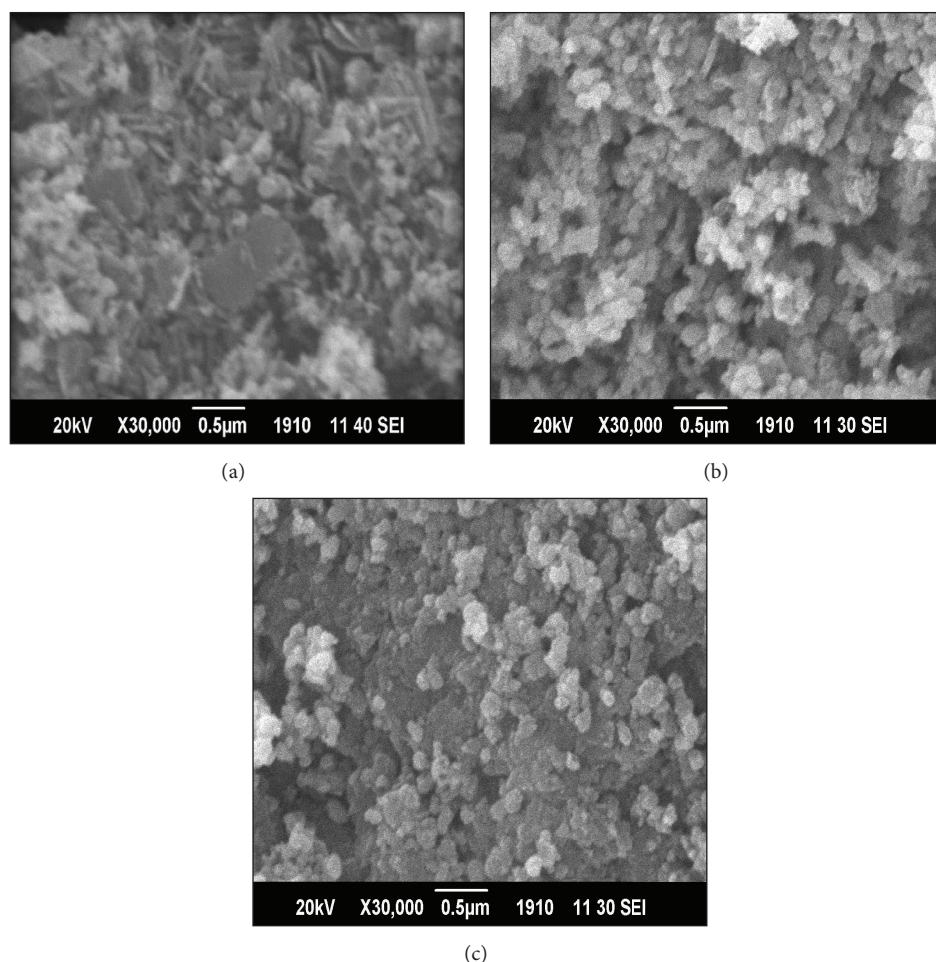
(a)

(b)

(c)

FIGURE 2: SEM micrograph of adsorbents at 30,000 resolution: (a) granular activated carbon and (b) Fe-TiO$_2$ (c) Pt-TiO$_2$ nanoparticles.

were dipped in 10% hydrogen fluoride solution and covered for 24 hours. Next, glass beads were stirred with metal doped titania nanoparticles aqueous solution, at 250 rpm for half an hour. After oven drying at 110°C for 20 min these coated beads were shifted to furnace at 400°C. Finally these were washed with distilled water, dried, and stored in dark.

3.6.2. Breakthrough Curves. Removal efficiency of the adsorption columns was represented by "break through curves" drawn from results, which showed that the concentration ratios (C/C_o) were a function of throughput volumes. Keeping in view the very low concentration of the pollutants, the breakthrough time and exhaustion time were set as C/C_o = 0.02 and C/C_o = 0.95, respectively. Samples for residual Geosmin and 2-MIB analysis were drawn after 10 bed volumes.

3.6.3. Column Desorption Study. In this study, after exhaustion of column, desorption study was carried out by pouring 50 mL of 0.1 M NaOH solution as an eluent, which was known to be efficient for column recovery [22]. Moreover, the adsorbent column was washed with distilled water before the next adsorption-desorption cycles. The adsorption-desorption

cycles were repeated trice using the optimized condition to check the sustainability of the column for repeated use.

3.7. Geosmin and 2-MIB Removal from Rawal Lake Filtration Plant Water. Adsorption capacity of the abovementioned adsorbents was tested to remove Geosmin and 2-MIB from natural water samples collected from Rawal filtration plant in batch and column experiments under optimized adsorption conditions.

4. Results and Discussion

4.1. Characterisation of Adsorbents. For the direct examination of particle size and surface morphology of the samples SEM was used. All the particles were spheroid or oblate spheroid loosed and macrospores can be clearly seen in the SEM micrographs. Scans of nanoparticles at ×30,000 resolution are represented in Figure 2. The crystalline sizes of the adsorbents were in the range of 24 to 51 nm (activated carbon (43.5 nm), Fe-TiO$_2$ (38.5 nm), and Pt-TiO$_2$ (41.6 nm)). SEM images of Fe-TiO$_2$ and Pt-TiO$_2$ nanoparticles confirmed the presence of more porous, sponge-like structure of high roughness and complexity, as compared to activated carbon,
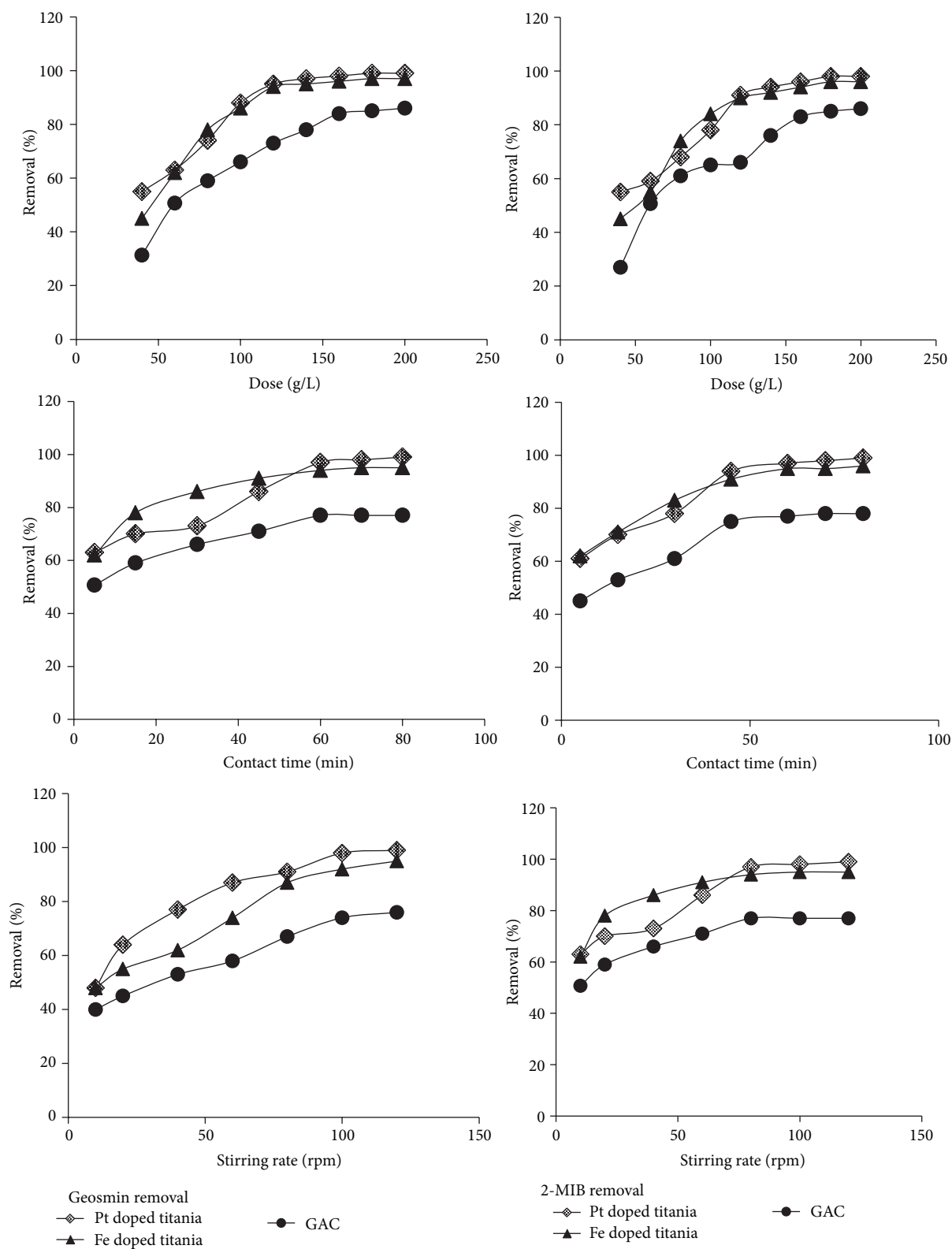
FIGURE 3: Dose, contact time, and stirring rate optimization for adsorbents.

TABLE 2: Removal efficiency of adsorbents used.

Adsorbents	GAC		Fe-TiO$_2$		Pt-TiO$_2$	
	Geosmin	2-MIB	Geosmin	2-MIB	Geosmin	2-MIB
% removal	82	76	96	94	99	98

TABLE 3: Freundlich constant parameters for Geosmin and 2-MIB analysis.

Adsorbate	Adsorbent	Freundlich isotherm parameters		
		k_f	n	R^2
2-MIB	GAC	0.64	3.12	0.97
	Fe-TiO$_2$	0.70	3.70	0.98
	Pt-TiO$_2$	0.71	4.00	0.99
Geosmin	GAC	0.65	3.10	0.97
	Fe-TiO$_2$	0.71	4.18	0.98
	Pt-TiO$_2$	0.86	4.38	0.99

TABLE 4: Langmuir constant parameters for Geosmin and 2-MIB analysis.

Adsorbate	Adsorbent	Langmuir isotherm parameters			
		V_m	K	R_L	R^2
2-MIB	GAC	0.62	0.80	0.71	0.98
	Fe-TiO$_2$	0.64	1.14	0.58	0.99
	Pt-TiO$_2$	0.70	1.56	0.56	0.99
Geosmin	GAC	0.64	0.90	0.69	0.98
	Fe-TiO$_2$	0.70	1.35	0.60	0.99
	Pt-TiO$_2$	0.72	1.53	0.57	0.99

Value of R_L interpretation: greater than 1 indicates unfavourable isotherm, equal to 1 means linear isotherm, between 0-1 shows favourable isotherm, and 0 indicates irreversible isotherm.

indicating the high surface area for adsorption. BET surface areas for three adsorbents tested were 567 m^2/g, 423 m^2/g, and 274 m^2/g for Pt-TiO$_2$, Fe-TiO$_2$, and activated carbon, respectively.

4.2. Adsorption Conditions Optimization. Adsorption condition optimization results are demonstrated in Figure 3. The batch adsorption experiments were carried out by using various amounts adsorbent types.

Similar removal trends were observed for both Geosmin and 2-MIB removal, with increasing adsorbent doses. It was observed that, even on increasing the amount of adsorbent doses in the solution, the percentage removal of Geosmin and 2-MIB increased gradually and % removal plateaued at 125 mg/L for metal doped nanoparticles while 160 mg/L was found to be optimized GAC dosage. Adsorption capacities of the three adsorbent types at different contact times, when all other variables are constant, were determined. The maximum adsorption capacity of Geosmin and 2-MIB was obtained within contact time of 60 min, with optimized adsorbents dosage for all adsorbents studied. After optimizing PAC dosage and contact time final experiments were performed to

explore optimum mixing rate. Results illustrate that stirring rate had remarkable effects on rate of adsorption as with the increase in speed contact between adsorbent and adsorbate increases. Maximum adsorption of Geosmin and 2-MIB was observed at mixing rate of 100 rpm using optimized adsorbent dozes, within a contact time of 60 min.

4.3. Removal Efficiency of Adsorbents. Removal efficiencies of the selected adsorbents are given in Table 2. Results indicate that removal efficiencies of metal doped titania particles were much higher, as compared to Granular activated carbon. Overall, Pt doped titania nanoparticles showed the best removal efficiency towards Geosmin and 2-MIB.

4.4. Adsorption Isotherms. Removal efficiencies of adsorbents were tested through isotherm studies. The linear form of the isotherm studies helped in better understanding of the adsorption phenomena. Freundlich and Langmuir equation explained adsorption of Geosmin and 2-MIB on different adsorbent concentrations, as discussed in the next sections.

Freundlich equation was used in this study as given below [23]

$$\text{Log } q_e = \log K + \frac{1}{n} \log C_e, \tag{2}$$

where q_e = equilibrium loading of Geosmin and 2-MIB on the GAC (ng/mg), C_e = equilibrium concentration of Geosmin and 2-MIB in the water (ng/L), k_f = adsorption capacity at unit concentration (ng/mg), $1/n$ = heterogeneity of adsorbent, and $1/n$ and k_f were obtained from slope and intercept of linear plot between log q_e and log C_e.

From data stated in Table 3, it is clear that the Freundlich model is statistically valid for all adsorbents analyzed. To compare different adsorbents, usually the absorbent with the higher amount of adsorbate adsorbed, at the desired effluent concentration, is preferred for the particular application. A number of carbon physical and chemical properties affect adsorption toward a particular adsorbate. For Geosmin and 2-MIB, the hydrophobic compounds, the amount of surface area associated with the adsorbate is critically important. The Freundlich constants (n and k) given in Table 3 for each adsorbent and the resulting curves are shown in Figure 4. The values of Freundlich constant K_{ef} indicate that this model gives a good fit to both Geosmin and 2-MIB. Values of constants were highest for Pt doped titania nanoparticles showing great affinity of the binding sites of adsorbent towards both adsorbates with the values 0.86 and 0.71 for Geosmin and 2-MIB, respectively. In contrast, the K_f values for GAC for removal of adsorbates are lowest, showing lowest adsorption ability of GAC among all adsorbents compared.
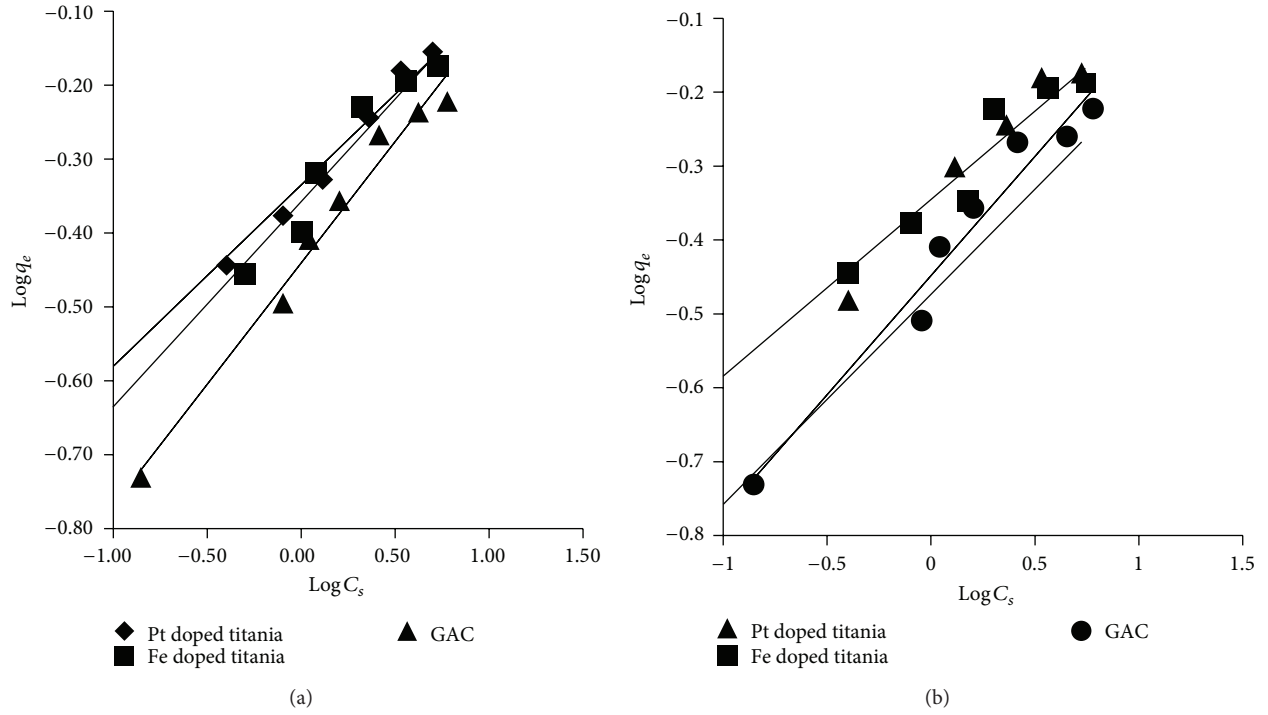
FIGURE 4: (a) Freundlich isotherms curve for adsorption of Geosmin at $18 \pm 2°$C. (b) Freundlich isotherms curve for adsorption of 2-MIB at $18 \pm 2°$C.
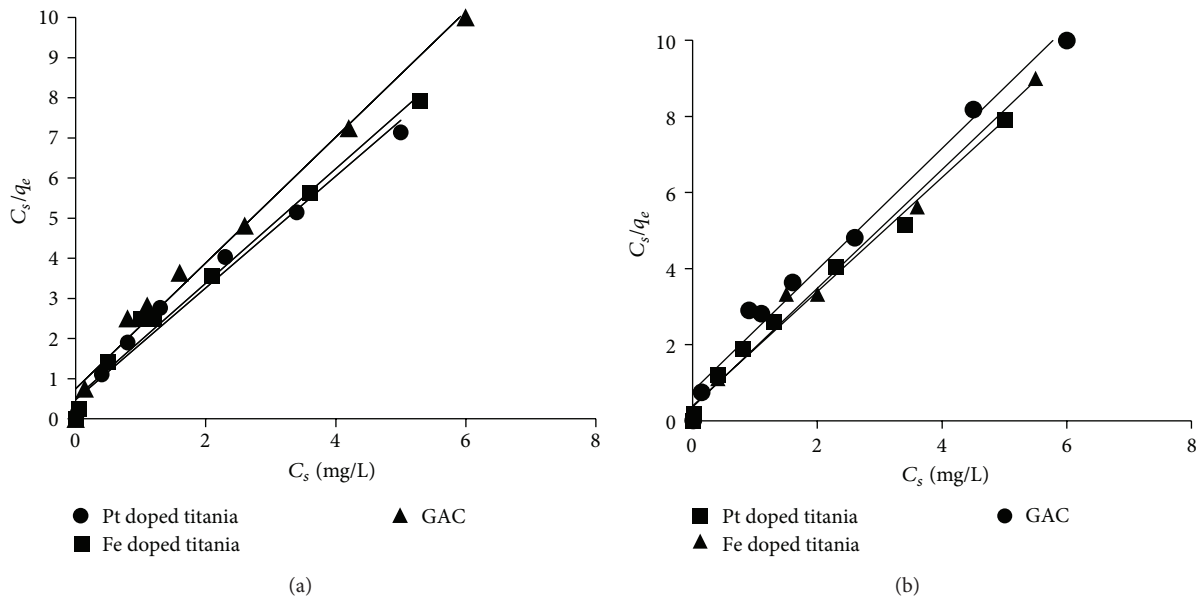
FIGURE 5: (a) Langmuir isotherm curve for adsorption of Geosmin at $18 \pm 2°$C. (b) Langmuir isotherm curve for adsorption of 2-MIB at $18 \pm 2°$C.

Mathematical form of Langmuir isotherm is given below [24]

$$\frac{C_e}{q_e} = \frac{C_e}{V_m} + \frac{1}{KV_m}, \tag{3}$$

where q_e = equilibrium loading of Geosmin and 2-MIB on the GAC (ng/mg), C_e = equilibrium concentration in the water (ng/L), and V_m = maximum adsorption capacity (ng/mg). Values of K and V_m were obtained directly from intercept and slope of linear plot between C_s/q_e and C_s. Langmuir constants are described in Table 4.

Langmuir isotherms curves for Geosmin and 2-MIB are shown in Figure 5. Values for adsorption coefficient K and monolayer capacity V_m are higher for Pt doped

TABLE 5: Pseudo-second order parameters for Geosmin for and 2-MIB analysis.

| Adsorbate | Adsorbent | Pseudo-second-order equation parameters | | | |
		q_e (mg/g)	k (g/mg min)	h (mg/g min)	R^2
2-MIB	GAC	0.39	0.98	0.12	0.99
	Fe-TiO$_2$	0.58	1.02	0.24	0.99
	Pt-TiO$_2$	0.61	1.10	0.35	0.99
Geosmin	GAC	0.43	0.14	0.15	0.99
	Fe-TiO$_2$	0.62	0.09	0.23	0.98
	Pt-TiO$_2$	0.67	1.04	0.37	0.99

(a)

(b)
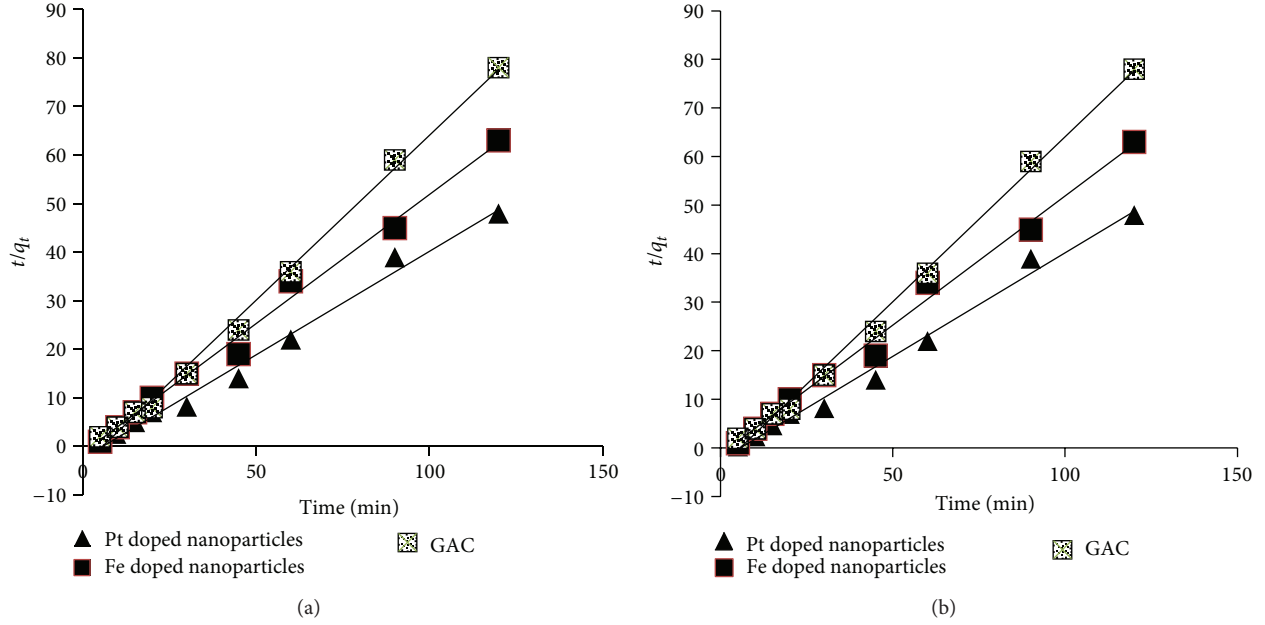
FIGURE 6: (a) Pseudo-second-order kinetic models for 2-MIB at $18 \pm 2°$C. (b) Pseudo-second-order kinetics model for Geosmin at $18 \pm 2°$C.

TABLE 6: Water quality parameters of RLFP treated water.

Quality parameter	Range	Units
DOC	3.3–5.4	mg/L
Turbidity	0.1-0.2	NTU
pH	6.5–7	—
Conductivity	500–700	S/cm
NOM	3.35–5.5	mg/L
UV$_{254}$	0.05–0.90	cm^{-1}
Geosmin	690	ng/L
2-MIB	657	ng/L

titania nanoparticles. These results explicitly indicate more favourable adsorption of Geosmin and 2-MIB on metal doped titania nanoparticles as compared to GAC.

The shape of the isotherm can be used to examine the favourability of the adsorbent. It was done by another dimensionless quantity, R_L, given by the following equation:

$$R_L = \frac{1}{1 + (KC_0)}, \tag{4}$$

where R_L is the dimensionless separation factor, C_o is the initial Geosmin and 2-MIB concentrations, and K is the Langmuir constant. R_L values ranged between 0.69 and 0.57 for Geosmin and 0.71–0.56 for 2-MIB. It showed favourable isotherms for both off-flavours. Values for both isotherm constants are higher in case of Geosmin which clearly suggest preferred adsorption of Geosmin on all adsorbents, compared to 2-MIB. Cook at al., 2004, also reported that Geosmin showed better adsorption than 2-MIB on activated carbon and this was attributed to the lower molecular weight and higher solubility of Geosmin [25].

4.5. Kinetic Isotherms . A pseudo-second-order model (5) was used to describe the kinetics of adsorption [26]:

$$\frac{dq_t}{dt} = k (q_e - q_t)^2, \tag{5}$$

where q_t is the adsorption capacity (mg/g) at any time interval, q_e is the adsorption capacity (mg/g) at the equilibrium, and k (g mg^{-1} min^{-1}) is the pseudo-second-order rate constant.
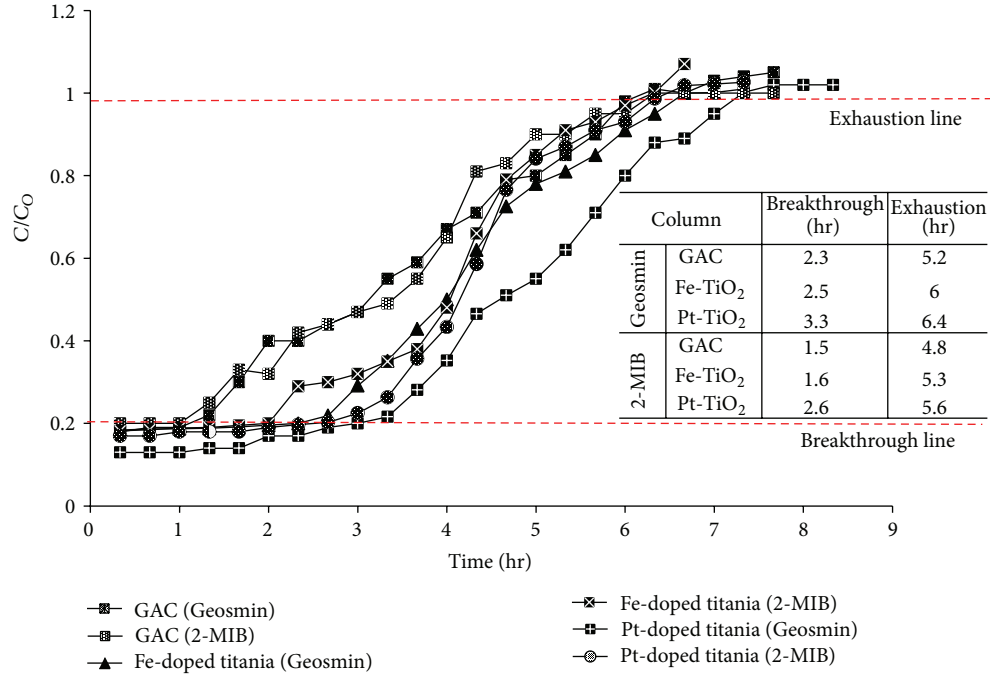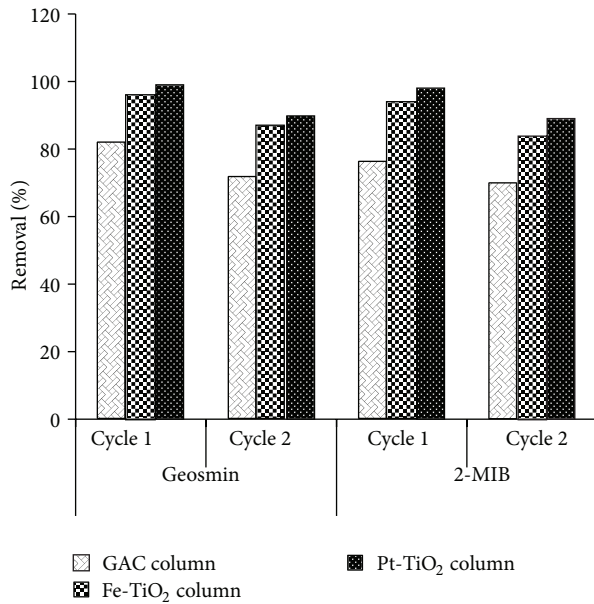
Column		Breakthrough (hr)	Exhaustion (hr)
Geosmin	GAC	2.3	5.2
	Fe-TiO$_2$	2.5	6
	Pt-TiO$_2$	3.3	6.4
2-MIB	GAC	1.5	4.8
	Fe-TiO$_2$	1.6	5.3
	Pt-TiO$_2$	2.6	5.6

- □ GAC (Geosmin)
- □ GAC (2-MIB)
- ▲ Fe-doped titania (Geosmin)
- ⊠ Fe-doped titania (2-MIB)
- ▦ Pt-doped titania (Geosmin)
- ⊙ Pt-doped titania (2-MIB)

FIGURE 7: Breakthrough curves for Geosmin and 2-MIB at 18 ± 2°C.

- ▨ GAC column
- ▨ Fe-TiO$_2$ column
- ▦ Pt-TiO$_2$ column

FIGURE 8: Adsorption capacities for columns after regeneration.

Integrating (5) with the following boundary conditions: $t = 0$ to t and $q_t = 0$ to q_t, gives

$$\frac{1}{q_e - q_t} = \frac{1}{q_e} + kt. \tag{6}$$

Equation (6) can be linearized as follows:

$$\frac{t}{q_t} = \frac{1}{kq_e^2} + \frac{1}{q_e}t. \tag{7}$$

Thus, the parameters k and q_e can be obtained from the intercept and slope of the plot of (t/q_t) against t.

The kinetic data obtained from batch adsorption tests was analyzed by using the pseudo-second-order model. Figure 6 shows the linearized plots of the results. The kinetics of Geosmin and 2-MIB adsorption were studied in batch adsorption tests, with three different adsorbents. Results clearly indicate that the removal efficiency is a function of contact time; moreover, maximal q_e and k values were obtained with Pt doped nanoparticles. All pseudo-second-order parameters are listed in Table 5. The data demonstrate a good compliance with the pseudo-second-order equation, as the regression coefficients for the linear plots were higher than 0.98 for all the adsorbents tested.

4.6. Column Experiments Results. Column efficiencies were determined in terms of breakthrough and column exhaustion times. At the beginning, removal through columns was very efficient as the adsorbents were fresh with all of their adsorption sites available. With the passage of time, some of the adsorption sites got exhausted and effluent concentrations started rising. After all the adsorption sites were exhausted, the inlet and the outlet concentrations became nearly the same. Column 1 having granular activated carbon was not found very effective either for Geosmin or 2-MIB. It attained early breakthrough and exhaustion points. Figure 7 illustrates breakthrough curves, breakthrough points, and exhaustion points for Geosmin and 2-MIB, respectively.

Overall comparison of adsorbents indicated that Pt-doped titania nanoparticles were most efficient for Geosmin and 2-MIB removal. Geosmin removal was a bit higher than 2-MIB in this case as well.
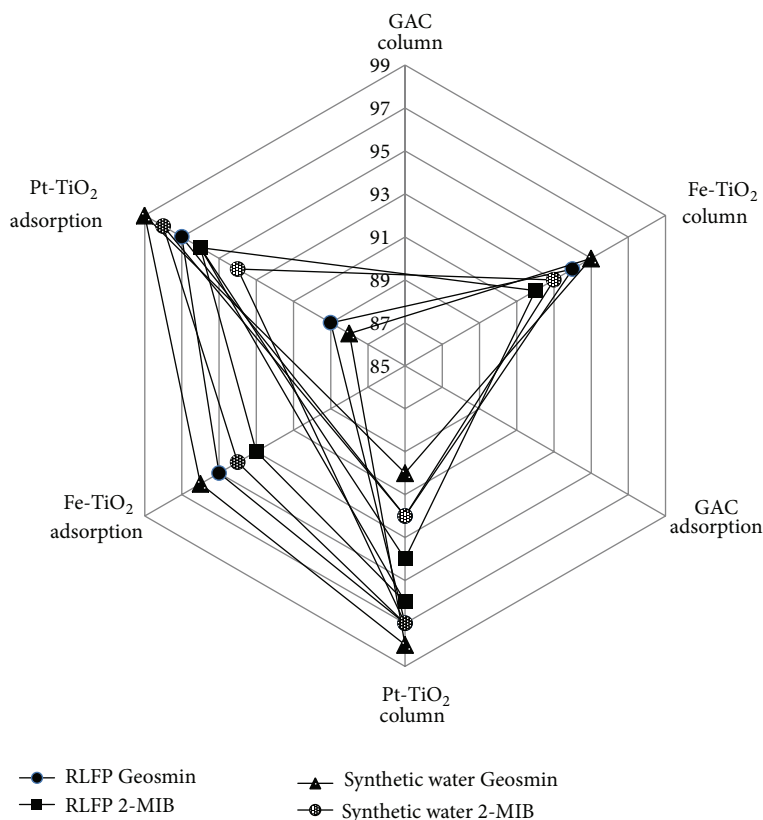
FIGURE 9: Comparison of Geosmin and 2-MIB removal from synthetic and RLFP water samples.

4.7. Column Desorption. For a viable sorption process, columns desorption and regeneration are important. The exhausted 12 cm bed volume columns (for all the three types of columns) were successfully regenerated using 0.1 M of NaOH solution. The results (Figure 8) show that, on average, the columns could be used again by losing only 8% of their adsorption ability in successive cycle.

4.8. Geosmin and 2-MIB Removal Using RLFP Treated Water. The above-stated experiments were performed using synthetic solution of Geosmin and 2-MIB. Finally, experiments were conducted with the RLFP treated water samples. Average concentration of Geosmin and 2-MIB in composite water samples was 690 ng/L and 678 ng/L, respectively. Water quality data for water from RLFP is given in Table 6.

A comparison of taste and odor removal efficiency using adsorption and Column tests is presented in Figure 9. According to the results better removal was achieved with synthetic water as compared to the sample of treated water from RLFP. This difference can be attributed to organic matter and several interfering species in the treated water samples (Table 6). High removal efficiencies of 97–99% for Geosmin and 96–98% for 2-MIB from both synthetic and treated water samples confirm effectiveness of metal doped nanoparticles.

5. Conclusions

The present experimental results suggest that metal doped titania nanoparticles demonstrate significant adsorption potential for the accelerated removal for earthy-musty odor producing compounds in the drinking water. Study shows that metal doping increases BET surface area, thus enhancing efficiency of titania to adsorb Geosmin and 2-MIB. The concentrations examined in this study are typically the levels that cause odor problems in lake water. Whilst activated carbon is still useful for off-flavours removal, metal doped titania nanoparticles are far more effective. Fe-TiO$_2$ showed 95% and 93% Geosmin and 2-MIB removal. Pt-TiO$_2$ was found to be most efficient; it removed 98% of Geosmin and 97% of 2-MIB as compared to 82% and 73% Geosmin and 2-MIB removal by most widely used granular activated carbon. Smaller size, extremely large surface area (567 m^2/g), and more active adsorption site make Pt-TiO$_2$ as superior adsorbent. Further work is also being undertaken to refine the process for implementation in commercial applications.

Conflict of Interests

The authors declare that there is no conflict of interests regarding the publication of this paper.

Acknowledgment

References

[1] M. Durrer, U. Zimmermann, and F. Jüttner, "Dissolved and particle-bound geosmin in a mesotrophic lake (Lake Zürich): spatial and seasonal distribution and the effect of grazers," *Water Research*, vol. 33, no. 17, pp. 3628–3636, 1999.

[2] A. Peter and U. Von Gunten, "Oxidation kinetics of selected taste and odor compounds during ozonation of drinking water," *Environmental Science and Technology*, vol. 41, no. 2, pp. 626–631, 2007.

[3] T.-F. Lin, J.-Y. Wong, and H.-P. Kao, "Correlation of musty odor and 2-MIB in two drinking water treatment plants in South Taiwan," *Science of the Total Environment*, vol. 289, no. 3, pp. 225–235, 2002.

[4] I. H. Suffet, G. A. Burlingame, P. E. Rosenfeld, and A. Bruchet, "The value of an odor-quality-wheel classification scheme for wastewater treatment plants," *Water Science and Technology*, vol. 50, no. 9, pp. 25–32, 2004.

[5] P. Westerhoff, M. Rodriguez-Hernandez, L. Baker, and M. Sommerfeld, "Seasonal occurrence and degradation of 2-methylisoborneol in water supply reservoirs," *Water Research*, vol. 39, no. 20, pp. 4899–4912, 2005.

[6] D. Sun, J. Yu, W. An, M. Yang, G. Chen, and S. Zhang, "Identification of causative compounds and microorganisms for musty odor occurrence in the Huangpu River, China," *Journal of Environmental Sciences*, vol. 25, no. 3, pp. 460–465, 2013.

[7] D. M. C. Rashash, A. M. Dietrich, and R. C. Hoehn, "Flavor profile analysis of selected odorous compounds," *The American Water Works Association*, vol. 89, no. 2, pp. 131–142, 1997.

[8] S. B. Watson, M. Charlton, Y. R. Rao et al., "Off flavours in large waterbodies: physics, chemistry and biology in synchrony," *Water Science and Technology*, vol. 55, no. 5, pp. 1–8, 2007.

[9] S.-W. Jung, K.-H. Baek, and M.-J. Yu, "Treatment of taste and odor material by oxidation adsorption," *Water Science and Technology*, vol. 49, no. 9, pp. 289–295, 2004.

[10] L. Ho, G. Newcombe, and J.-P. Croué, "Influence of the character of NOM on the ozonation of MIB and geosmin," *Water Research*, vol. 36, no. 3, pp. 511–518, 2002.

[11] S. L. N. Elhadi, P. M. Huck, and R. M. Slawson, "Removal of geosmin and 2-methylisoborneol by biological filtration," *Water Science and Technology*, vol. 49, no. 9, pp. 273–280, 2004.

[12] C. Ng, J. N. Losso, W. E. Marshall, and R. M. Rao, "Freundlich adsorption isotherms of agricultural by-product-based powdered activated carbons in a geosmin-water system," *Bioresource Technology*, vol. 85, no. 2, pp. 131–135, 2002.

[13] M. Pirbazari, V. Ravindran, B. N. Badriyha, S. Craig, and M. J. McGuire, "GAC adsorber design protocol for the removal of off-flavors," *Water Research*, vol. 27, no. 7, pp. 1153–1166, 1993.

[14] R. Srinivasan and G. A. Sorial, "Treatment of taste and odor causing compounds 2-methyl isoborneol and geosmin in drinking water: a critical review," *Journal of Environmental Sciences*, vol. 23, no. 1, pp. 1–13, 2011.

[15] T. Balaji and H. Matsunaga, "Adsorption characteristics of As(III) and As(V) with titanium dioxide loaded Amberlite XAD-7 resin," *Analytical Sciences*, vol. 18, no. 12, pp. 1345–1349, 2002.

[16] L. A. Lawton, P. K. J. Robertson, R. F. Robertson, and F. G. Bruce, "The destruction of 2-methylisoborneol and geosmin using titanium dioxide photocatalysis," *Applied Catalysis B: Environmental*, vol. 44, no. 1, pp. 9–13, 2003.

[17] M. A. Behnajady, N. Modirshahla, M. Shokri, and B. Vahid, "Effect of operational parameters on degradation of malachite green by ultrasonic irradiation," *Ultrasonics Sonochemistry*, vol. 15, no. 6, pp. 1009–1014, 2008.

[18] Y. Tang, Z. Jiang, Q. Tay et al., "Visible-light plasmonic photocatalyst anchored on titanate nanotubes: a novel nanohybrid with synergistic effects of adsorption and degradation," *RSC Advances*, vol. 2, no. 25, pp. 9406–9414, 2012.

[19] Y. Tang, Z. Jiang, J. Deng et al., "Synthesis of nanostructured silver/silver halides on titanate surfaces and their visible-light photocatalytic performance," *ACS Applied Materials and Interfaces*, vol. 4, no. 1, pp. 438–446, 2012.

[20] A. Bhatnagar, E. Kumar, and M. Sillanpää, "Nitrate removal from water by nano-alumina: characterization and sorption studies," *Chemical Engineering Journal*, vol. 163, no. 3, pp. 317–323, 2010.

[21] L. Ho, D. Hoefel, F. Bock, C. P. Saint, and G. Newcombe, "Biodegradation rates of 2-methylisoborneol (MIB) and geosmin through sand filters and in bioreactors," *Chemosphere*, vol. 66, no. 11, pp. 2210–2218, 2007.

[22] N. Saifuddin, C. Y. Nian, L. W. Zhan, and K. X. Ning, "Chitosan-silver nanoparticles composite as point-of-use drinking water filtration system for household to remove pesticides in water," *Asian Journal of Biochemistry*, vol. 6, no. 2, pp. 142–159, 2011.

[23] S. R. Chowdhury and E. K. Yanful, "Arsenic and chromium removal by mixed magnetite-maghemite nanoparticles and the effect of phosphate on removal," *Journal of Environmental Management*, vol. 91, no. 11, pp. 2238–2247, 2010.

[24] F. Deniz and S. Karaman, "Removal of an azo-metal complex textile dye from colored aqueous solutions using an agro-residue," *Microchemical Journal*, vol. 99, no. 2, pp. 296–302, 2011.

[25] D. Cook and G. Newcombe, "Can we predict the removal of MIB and geosmin with PAC by using water quality parameters?" *Water Science and Technology: Water Supply*, vol. 4, no. 4, pp. 221–226, 2004.

[26] W. T. Tsai, C. Y. Chang, C. H. Ing, and C. F. Chang, "Adsorption of acid dyes from aqueous solution on activated bleaching earth," *Journal of Colloid and Interface Science*, vol. 275, no. 1, pp. 72–78, 2004.

Research Article

Preparation of Oleyl Phosphate-Modified TiO$_2$/Poly(methyl methacrylate) Hybrid Thin Films for Investigation of Their Optical Properties

Masato Fujita,[1] Naokazu Idota,[2] Kimihiro Matsukawa,[3] and Yoshiyuki Sugahara[1,2]

[1]*Department of Applied Chemistry, School of Science and Engineering, Waseda University, 3-4-1 Okubo, Shinjuku-ku, Tokyo 169-8555, Japan*
[2]*Kagami Memorial Research Institute for Materials Science and Technology, Waseda University, 2-8-26 Nishiwaseda, Shinjuku-ku, Tokyo 169-0051, Japan*
[3]*Osaka Municipal Technical Research Institute, 1-10 Morinomiya, Joto-ku, Osaka 536-8553, Japan*

Correspondence should be addressed to Yoshiyuki Sugahara; ys6546@waseda.jp

TiO$_2$ nanoparticles (NPs) modified with oleyl phosphate were synthesized through stable Ti–O–P bonds and were utilized to prepare poly(methyl methacrylate)- (PMMA-) based hybrid thin films via the *ex situ* route for investigation of their optical properties. After surface modification of TiO$_2$ NPs with oleyl phosphate, IR and ^{13}C CP/MAS NMR spectroscopy showed the presence of oleyl groups. The solid-state ^{31}P MAS NMR spectrum of the product revealed that the signal due to oleyl phosphate (OP) shifted upon reaction, indicating formation of covalent Ti–O–P bonds. The modified TiO$_2$ NPs could be homogeneously dispersed in toluene, and the median size was 16.1 nm, which is likely to be sufficient to suppress Rayleigh scattering effectively. The TEM images of TiO$_2$/PMMA hybrid thin films also showed a homogeneous dispersion of TiO$_2$ NPs, and they exhibited excellent optical transparency even though the TiO$_2$ content was 20 vol%. The refractive indices of the OP-modified TiO$_2$/PMMA hybrid thin films changed higher with increases in TiO$_2$ volume fraction, and the hybrid thin film with 20 vol% of TiO$_2$ showed the highest refractive index (n = 1.86).

1. Introduction

Transparent materials with high refractive indices have been extensively required for numerous applications, including optical devices, lenses, antireflective coatings, and waveguides [1–3]. In these applications, synthetic polymers have been employed as optical materials exhibiting excellent formability and tunable chemical and physical properties. However, refractive indices of common polymers are limited to the range from 1.3 to 1.7 [4]. Recently, functional polymer-based hybrids incorporating inorganic fillers with high refractive indices have attracted increasing attention for their ability to improve the optical properties of conventional polymers [5]. TiO$_2$ is an attractive inorganic component for preparation of hybrid materials because of such characteristics as its high refractive index (n = 2.5–2.7), nonadsorption

of visible light, nontoxicity, and low cost [6]. One important issue in the preparation of transparent TiO$_2$/polymer hybrids is the suppression of Rayleigh scattering at the interfaces between inorganic components and polymer matrices. In general, the diameters of inorganic fillers should be smaller than 40 nm, which is one-tenth the minimum wavelength of visible light, to suppress Rayleigh scattering [7]. Thus, TiO$_2$ nanoparticles (NPs) of desirable size, below 40 nm, as high refractive inorganic fillers, should be employed in the preparation of transparent polymer-based hybrids. In addition, homogeneous dispersion of TiO$_2$ NPs in a polymer matrix is also required to maintain the transparency after formation of the hybrids. TiO$_2$ NPs easily aggregate in hydrophobic polymer matrices because their surfaces are covered with hydrophilic hydroxyl groups [8]. Surface modification of TiO$_2$ NPs with organic groups is consequently an important

technique for improving their affinity with polymer matrices [7] to suppress their aggregation.

Carboxylic acids [9, 10], silane coupling reagents [11, 12], and phosphorus coupling reagents [13, 14] have been generally used for surface modification of various metallic oxides including TiO_2 because of their high reactivity to the surfaces. In the case of inorganic fillers in polymer-based hybrids for optical applications, monolayered stable surface modification is strongly desired to maintain their uniform and stable dispersion in the polymer matrix. For modification with carboxylic acids, the drawback is instability of Ti–O–C bonds with respect to hydrolysis. It is well-known that silane coupling reagents undergo inter- and intramolecular condensation (namely, homocondensation) in the presence of a trace of water to form multilayers comprising silane coupling molecule moieties on their surfaces. Phosphorus coupling reagents react with the TiO_2 surfaces easily to form Ti–O–P bonds, on the other hand, which are stable with respect to hydrolysis, and no homocondensation of phosphorous coupling reagents proceeds under mild conditions [15]. Among phosphorus coupling reagents, phosphoric acid esters are attractive, since they can be easily prepared from commercially available phosphoric acids and alcohols [16]. Another advantage is the flexibility of their structures, leading to facile introduction of desirable functional groups, which play an important role in their compatibility with both polymer matrices and solvents [17–21].

Poly(methyl methacrylate) (PMMA) is a typical optical polymer exhibiting high transparency and excellent formability. Since the refractive index of PMMA is relatively low for optical applications ($n = 1.49$) [22], incorporation of TiO_2 NPs in PMMA matrices has been investigated extensively for preparation of PMMA-based hybrid materials exhibiting high refractive indices [10, 23–34]. Yuwono et al. prepared transparent TiO_2/PMMA hybrid films via an *in situ* sol-gel route [24]. The refractive index of the hybrid film increased to 1.780 with incorporation of 60 mass% TiO_2 into PMMA. Lee and Chen also investigated the *in situ* sol-gel route for preparation of hybrids using titanium(IV) *n*-butoxide and PMMA-based polymers bearing trimethoxysilyl residues [25]. The refractive indices of the hybrid films increased linearly from 1.508 to 1.867 with TiO_2 contents in the range from 2.9 to 70.7 mass% TiO_2. In both studies, the *in situ* sol-gel route was used to generate anatase TiO_2 NPs ($n = 2.5$) in the polymer matrices. In the *in situ* method, it is difficult to control the precise amount of TiO_2 content and the dispersion of NPs in PMMA. An *ex situ* route in which inorganic fillers are incorporated into polymer matrices after surface modification, on the other hand, enables easier adjustment of the refractive indices of TiO_2/PMMA hybrids than the *in situ* route. Thus, the *ex situ* route enables us to achieve excellent dispersion of well-defined rutile TiO_2 NPs ($n = 2.7$) into polymer matrices.

In this study, we report the preparation of PMMA-based hybrid thin films by incorporating TiO_2 NPs modified with oleyl phosphate (OP) via the *ex situ* route. It has been demonstrating that an oleyl group is an attractive group for surface modification of TiO_2 NPs, though stability is not sufficient for modifications with oleic acid and oleylamine

[35] with respect to hydrolysis. The surfaces of the TiO_2 NPs were modified with OP, and a stable dispersion of the resulting modified TiO_2 NPs in organic solvent was achieved [36]. It should be noted that stability of resulting Ti–O–P bonds is important when TiO_2 NPs are used as nanofillers via the *ex situ* route. In this study, an aqueous dispersion of rutile TiO_2 was used as a starting material and was reacted with OP to achieve surface modification. The resultant OP-modified TiO_2 NPs were dispersed in a PMMA matrix to prepare TiO_2/PMMA hybrid thin films, and their optical properties were investigated as a function of the TiO_2 content.

2. Materials and Methods

2.1. Materials. A 15 mass% aqueous TiO_2 dispersion and OP (monoester and diester mixture) were kindly supplied by Sakai Chemical Co., Ltd. (Osaka, Japan). All reagents were used as received without further purification. Poly(methyl methacrylate) (PMMA) was purchased from Tokyo Chemical Industry Co., Ltd. (Tokyo, Japan).

2.2. Analyses. Infrared (IR) spectra were recorded on a JASCO FT-IR-460 Plus spectrometer using the KBr disk technique. X-ray diffraction (XRD) patterns were obtained with a Rigaku RINT-2500 diffractometer (monochromated CuKα radiation). Solid-state ^{13}C and ^{31}P nuclear magnetic resonance (NMR) spectroscopy was performed using a JEOL CMX-400 spectrometer at 99.55 and 160.25 MHz, respectively. Solid-state ^{13}C NMR spectra were obtained with cross-polarization (CP) and magic angle spinning (MAS) techniques (pulse delay 5 s, contact time 1.5 s, spinning rate 8 kHz). Solid-state ^{31}P NMR spectra were obtained with a MAS technique only (pulse delay 20 s, spinning rate 8 kHz). Thermogravimetric analysis (TG) was performed with a PERKIN ELMER TGA7 thermobalance in the temperature range from 30 to 800°C at a heating rate of 10°C/min under an air flow. A transmission electron microscopy (TEM) image was obtained with a JEOL JEM-1011 microscope operating at 100 kV accelerating voltage. The distribution of particle sizes was measured by dynamic light scattering (DLS) technique using a NIKKISO Nanotrac Wave-EX150 at a wavelength of 780 nm. In obtaining TEM image of TiO_2/PMMA hybrids, the sample was prepared on a Si wafer and an ultrathin section of the film was cut by a focused ion beam instrument (SEIKO EG&G SMI 2050). Ultraviolet-visible (UV-Vis) spectra were recorded on a JASCO V-630 spectrometer in the transmittance mode. The refractive indices were determined using an Otsuka Electronics FE-3000 refractive film thickness monitor. The resultant refractive indices of hybrid films were reported as a function of volume fraction of TiO_2 (=[volume of TiO_2 NPs]/[volume of PMMA]) using density of rutile TiO_2 (4.23 g/cm^3) [37] and PMMA (1.18 g/cm^3) [38].

2.3. Surface Modification of TiO_2 NPs. OP moiety was covalently bound to the surface of TiO_2 NPs using an aqueous dispersion diluted with 15 mL of methanol, based on a previous study [36]. Briefly, 0.49 mL of OP dissolved in 20 mL of methanol was added to the TiO_2 dispersion and stirred

for 18 h at room temperature. The precipitate was separated by centrifugation at 3500 rpm for 10 min and redispersed in 5 mL of toluene. The precipitate was washed twice with 15 mL of ethanol by the dispersion-precipitation process using super-centrifugation at 13500 rpm for 5 min to remove unreacted OP. The precipitate was then dispersed in 10 mL of toluene, following evaporation of the solution in vacuo. Finally, the remaining OP-modified TiO_2 NPs (OP_TiO_2) were redispersed in 20 mL of toluene.

2.4. Preparation of TiO_2/PMMA Hybrid Thin Films. Prescribed amounts of the OP_TiO_2/toluene dispersion and toluene were added to a vial containing 200 mg of PMMA. In all the PMMA-based hybrid samples (0–20 vol% TiO_2 content), the total dispersion volume was 10 mL. After stirring for 5 h at 40°C, a dispersion of OP_TiO_2 and PMMA was obtained. Hybrid thin films were prepared by spin-coating of the dispersion on glass substrates at 2000 rpm for 20 s and subsequent heating at 100°C for 1 h.

3. Results and Discussion

3.1. Characterization of TiO_2 NPs. The FTIR spectra of OP_TiO_2, OP, and bare TiO_2 NPs are shown in Figure 1. In the spectrum of OP_TiO_2, absorption bands assignable to oleyl groups are present: stretching vibrations of –HC=CH– appear at $3001\,cm^{-1}$, $\nu_{as}(CH_3)$ at $2954\,cm^{-1}$, $\nu_s(CH_3)$ at $2871\,cm^{-1}$, $\nu_{as}(CH_2)$ at $2921\,cm^{-1}$, $\nu_s(CH_2)$ at $2851\,cm^{-1}$, and $\delta(CH_2)$ at $1458\,cm^{-1}$. These bands are also present in the spectrum of OP [39]. Notable differences among these IR spectra are observed in the P–O stretching region. Although a ν(P=O) absorption band at $1151\,cm^{-1}$ is clearly observed in the spectrum of OP, the corresponding band disappears in the spectrum of OP_TiO_2. P–O stretching absorption bands, which are not observed in the spectrum of TiO_2 NPs, are present at 1029 and $1008\,cm^{-1}$ in the spectrum of OP_TiO_2. These observations suggest that the OP moiety is bound to the TiO_2 surface [13].

The solid-state ^{13}C CP/MAS NMR spectrum of OP_TiO_2 is shown in Figure 2. The carbon signals of free OP in the liquid-state ^{13}C NMR spectrum (Figure 2(a)) are observed at 129.9, 67.9, 32.6, 31.9, 29.3, 27.2, 27.2, 25.4, 22.7, and 14.1 ppm. In the spectrum of OP_TiO_2, therefore all the signals at 130, 68, 33, 31, 28, 27, 24, and 15 ppm are assignable to the oleyl groups. Thus, the solid-state ^{13}C CP/MAS NMR and FTIR results demonstrate the presence of oleyl groups in the OP_TiO_2.

The solid-state ^{31}P MAS NMR spectrum of OP_TiO_2 is shown in Figure 3. In the liquid-state ^{31}P NMR spectrum of free OP (Figure 3(a)), the signals of free mono- and diesters are observed at 4.3 and 3.1 ppm, respectively. In the OP_TiO_2, the signals are observed at 4.5, 2.1, and −1.3 ppm after the modification reaction. Guerrero et al. reported that the NMR signal of organophosphorous compounds shifted upfield after dehydration condensation between Ti–OH and P–OH [13]. In addition, the phosphorous signals shifted downfield with the coordination of the phosphoryl oxygen with Lewis acid sites because of an increase in the electrophilicity of phosphorous atoms. The disappearance of the ν(P=O) absorption

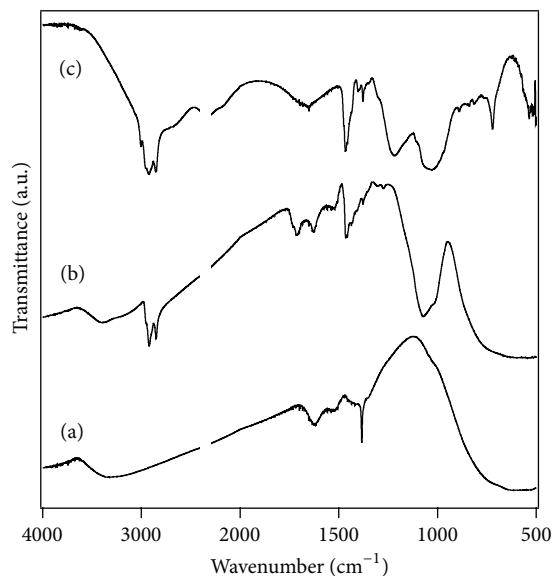Figure 1: FTIR spectra of (a) TiO_2 NPs, (b) OP_TiO_2, and (c) OP.
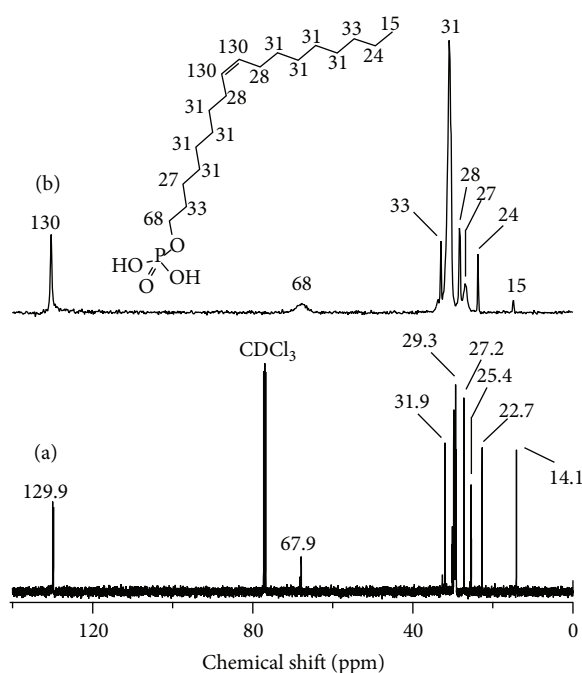

Figure 2: (a) ^{13}C NMR spectrum of OP and (b) ^{13}C CP/MAS NMR spectrum of OP_TiO_2.

band from FTIR suggests that the phosphoryl oxygen in OP may react preferentially with the Lewis acid sites of the TiO_2 surfaces. Thus, the signal at −1.3 ppm is assignable to the tri- and bidentate environments of mono- and dioleyl phosphate moieties, respectively. The signal at 2.1 ppm is likely to be due to the bidentate environment of a monooleyl phosphate moiety produced by a reaction involving P=O and Lewis acid sites. The formation of monodentate binding by a reaction between Lewis acid sites on TiO_2 NPs and
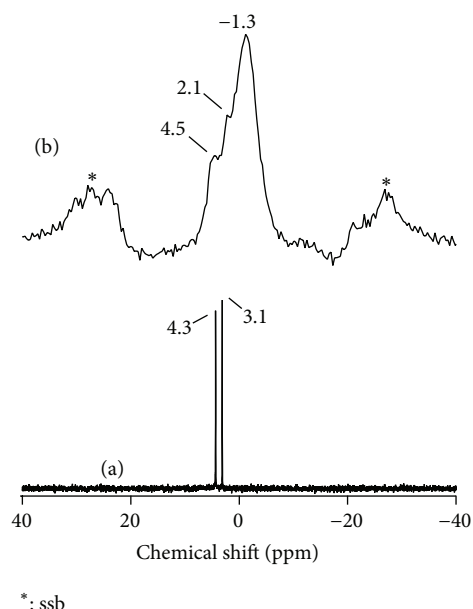
FIGURE 3: (a) ^{31}P NMR spectrum of OP and (b) ^{31}P MAS NMR spectrum of OP_TiO$_2$.

FIGURE 4: UV-Vis spectra of OP_TiO$_2$/PMMA hybrid films.

phosphoryl oxygens of OP seems to result in the appearance of the signal at 4.5 ppm.

In XRD patterns of TiO$_2$ NPs and OP_TiO$_2$ (see Figure S1 in Supplementary Material available online at http://dx.doi .org/10.1155/2015/297197), all diffraction lines in the patterns of both samples correspond to rutile TiO$_2$ (JCPDS card 21-1276), indicating that the crystal structure is retained after the reaction. The crystallite size of the TiO$_2$ NPs is estimated at 5.5 nm using the Scherrer equation.

In the TEM image of OP_TiO$_2$ (Figure S2), TiO$_2$ NPs can be observed as a large number of dark spots in the range of 4–20 nm. Almost all of the TiO$_2$ NPs are individually divided by border lines with a few nm thickness, and they appear to correspond to OP layers on the surface. Considering the length of the oleyl groups (=2.3 nm) [40], OP moieties could be present as monolayers on the surfaces of the TiO$_2$ NPs. The particle size distribution is determined by DLS using dispersion of OP_TiO$_2$ in toluene (Figure S3 in Supplementary Material). The size distribution of the OP_TiO$_2$ NPs is shown to be relatively narrow with the monodispersion, and the median size is 16.1 nm. In contrast, bare TiO$_2$ NPs exhibit a 4.9 nm median size for the starting aqueous dispersion. Since individual particle shapes of OP_TiO$_2$ are clearly observed in the TEM images, aggregation comprising a limited number of TiO$_2$ NPs could be modified with OP. Thus, it is demonstrated that OP-modified TiO$_2$ NPs are successfully prepared as nanofillers for optical applications because their size can be controlled at below 40 nm to suppress Rayleigh scattering effectively.

3.2. Optical Properties of OP_TiO$_2$/PMMA Hybrid Thin Films.
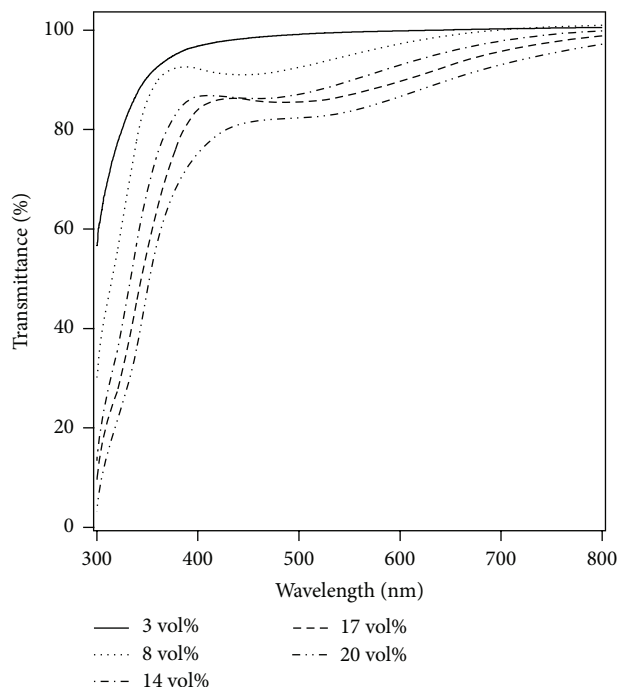OP_TiO$_2$/PMMA hybrid thin films are transparent even though they contain 20 vol% TiO$_2$ NPs (Figure S4 in
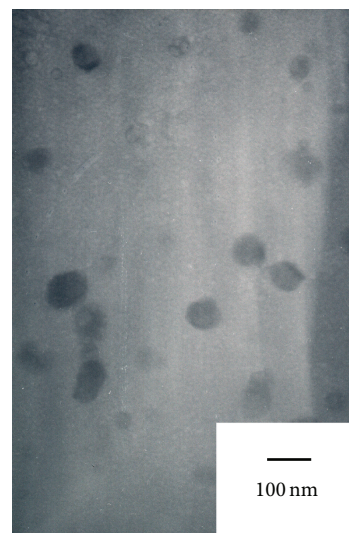

FIGURE 5: TEM image of OP_TiO$_2$/PMMA hybrid film (14 vol% TiO$_2$).

Supplementary Material). UV-Vis spectra of OP_TiO$_2$/ PMMA hybrid thin films containing 3, 8, 14, and 20 vol% TiO$_2$ are shown in Figure 4. It is clearly demonstrated that the transmittance value at 633 nm is higher than 89.0% for all OP_TiO$_2$/PMMA hybrid thin films. In the TEM image of OP_TiO$_2$/PMMA containing 14 vol% TiO$_2$ shown in Figure 5, dark circles with diameters of 10–40 nm are homogeneously dispersed in the PMMA matrices. Although some aggregated TiO$_2$ NPs larger than 40 nm are observed in the TEM image, the dispersion of TiO$_2$ NPs of a desirable size
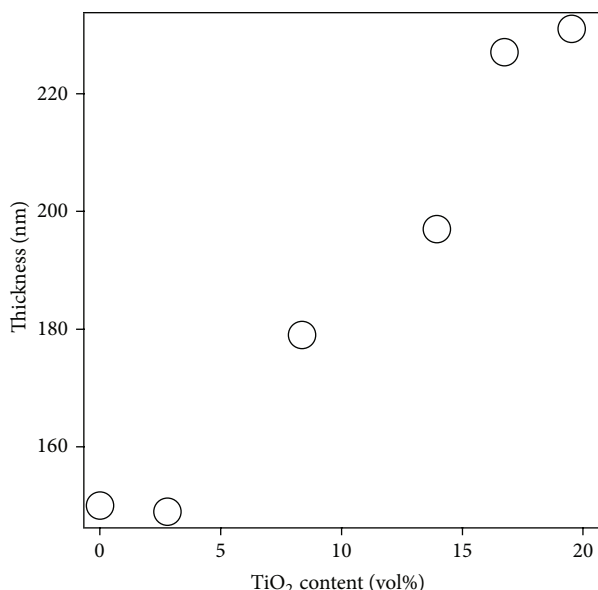
FIGURE 6: Changes in thicknesses of TiO$_2$/PMMA hybrid films as a function of their TiO$_2$ content.
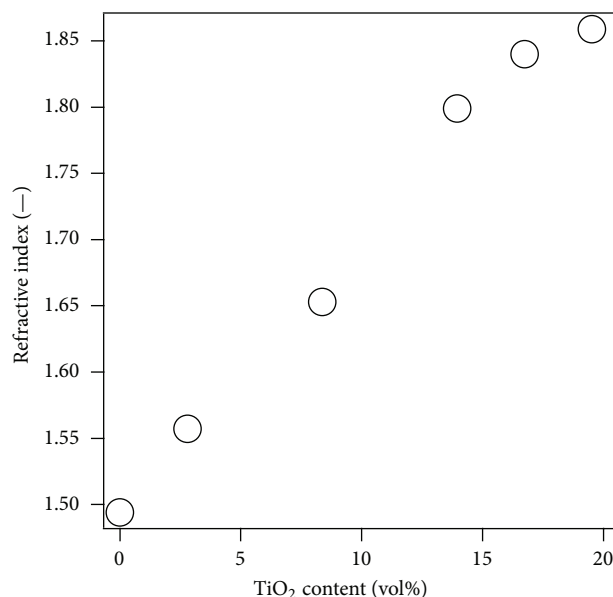

FIGURE 7: Changes in refractive indices of TiO$_2$/PMMA hybrid films as a function of TiO$_2$ content.

for suppression of Rayleigh scattering therefore leads to high transparency of the OP_TiO$_2$/PMMA hybrid thin films.

The thicknesses of the OP_TiO$_2$/PMMA hybrid thin films are shown in Figure 6. The film thickness increases in the range of 150–260 nm with increases in TiO$_2$ volume fraction. In general, the thickness of spin-coated polymer film depends mainly on the viscosity and density of a polymer solution at a certain spin speed [41]. TiO$_2$ NPs have a greater density than PMMA, and PMMA is diluted with a low viscosity OP_TiO$_2$ dispersion. The effect of density seems to dominate and the addition of the OP_TiO$_2$ dispersion to the PMMA solution results in the formation of a thicker film than neat PMMA.

The refractive indices of the OP_TiO$_2$/PMMA hybrid thin films at 633 nm are plotted against the TiO$_2$ volume fraction, as shown in Figure 7. The refractive index of the neat PMMA film is 1.49, and the indices of OP_TiO$_2$/PMMA hybrid thin films increase linearly with increases in the TiO$_2$ volume fraction, suggesting that the refractive indices of hybrid thin films can be controlled by adjusting the TiO$_2$ volume fraction. At 20 vol% TiO$_2$ content, the refractive index rises to 1.86. This value is comparable with those of flint glass (n = 1.4–2.0) [42] and sapphire crystal (n = 1.77) [43], suggesting the potential usefulness of the OP_TiO$_2$/PMMA hybrids in the present study for various optical applications.

In a previous report on TiO$_2$/PMMA hybrids, Lee and Chen reported the preparation of anatase TiO$_2$/PMMA hybrid films using titanium butoxide and a PMMA derivative bearing trialkoxysilane in the side chains via the *in situ* sol-gel route [25]. The refractive indices of the hybrid films increased linearly between 1.508 and 1.867 for 2.9–70.7 mass% TiO$_2$ content. In the present study, rutile TiO$_2$ NPs, which have a higher refractive index than that of anatase, were dispersed in PMMA via the *ex situ* route. The refractive indices of the hybrid thin films in the present study are slightly higher

than those in the previous report using anatase in the TiO$_2$ content range between 0.9 and 21.6 vol%. In this study, OP used as a surface modifier has a relatively low refractive index (n = 1.45–1.48), and surface modification with OP should decrease the volume fraction of TiO$_2$ NPs compared with the hybrid film comprising only PMMA and TiO$_2$ in the previous report. Thus, the refractive indices of hybrid thin films using OP_TiO$_2$ were similar to those in the previous report in spite of the dispersion of rutile TiO$_2$ NPs.

4. Conclusions

OP was covalently bound to the surfaces of TiO$_2$ NPs to prepare TiO$_2$/PMMA hybrid thin films with high refractive indices. After the surface modification of TiO$_2$ NPs, IR and the solid-state ^{31}P MAS NMR results revealed the formation of Ti–O–P bonds, and the oleyl groups on the surfaces played an important role in suppressing the aggregation of TiO$_2$ NPs in toluene. The particle sizes of the OP-modified NPs were smaller than 40 nm and were homogeneously dispersed in PMMA. The OP_TiO$_2$/PMMA hybrid thin films exhibited excellent optical transparency, and their transmittance values were larger than 89.0% at 633 nm. The refractive indices of the hybrid thin films increased with increases in the volume fraction of TiO$_2$ NPs, and their refractive index reached 1.86 at 20 vol% TiO$_2$ content. The present results demonstrate that the surface modification of TiO$_2$ NPs is an excellent method for the preparation of TiO$_2$ fillers applicable to the *ex situ* method for preparing various TiO$_2$/polymer hybrids.

Conflict of Interests

The authors declare that there is no conflict of interests regarding the publication of this paper.

Acknowledgments

References

[1] N. Nakayama and T. Hayashi, "Preparation and characterization of TiO_2 and polymer nanocomposite films with high refractive index," *Journal of Applied Polymer Science*, vol. 105, no. 6, pp. 3662–3672, 2007.

[2] L. Martinu and D. Poitras, "Plasma deposition of optical films and coatings: a review," *Journal of Vacuum Science & Technology A: Vacuum, Surfaces and Films*, vol. 18, no. 6, pp. 2619–2645, 2000.

[3] H. Ma, A. K. Y. Jen, and L. R. Dalton, "Polymer-based optical waveguides: materials, processing, and devices," *Advanced Materials*, vol. 14, no. 19, pp. 1339–1365, 2002.

[4] H. Dislich, "Plastics as optical materials," *Angewandte Chemie International Edition in English*, vol. 18, no. 1, pp. 49–59, 1979.

[5] C. Lü and B. Yang, "High refractive index organic-inorganic nanocomposites: design, synthesis and application," *Journal of Materials Chemistry*, vol. 19, no. 19, pp. 2884–2901, 2009.

[6] R. J. Nussbaumer, W. R. Caseri, P. Smith, and T. Tervoort, "Polymer-TiO_2 nanocomposites: a route towards visually transparent broadband UV filters and high refractive index materials," *Macromolecular Materials and Engineering*, vol. 288, no. 1, pp. 44–49, 2003.

[7] H. Althues, J. Henle, and S. Kaskel, "Functional inorganic nanofillers for transparent polymers," *Chemical Society Reviews*, vol. 36, no. 9, pp. 1454–1465, 2007.

[8] W. Caseri, "Nanocomposites of polymers and metals or semiconductors: historical background and optical properties," *Macromolecular Rapid Communications*, vol. 21, no. 11, pp. 705–722, 2000.

[9] J. L. H. Chau, Y.-M. Lin, A.-K. Li et al., "Transparent high refractive index nanocomposite thin films," *Materials Letters*, vol. 61, no. 14-15, pp. 2908–2910, 2007.

[10] S. M. Khaled, R. Sui, P. A. Charpentier, and A. S. Rizkalla, "Synthesis of TiO_2-PMMA nanocomposite: using methacrylic acid as a coupling agent," *Langmuir*, vol. 23, no. 7, pp. 3988–3995, 2007.

[11] M. Iijima, S. Takenouchi, I. W. Lenggoro, and H. Kamiya, "Effect of additive ratio of mixed silane alkoxides on reactivity with TiO_2 nanoparticle surface and their stability in organic solvents," *Advanced Powder Technology*, vol. 22, no. 5, pp. 663–668, 2011.

[12] M. Sabzi, S. M. Mirabedini, J. Zohuriaan-Mehr, and M. Atai, "Surface modification of TiO_2 nano-particles with silane coupling agent and investigation of its effect on the properties of polyurethane composite coating," *Progress in Organic Coatings*, vol. 65, no. 2, pp. 222–228, 2009.

[13] G. Guerrero, P. H. Mutin, and A. Vioux, "Anchoring of phosphonate and phosphinate coupling molecules on titania particles," *Chemistry of Materials*, vol. 13, no. 11, pp. 4367–4373, 2001.

[14] G. Arrachart, I. Karatchevtseva, A. Heinemann, D. J. Cassidy, and G. Triani, "Synthesis and characterisation of nanocomposite materials prepared by dispersion of functional TiO_2 nanoparticles in PMMA matrix," *Journal of Materials Chemistry*, vol. 21, no. 34, pp. 13040–13046, 2011.

[15] G. Guerrero, J. G. Alauzun, M. Granier, D. Laurencin, and P. H. Mutin, "Phosphonate coupling molecules for the control of surface/interface properties and the synthesis of nanomaterials," *Dalton Transactions*, vol. 42, no. 35, pp. 12569–12585, 2013.

[16] L. D. Freedman and G. O. Doak, "The preparation and properties of phosphonic acids," *Chemical Reviews*, vol. 57, no. 3, pp. 479–523, 1957.

[17] A. Bachinger and G. Kickelbick, "Photocatalytic stability of organic phosphonates and phosphates on TiO_2 nanoparticles," *Applied Catalysis A: General*, vol. 409-410, pp. 122–132, 2011.

[18] Y. Imai, A. Terahara, Y. Hakuta, K. Matsui, H. Hayashi, and N. Ueno, "Transparent poly(bisphenol A carbonate)-based nanocomposites with high refractive index nanoparticles," *European Polymer Journal*, vol. 45, no. 3, pp. 630–638, 2009.

[19] P. Tao, Y. Li, A. Rungta et al., "TiO_2 nanocomposites with high refractive index and transparency," *Journal of Materials Chemistry*, vol. 21, no. 46, pp. 18623–18629, 2011.

[20] A. T. Myller, J. J. Karhe, and T. T. Pakkanen, "Preparation of aminofunctionalized TiO_2 surfaces by binding of organophosphates," *Applied Surface Science*, vol. 257, no. 5, pp. 1616–1622, 2010.

[21] M. Kobayashi, R. Matsuno, H. Otsuka, and A. Takahara, "Precise surface structure control of inorganic solid and metal oxide nanoparticles through surface-initiated radical polymerization," *Science and Technology of Advanced Materials*, vol. 7, no. 7, pp. 617–628, 2006.

[22] P. Michel, J. Dugas, J. M. Cariou, and L. Martin, "Thermal variations of refractive index of PMMA, polystyrene, and poly(4-methyl-1-pentene)," *Journal of Macromolecular Science, Part B: Physics*, vol. 25, no. 4, pp. 379–394, 1986.

[23] M. Inkyo, Y. Tokunaga, T. Tahara et al., "Beads mill-assisted synthesis of poly methyl methacrylate (PMMA)-TiO_2 nanoparticle composites," *Industrial and Engineering Chemistry Research*, vol. 47, no. 8, pp. 2597–2604, 2008.

[24] A. H. Yuwono, B. Liu, J. Xue et al., "Controlling the crystallinity and nonlinear optical properties of transparent TiO_2-PMMA nanohybrids," *Journal of Materials Chemistry*, vol. 14, no. 20, pp. 2978–2987, 2004.

[25] L.-H. Lee and W.-C. Chen, "High-refractive-index thin films prepared from trialkoxysilane-capped poly(methylmethacrylate)-titania materials," *Chemistry of Materials*, vol. 13, no. 3, pp. 1137–1142, 2001.

[26] T. Asai, W. Sakamoto, and T. Yogo, "Synthesis of patterned and transparent TiO_2 nanoparticle/polymer hybrid films," *Materials Letters*, vol. 107, pp. 235–238, 2013.

[27] A. Convertino, G. Leo, M. Tamborra et al., "TiO_2 colloidal nanocrystals functionalization of PMMA: a tailoring of optical properties and chemical adsorption," *Sensors and Actuators B: Chemical*, vol. 126, no. 1, pp. 138–143, 2007.

[28] J.-M. Yeh, C.-J. Weng, K.-Y. Huang, H.-Y. Huang, Y.-H. Yu, and C.-H. Yin, "Thermal and optical properties of PMMA-titania hybrid materials prepared by sol-gel approach with HEMA as coupling agent," *Journal of Applied Polymer Science*, vol. 94, no. 1, pp. 400–405, 2004.

[29] C.-C. Chang, L.-P. Cheng, F.-H. Huang, C.-Y. Lin, C.-F. Hsieh, and W.-H. Wang, "Preparation and characterization of TiO_2 hybrid sol for UV-curable high-refractive-index organic-inorganic hybrid thin films," *Journal of Sol-Gel Science and Technology*, vol. 55, no. 2, pp. 199–206, 2010.

[30] Y. Wang, D. Zhang, L. Shi, L. Li, and J. Zhang, "Novel transparent ternary nanocomposite films of trialkoxysilane-capped poly(methyl methacrylate)/zirconia/titania with incorporating networks," *Materials Chemistry and Physics*, vol. 110, no. 2-3, pp. 463–470, 2008.

[31] S. Yamada, Z. Wang, and K. Yoshinaga, "Incorporation of TiO_2 nanoparticles, formed via sol-gel process in micelle of block copolymer, into poly(methyl methacrylate) to fabricate high refractive and transparent hybrid materials," *Chemistry Letters*, vol. 38, no. 8, pp. 828–829, 2009.

[32] T. Asai, W. Sakamoto, and T. Yogo, "In situ synthesis of transparent TiO_2 nanoparticle/polymer hybrid," *Journal of Materials Science*, vol. 48, no. 21, pp. 7503–7509, 2013.

[33] W. Du, H. Wang, W. Zhong, L. Shen, and Q. Du, "High refractive index films prepared from titanium chloride and methyl methacrylate via a non-aqueous sol-gel route," *Journal of Sol-Gel Science and Technology*, vol. 34, no. 3, pp. 227–231, 2005.

[34] S. Yamada, Z. Wang, E. Mouri, and K. Yoshinaga, "Crystallization of titania ultra-fine particles from peroxotitanic acid in aqueous solution in the present of polymer and incorporation into poly(methyl methacylate) via dispersion in organic solvent," *Colloid and Polymer Science*, vol. 287, no. 2, pp. 139–146, 2009.

[35] C. C. Li, S. J. Chang, and M. Y. Tai, "Surface chemistry and dispersion property of TiO_2 nanoparticles," *Journal of the American Ceramic Society*, vol. 93, no. 12, pp. 4008–4010, 2010.

[36] M. Iijima, S. Tajima, M. Yamazaki, and H. Kamiya, "Redispersion property of TiO_2 nanoparticles modified with oleyl-group," *Journal of the Society of Powder Technology, Japan*, vol. 49, no. 2, pp. 108–115, 2012.

[37] R. J. Nussbaumer, W. Caseri, T. Tervoort, and P. Smith, "Synthesis and characterization of surface-modified rutile nanoparticles and transparent polymer composites thereof," *Journal of Nanoparticle Research*, vol. 4, no. 4, pp. 319–323, 2002.

[38] P. Prêtre, L. M. Wu, A. Knoesen, and J. D. Swalen, "Optical properties of nonlinear optical polymers: a method for calculation," *Journal of the Optical Society of America B: Optical Physics*, vol. 15, no. 1, pp. 359–368, 1998.

[39] P. J. Thistlethwaite and M. S. Hook, "Diffuse reflectance fourier transform infrared study of the adsorption of oleate/oleic acid onto titania," *Langmuir*, vol. 16, no. 11, pp. 4993–4998, 2000.

[40] A. L. Willis, N. J. Turro, and S. O'Brien, "Spectroscopic characterization of the surface of iron oxide nanocrystals," *Chemistry of Materials*, vol. 17, no. 24, pp. 5970–5975, 2005.

[41] A. G. Emslie, F. T. Bonner, and L. G. Peck, "Flow of a viscous liquid on a rotating disk," *Journal of Applied Physics*, vol. 29, no. 5, pp. 858–862, 1958.

[42] C. R. Kurkjian and W. R. Prindle, "Perspectives on the history of glass composition," *Journal of the American Ceramic Society*, vol. 81, no. 4, pp. 795–813, 1998.

[43] I. H. Malitson, "Refraction and dispersion of synthetic sapphire," *Journal of the Optical Society of America*, vol. 52, no. 12, pp. 1377–1379, 1962.

Research Article

Attenuating Immune Response of Macrophage by Enhancing Hydrophilicity of Ti Surface

Xiaohan Dai,[1,2] Yan Wei,[2] Xuehui Zhang,[3] Song Meng,[2] Xiaoju Mo,[2] Xing Liu,[4] Xuliang Deng,[2] Li Zhang,[5] and Xuming Deng[1]

[1]*Key Laboratory of Zoonosis, Ministry of Education, Institute of Zoonosis, College of Veterinary Medicine, Jilin University, Changchun 130062, China*

[2]*Department of Geriatric Dentistry, Peking University School and Hospital of Stomatology, Beijing 100081, China*

[3]*Department of Dental Materials, Peking University School and Hospital of Stomatology, Beijing 100081, China*

[4]*First Clinical Division, Peking University School and Hospital of Stomatology, Beijing 100034, China*

[5]*Research Center for Nano-Biomaterials, Analytical & Testing Center, Sichuan University, Chengdu 610064, China*

Correspondence should be addressed to Li Zhang; zhangli9111@126.com and Xuming Deng; dengxm@jlu.edu.cn

Immune responses can determine the *in vivo* fate of implanted materials. The strategy for developing implants has shifted towards using materials with immunomodulatory activity. However, the immunoregulatory effect of hydrophilicity of titanium surface on the macrophage behavior and its underlying mechanism remain poorly understood. Here, the Ti surface hydrophilicity-dependent behavior of murine RAW264.7 macrophages was investigated *in vitro*. Two laboratory models with significantly different surface hydrophilicity and similar roughness were established with Ti-polished and Ti-H_2O_2 surfaces. The results of cell morphology observation showed that the Ti-H_2O_2 surface yielded enhanced cell adhesion and less multinucleated cell formation. CCK-8 assay indicated that the growth rate of macrophage on Ti-H_2O_2 surface is higher than that of Ti-polished. ELISA assay result revealed lower level of proinflammatory factor TNF-α and higher level of anti-inflammatory factor IL-10 on the Ti-H_2O_2 surface compared to Ti-polished. Subsequently, immunofluorescence and western blotting analysis showed that activation of the NF-κB-TNF-α pathway might be involved in the modulation of the immune response by surface hydrophilicity. Together, these results suggested that relative high hydrophilic Ti surface might attenuate the immune response of macrophage by activating NF-κB signaling. These findings could provide new insights into designing implant devices for orthopedic applications.

1. Introduction

Because of excellent mechanical and corrosion resistance properties, titanium- (Ti-) based materials have been widely used in making dental and orthopedic implants [1, 2]. However, immune responses mediated by inflammatory cells have been found to significantly impact the biocompatibility and function of implanted medical devices or prostheses and can ultimately precipitate their clinical failure [3, 4]. The paradigm for developing an ideal implant material has been shifted using from inert to immunomodulatory materials, emphasizing the importance of immune cells in the evaluation of a candidate material [5]. Macrophages, the major effector cells in the immune response to implants,

have been reported to determine the long-term immune response and outcome of an inflammatory reaction [6, 7]. Modulation of adhesion and activation of macrophages with anti-inflammatory drugs can reduce immune responses [8]. However, in the clinic the long-term systematic use of drugs can compromise host defenses, leading to impaired immune responses and an increased potential for infection [9]. To avoid this problem, appropriate surface modifications of implants have been considered as an alternative approach to inhibit or attenuate inflammation reaction temporarily for achieving high success rates [10–12].

Recently, several types of surface modification methods have been introduced to slow macrophage-mediated immune

responses triggered by Ti-based implants, including coatings, sand blasting, and acid etching [13–15]. However, delamination of the coating was found to sometimes occur during implant placement or in load bearing situations, which was probably caused by poor stability of the coating bound to the substrate [13]. Additionally, normal bone mineralization can be inhibited by the release of constituents, such as Al_2O_3 or Ta_2O_5, from the material when they were modified by sand blasting [14]. The etched implant surface has been shown to be capable of promoting osseointegration because of hydrophilicity [15]. Furthermore, surface hydrophilicity of Ti-based implants has been established to modulate osteogenic cell adhesion, proliferation, and differentiation [16]. Therefore, it can be hypothesized that incorporating surface hydrophilicity might be a promising alternative for regulating macrophage behavior. Nevertheless, little attention has been paid to the immunoregulatory effect of surface hydrophilicity of titanium on the macrophage behavior and data about this topic has been needed.

Herein, the purpose of this work is to investigate the effects of the hydrophilicity of Ti surface on macrophage behavior *in vitro*. Two kinds of Ti surfaces with different hydrophilicity including polished Ti surface (Ti-polished) and etched Ti surface (Ti-H_2O_2) were used in present study. The morphology, roughness, and wettability of the Ti surfaces were firstly characterized. The morphology of macrophage RAW264.7 cells on the Ti surfaces was observed by scanning electron microscopy (SEM) and confocal laser scanning microscopy (CLSM). Cell proliferation was assessed by CCK-8 assay. The activation status of macrophages was quantified by measuring TNF-α and IL-10 secretion by ELISA assay. Subsequently, the underlying mechanism of modulation of surface hydrophilicity on the immune response was explored by both immunofluorescence and western blotting analysis.

2. Materials and Methods

2.1. Samples Preparation. Ti disks with 20 mm in diameter and 2 mm thick were used to prepare two kinds of different Ti surfaces including hydrophilic (Ti-H_2O_2) and polished (Ti-polished). Ti-polished surfaces were prepared by polishing with sand paper from 400 to 1500 grit. Ti-H_2O_2 surfaces were obtained via immersing the Ti disks in 10% H_2O_2 solution for 24 h.

2.2. Sample Characterization. The surfaces were imaged by scanning electron microscope (SEM, Hitachi S-4800, Tokyo, Japan) at a 15 kV accelerating voltage. Atomic force microscopy (AFM, SPA-300HV, Seiko, Tokyo, Japan) was performed to measure the surface roughness parameter Ra over a $10 \times 10 \, \mu$m area. X-ray photoelectron spectroscopy (XPS, Thermo V6 Escalab 250, West Sussex, UK) was carried out to analyze element composition of these Ti surfaces. Surface water contact angles of Ti materials were measured using a drop shape analysis system (JY-82A, China).

2.3. Cell Culture. Murine macrophage-like RAW264.7 cells were obtained from Cell Resource Center, IBMS,

CAMS/PUMC, and cultured in DMEM medium with 10% FBS (Gbico, Carlsbad, CA, USA). After two passages, cells were plated at 2.0×10^5 cells per well in 24-well plates.

2.4. Cell Morphology Observation

2.4.1. Scanning Electron Microscopy (SEM). Cells were incubated on Ti disks for 1, 3, and 7 days. After incubation, cells were fixed with 2.5% glutaraldehyde and incubated with 0.18 mol/L sucrose solution. Samples were dehydrated through a graded ethanol series (30–100%) and air-dried.

2.4.2. Confocal Laser Scanning Microscopy (CLSM). Cells were cultured on Ti disks for 7 days. Cells were then fixed with 4.0% paraformaldehyde, treated with Alexa Fluor 546-phalloidin (50 μg/mL) for 1 h at room temperature, and then stained with DAPI for 10 min according to the manufacturer's directions. Images of the stained cells were acquired using CLSM (Zeiss, LSM 780, Oberkochen, Germany).

2.5. Cell Proliferation Assay. To assess macrophage activity on Ti disks, cell counting kit-8 (CCK-8) was performed on days 1, 3, 5, and 7. According to the manufacturer's directions, CCK-8 solution was added to each well of the plate at a ratio of 1 : 10 and then was incubated for 2 h in an incubator. After incubation, absorbance was measured using a microplate reader (Bio-Rad, Hercules, CA, USA).

2.6. Cell Cytokine Secretion Examination. To analyze cytokine secretion, cells were cocultured with Ti disks and supernatants were collected at days 1, 3, 5, and 7. The levels of TNF-α and IL-10 in the supernatants were quantified using an ELISA kit (R&D Systems, Minneapolis, MN, USA) according to the manufacturer's directions.

2.7. Assessment of NF-κB. In accordance with the manufacturer's directions, cells grown on Ti disks for 3 days were fixed, blocked, and incubated with anti-NF-κB p65 primary antibody at 4°C overnight. Then samples were treated with an appropriate Cy3-conjugated secondary antibody for 1 h and stained with DAPI for 5 min at room temperature. A confocal microscopy (Zeiss, LSM 780, Oberkochen, Germany) was used to observe NF-κB activation.

2.8. Statistical Analysis. Data were analyzed using an independent Student's t-test and are presented as means ± standard deviation (S.D.). $P < 0.05$ was considered to indicate a statistically significant difference.

3. Results and Discussion

Given the importance of macrophages in bone dynamics, some studies have investigated interactions between bone substitute biomaterials (e.g., bioceramics, polymers, or titanium) and macrophages [11, 17, 18]. However, in the field of implant materials research, the immunoregulatory effect of surface hydrophilicity of titanium on the macrophage
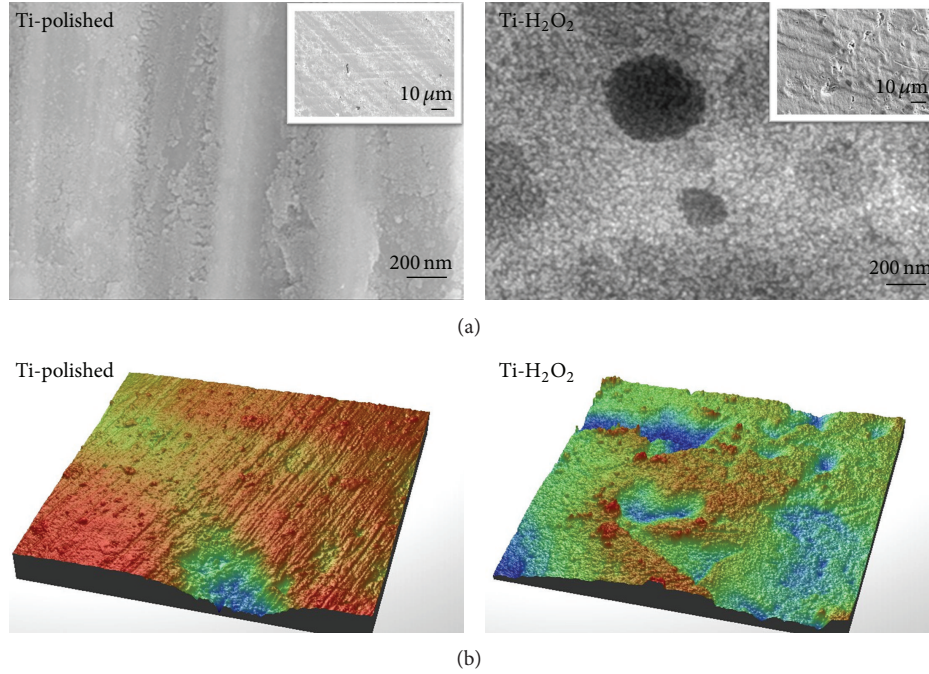
(a)

(b)

FIGURE 1: Scanning electron microscopy (a) and atomic force microscopy (b) images of the Ti-polished and Ti-H$_2$O$_2$ surfaces.

behavior and its underlying mechanism still remain largely unknown. To devise a strategy for Ti surface design for clinical regenerative therapies, additional data regarding the effects of surface hydrophilicity on immune responses and the underlying mechanisms involved will be required. The results in present study demonstrated that a more hydrophilic Ti surface might more favorably attenuate macrophage immune responses via NF-κB-TNF-α signaling.

The SEM observation clearly indicated that Ti-H$_2$O$_2$ possessed a nanostructure with a uniformly distributed nanoparticle compared to Ti-polished surface (Figure 1(a)). As shown in Table 1, AFM images showed that the two kinds of Ti surfaces shared similar roughness that Ra of Ti-polished and Ti-H$_2$O$_2$ were 23.25 ± 5.89 nm and 87.13 ± 23.72 nm. While Ti-H$_2$O$_2$ surface ($35.21 \pm 3.08°$) was found to be more hydrophilic than the Ti-polished surface ($64.46 \pm 2.384°$). The quantified element composition given by XPS indicated a little increment in the O1s peak for the hydrophilic Ti-H$_2$O$_2$ surface compared to hydrophobic Ti-polished surface, supported by atomic ratios of oxygen (Figure 2 and Table 2). The results were consistent with previous report that O$_2^-$ and –OH group would be generated on surface when treated with H$_2$O$_2$ solution [19]. Thus, the two kinds of Ti surface models used in our work presented significantly different surface hydrophilicity and similar roughness.

The proliferation rate of cells on the Ti surfaces partially reflects biocompatibility of the materials, which is essential for implant survival. Mouse macrophage RAW264.7 cells viability on different Ti surfaces was measured by CCK-8 assay for 1, 3, 5, or 7 days (Figure 3). Overall, relative high hydrophilic Ti-H$_2$O$_2$ surface resulted in enhanced cell proliferation. Although cell viabilities on different surfaces

TABLE 1: Water contact angle and surface roughness of the Ti samples.

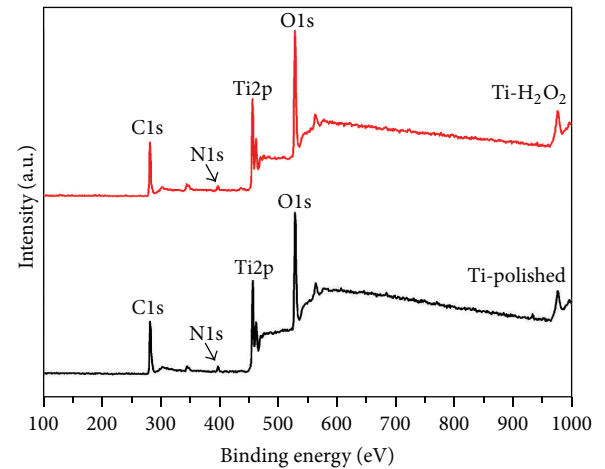| Sample	Contact angle (°)	Ra (nm)
Ti-H$_2$O$_2$	35.21 ± 3.08	87.13 ± 23.72
Ti-polished	64.46 ± 2.38	23.25 ± 5.89

FIGURE 2: X-ray photoelectron spectroscopy analysis of the Ti-polished and Ti-H$_2$O$_2$ surfaces.

were similar after 1 day of culture, significantly higher cell viabilities were found on hydrophilic Ti-H$_2$O$_2$ surfaces compared to hydrophobic Ti-polished surfaces after culture for 3 days. Additionally, this trend continued to be maintained

TABLE 2: Element distribution recorded by XPS analysis.

	Ti-H_2O_2	Ti-polished
C1s	42.31%	44.71%
Ti2p	13.35%	13.15%
N1s	2.58%	2.72%
O1s	41.77%	39.44%
F1s	0	0
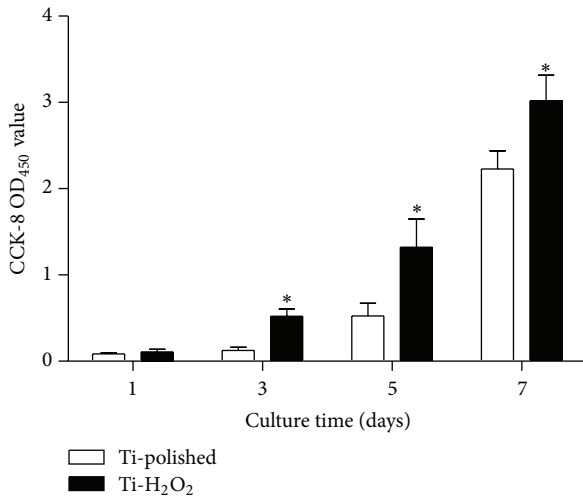
FIGURE 3: The effect of surface hydrophilicity on RAW264.7 cells viability measured by CCK-8 ($^*P < 0.05$).

at days 5 and 7. These data demonstrate that hydrophilic Ti-H_2O_2 surfaces are more biocompatible than hydrophobic Ti-polished surfaces. The excellent biocompatibility of Ti-H_2O_2 surfaces for macrophage may be benefit for wound healing. Previous studies also indicated that improved wound healing was associated with enhanced macrophage recruitment [20].

The influence of materials on macrophage morphology played an important role in the assessment of materials immunoregulatory property. Cell shape changes have been reported to be related to different functional states of cells, such as proliferation, nuclear organization, and differentiation [21–23]. Additionally, cell shape was found to modulate the phenotypic polarization of macrophages. In this study, we clearly observed different initial cell adhesion behaviors of macrophages on two types of Ti surfaces after 1 day of culture (Figure 4(a)). More filopodia were observed on hydrophobic Ti-polished surfaces than on those of hydrophilic Ti-H_2O_2 surfaces. Filopodia are specialized macrophage adhesion structures that can form in the early stages of cell adhesion and consist of punctuate F-actin on plasma membrane extensions [24], which facilitate attachment and migration [25, 26]. It has been proposed that a round shape might indicate a resting nonactivated macrophage, whereas the presence of multiple filopodia represents an activated macrophage [26]. Therefore, the difference in filopodia numbers clearly suggested that macrophages would be more prone to become activated on the hydrophobic Ti-H_2O_2 surface than on the hydrophilic Ti-polished.

After 7 days of culture, SEM observation showed that several suspected FBGCs formed by cell fusion appeared on Ti-polished surfaces, whereas only elongated cells with numerous cellular projections were present on Ti-H_2O_2 surfaces (Figure 4(a)). Furthermore, immunofluorescence staining of cytoskeleton organization and CLSM analysis of nuclei confirmed that more FBGCs formed on hydrophobic Ti-polished surfaces than on hydrophilic Ti-H_2O_2 surfaces (Figure 4(b)). This phenomenon was consistent with previous work of Collier et al. who reported that hydrophilic surfaces exert a robust inhibitory effect on FBGCs formation [25]. The formation of FBGCs in response to implanted biomaterials or medical devices, also known as a foreign body reaction, has been implicated in the degradation and cracking of implanted material and in initiating the formation of fibrous capsules that surround the implanted biomaterials [27, 28]. FBGCs with multiple nuclei might release profibrotic factors, including transforming growth factor beta (TGF-β) and platelet-derived growth factor (PDGF), which could in turn activate fibroblasts and endothelial cells to facilitate the subsequent fibrotic encapsulation and inflammatory response [21, 29]. Thus, increased FBGCs formation on hydrophobic Ti-polished surfaces might imply a more serious inflammatory response of macrophages, and hydrophilic Ti-H_2O_2 surfaces might be more beneficial for inhibiting inflammation.

Notably, the two types of Ti surfaces also yielded macrophages with significantly different cell morphologies. More macrophages with spindles appeared on Ti-H_2O_2 surface, whereas almost all macrophages exhibited a round cell appearance with multiple filopodia on Ti-polished surfaces (Figure 4(b)). These results suggested that Ti-H_2O_2 surfaces might promote the polarization of macrophages towards a prohealing macrophage phenotype, implying that they can exert anti-inflammatory activities and improve wound healing responses. Our results were also consistent with previous report that prohealing cells exhibited a more elongated shape compared to proinflammatory cells [30]. By contrast, the round cell morphology on Ti-polished surfaces might be a phenotypic marker of proinflammatory macrophages, leading to fibrotic responses and inflammation around any materials.

It has been well established that the immune system is closely related to skeletal development and that they share many common cytokines [31]. Those cytokines can mediate macrophage-dependent inflammatory cascades that are triggered by innate immune activation and act to influence implant integration and osteogenesis [32–35]. Proinflammatory cytokines can enhance osteoclast differentiation and resorbing activity and inhibit osteoblast activity and bone formation, whereas anti-inflammatory cytokines exert opposite effects [33–35]. TNF-α, a key proinflammatory regulator that is mainly released by stimulated macrophages, contributes to fibrosis via TNF receptor 2, which then acts through extracellular signal-regulated kinase 1/2 (ERK1/2) to stimulate cell proliferation and inhibit collagen degradation [33]. TNF-α was also found to activate the ERK-specific mitogen-activated protein kinase (MAPK) pathway, leading to increased TGF-β1 production, which can facilitate fibrosis
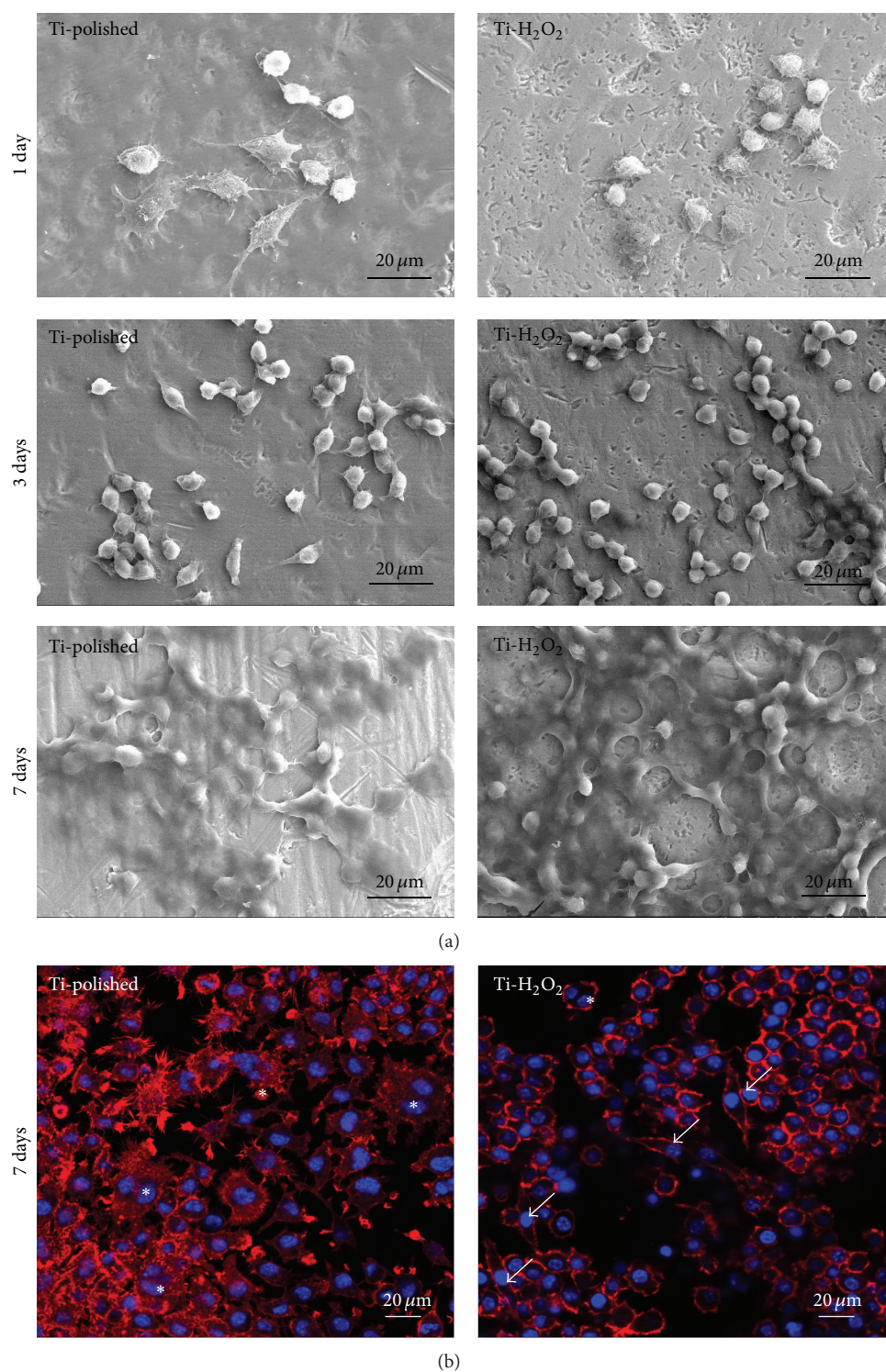
(a)

(b)

FIGURE 4: The influence of surface hydrophilicity on cell morphology and FBGCs formation. (a) Scanning electron microscopy images of macrophages cultured on Ti-polished or Ti-H_2O_2 surfaces for 1, 3, and 7 days. (b) The cytoskeleton organization of macrophages cultured on Ti-polished and Ti-H_2O_2 surfaces for 7 days. White asterisks indicate FBGCs. White arrow indicates the spindle cells. F-actin and cell nuclei were immunostained with Alexa Fluor 546-phalloidin (red) and DAPI (blue), respectively.
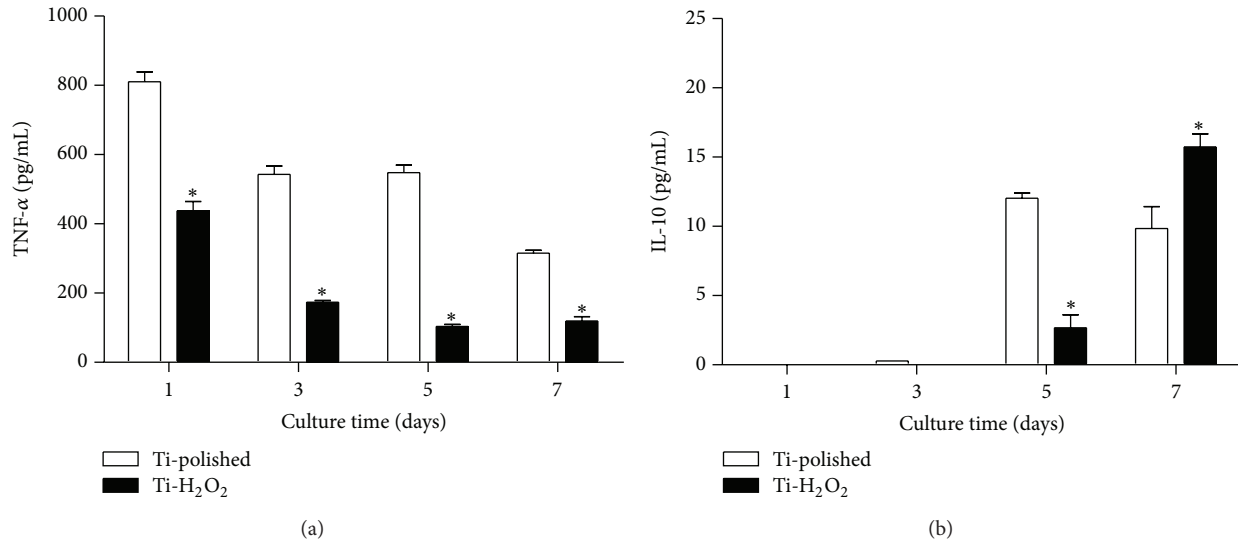
(a)

(b)

FIGURE 5: The levels of secreted TNF-α (a) and IL-10 (b) in the supernatants of macrophages cultured on different surfaces for 1, 3, 5, and 7 days ($^{*}P < 0.05$).

[36]. The ELISA quantitative analysis showed that TNF-α secretion was significantly increased on hydrophobic Ti-polished surfaces compared to hydrophilic Ti-H$_2$O$_2$ surfaces at all time points (Figure 5(a)). Production of the proinflammatory cytokine TNF-α peaked on both Ti surfaces after 1 day of culture and then decreased with the time, suggesting that a robust inflammatory response occurred at an early stage of culture. IL-10 is a typical anti-inflammatory cytokine that plays a critical role in suppressing proinflammatory cytokines [35]. In contrast to the pattern of proinflammatory cytokine secretion, production of the anti-inflammatory cytokine IL-10 increased in a time-dependent manner on both Ti surfaces (Figure 5(b)). These results indicated that the surface wettability of Ti implants has a profound effect on the immune response of macrophages. Our results are also in line with previous studies. Lee et al. reported that hydrophilic titanium elicited fewer inflammation reactions [37]. Tsang et al. demonstrated that hydrophilic carbon nanofibers (CNFs) caused a weaker macrophage-dependent inflammatory response than hydrophobic CNFs [38]. Taken together, hydrophilic Ti-H$_2$O$_2$ surfaces may potentially be better osteogenesis-promoting materials, due to the ability to inhibit the production of proinflammatory cytokines and promote anti-inflammatory molecule secretion.

The confirmation that macrophage behavior can be affected by different hydrophilic Ti surfaces prompted us to further explore the possible mechanism underlying the hydrophilicity-dependent inflammatory response to implanted materials. Activation of the NF-κB pathway, a key intracellular regulator of inflammatory signaling, has been known to promote the secretion of proinflammatory cytokines, including TNF-α and IL-1β [30, 31]. In our work, the significantly different levels of TNF-α production on these two Ti surfaces implied that the NF-κB pathway might be critical in the hydrophilicity-dependent immune

response. The NF-κB family consists of five members—p50, p52, p65 (RelA), c-Rel, and RelB—that share an N-terminal Rel homology domain (RHD) [32]. Most of these proteins can form different NF-κB homodimers and heterodimers. Among the heterodimers, p50/p65 heterodimers are considered to be key mediators of gene expression [33]. Therefore, p65 was chosen in present research as the mark for NF-κB expression. It can be seen from immunofluorescence images and western blotting results in our work that more NF-κB p65 was present in macrophages cultured on Ti-polished surfaces than in those cultured on Ti-H$_2$O$_2$ surfaces (Figure 6). Combined with inflammatory cytokines secretion results, we can conclude that NF-κB signaling may be involved in the regulation effects of hydrophilic Ti surfaces on the acute phase inflammation response of macrophage. Conclusively, these findings could provide an approach to optimize the Ti implant materials for desired bone integration and orthopedic applications.

4. Conclusions

In this study, Ti surface hydrophilicity-dependent immune response and underlying mechanism were explored. The results showed that more hydrophilic Ti surface (Ti-H$_2$O$_2$) yielded enhanced cell adhesion, increased proliferation, and less multinucleated cells formation. The hydrophilic Ti-H$_2$O$_2$ surfaces that exhibited the inhibition in the production of pro-inflammatory cytokines and the promotion in the secretion of anti-inflammatory molecules may be more beneficial to serve as potentially osteogenesis-promoting materials. Moreover, it was revealed that hydrophilic Ti surface might be more favorable in attenuating macrophage immune response via NF-κB signaling. These results may provide new insight in surface-designing of novel implant devices.
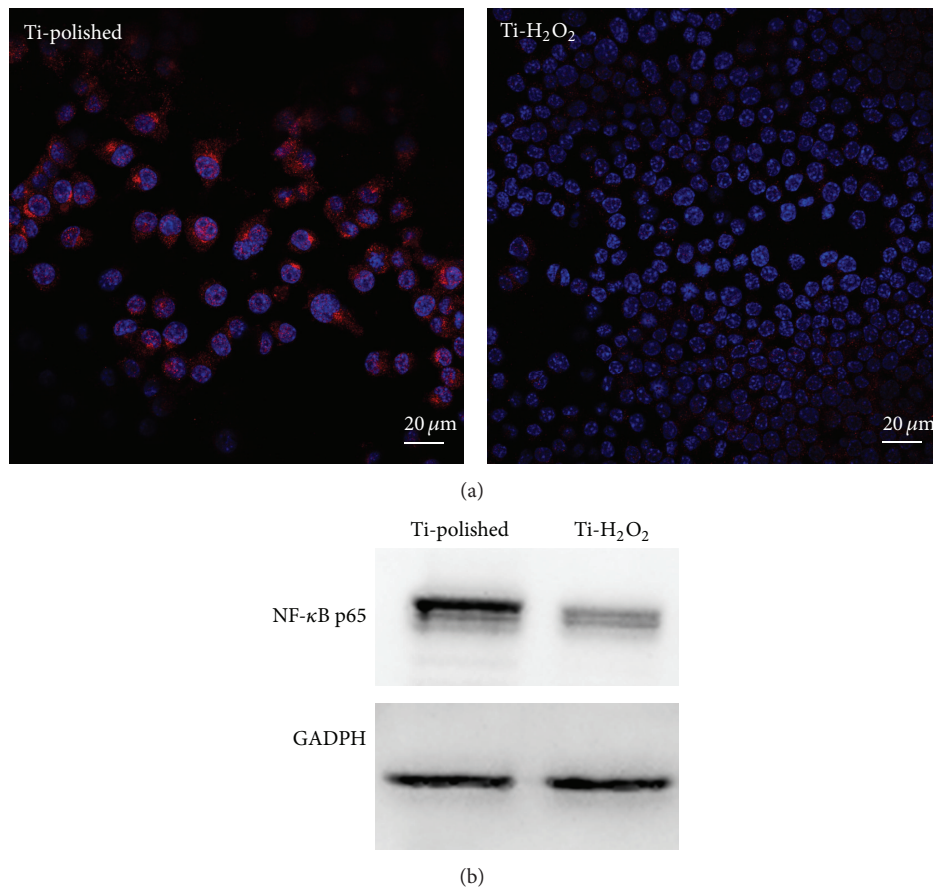
(a)

(b)

FIGURE 6: Immunofluorescence images (a) and western blotting images (b) of NF-κB p65 in macrophage nuclei. NF-κB p65 and cell nuclei were immunostained by Cy3 (red) and DAPI (blue), respectively.

Conflict of Interests

The authors declare that there is no conflict of interests regarding the publication of this paper.

Acknowledgments

References

[1] M. Schuier, D. Trentin, M. Textor, and S. G. Tosatti, "Biomedical interfaces: titanium surface technology for implants and cell carriers," *Nanomedicine*, vol. 1, no. 4, pp. 449–463, 2006.

[2] D. A. Puleo and A. Nanci, "Understanding and controlling the bone-implant interface," *Biomaterials*, vol. 20, no. 23-24, pp. 2311–2321, 1999.

[3] S. A. Eming, T. Krieg, and J. M. Davidson, "Inflammation in wound repair: molecular and cellular mechanisms," *Journal of Investigative Dermatology*, vol. 127, no. 3, pp. 514–525, 2007.

[4] J. M. Schierholz and J. Beuth, "Implant infections: a haven for opportunistic bacteria," *Journal of Hospital Infection*, vol. 49, no. 2, pp. 87–93, 2001.

[5] Z. Chen, X. Mao, L. Tan et al., "Osteoimmunomodulatory properties of magnesium scaffolds coated with β-tricalcium phosphate," *Biomaterials*, vol. 35, no. 30, pp. 8553–8565, 2014.

[6] T. A. Wynn, A. Chawla, and J. W. Pollard, "Macrophage biology in development, homeostasis and disease," *Nature*, vol. 496, no. 7446, pp. 445–455, 2013.

[7] M. Bartneck, K. H. Heffels, Y. Pan, M. Bovi, G. Zwadlo-Klarwasser, and J. Groll, "Inducing healing-like human primary macrophage phenotypes by 3D hydrogel coated nanofibres," *Biomaterials*, vol. 33, no. 16, pp. 4136–4146, 2012.

[8] Y. Zhong and R. V. Bellamkonda, "Dexamethasone-coated neural probes elicit attenuated inflammatory response and neuronal loss compared to uncoated neural probes," *Brain Research*, vol. 1148, no. 1, pp. 15–27, 2007.

[9] H. Hackstein and A. W. Thomson, "Dendritic cells: emerging pharmacological targets of immunosuppressive drugs," *Nature Reviews Immunology*, vol. 4, no. 1, pp. 24–34, 2004.

[10] A. Eckhardt, T. Harorli, J. Limtanyakul et al., "Inhibition of cytokine and surface antigen expression in LPS-stimulated

murine macrophages by triethylene glycol dimethacrylate," *Biomaterials*, vol. 30, no. 9, pp. 1665–1674, 2009.

[11] D. P. Vasconcelos, A. C. Fonseca, M. Costa et al., "Macrophage polarization following chitosan implantation," *Biomaterials*, vol. 34, no. 38, pp. 9952–9959, 2013.

[12] D. Naskar, S. Nayak, T. Dey, and S. C. Kundu, "Non-mulberry silk fibroin influence osteogenesis and osteoblast-macrophage cross talk on titanium based surface," *Scientific Reports*, vol. 4, article 4745, 2014.

[13] A. Kamali, A. Hussain, C. Li et al., "Tribological performance of various CoCr microstructures in metal-on-metal bearings: the development of a more physiological protocol in vitro," *The Journal of Bone and Joint Surgery. British Volume*, vol. 92, no. 5, pp. 717–725, 2010.

[14] C.-K. Cheng, N.-K. Yao, H.-C. Liu, and K.-S. Lee, "Influences of configuration changes of the patella on the knee extensor mechanism," *Clinical Biomechanics*, vol. 11, no. 2, pp. 116–120, 1996.

[15] P. R. Klokkevold, R. D. Nishimura, M. Adachi, and A. Caputo, "Osseointegration enhanced by chemical etching of the titanium surface. A torque removal study in the rabbit," *Clinical Oral Implants Research*, vol. 8, no. 6, pp. 442–447, 1997.

[16] H. Aita, W. Att, T. Ueno et al., "Ultraviolet light-mediated photofunctionalization of titanium to promote human mesenchymal stem cell migration, attachment, proliferation and differentiation," *Acta Biomaterialia*, vol. 5, no. 8, pp. 3247–3257, 2009.

[17] Z. Chen, C. Wu, W. Gu, T. Klein, R. Crawford, and Y. Xiao, "Osteogenic differentiation of bone marrow MSCs by β-tricalcium phosphate stimulating macrophages via BMP2 signalling pathway," *Biomaterials*, vol. 35, no. 5, pp. 1507–1518, 2014.

[18] K. S. Tan, L. Qian, R. Rosado, P. M. Flood, and L. F. Cooper, "The role of titanium surface topography on J774A.1 macrophage inflammatory cytokines and nitric oxide production," *Biomaterials*, vol. 27, no. 30, pp. 5170–5177, 2006.

[19] M. A. Baker, S. L. Assis, O. Z. Higa, and I. Costa, "Nanocomposite hydroxyapatite formation on a Ti-13Nb-13Zr alloy exposed in a MEM cell culture medium and the effect of H_2O_2 addition," *Acta Biomaterialia*, vol. 5, no. 1, pp. 63–75, 2009.

[20] M. C. Robson, D. A. Dubay, X. Wang, and M. G. Franz, "Effect of cytokine growth factors on the prevention of acute wound failure," *Wound Repair and Regeneration*, vol. 12, no. 1, pp. 38–43, 2004.

[21] S. Franz, S. Rammelt, D. Scharnweber, and J. C. Simon, "Immune responses to implants—a review of the implications for the design of immunomodulatory biomaterials," *Biomaterials*, vol. 32, no. 28, pp. 6692–6709, 2011.

[22] M. Versaevel, T. Grevesse, and S. Gabriele, "Spatial coordination between cell and nuclear shape within micropatterned endothelial cells," *Nature Communications*, vol. 3, p. 671, 2012.

[23] R. McBeath, D. M. Pirone, C. M. Nelson, K. Bhadriraju, and C. S. Chen, "Cell shape, cytoskeletal tension, and RhoA regulate stem cell lineage commitment," *Developmental Cell*, vol. 6, no. 4, pp. 483–495, 2004.

[24] R. Trindade, T. Albrektsson, P. Tengvall, and A. Wennerberg, "Foreign body reaction to biomaterials: on mechanisms for buildup and breakdown of osseointegration," *Clinical Implant Dentistry and Related Research*, 2014.

[25] T. O. Collier, J. M. Anderson, W. G. Brodbeck, T. Barber, and K. E. Healy, "Inhibition of macrophage development and foreign body giant cell formation by hydrophilic interpenetrating polymer network," *Journal of Biomedical Materials Research A*, vol. 69, no. 4, pp. 644–650, 2004.

[26] E. Saino, M. L. Focarete, C. Gualandi et al., "Effect of electrospun fiber diameter and alignment on macrophage activation and secretion of proinflammatory cytokines and chemokines," *Biomacromolecules*, vol. 12, no. 5, pp. 1900–1911, 2011.

[27] W. F. A. den Dunnen, P. H. Robinson, R. van Wessel, A. J. Pennings, M. B. M. van Leeuwen, and J. M. Schakenraad, "Long–term evaluation of degradation and foreign–body reaction of subcutaneously implanted poly(DL–lactide–ε–caprolactone)," *Journal of Biomedical Materials Research*, vol. 36, no. 3, pp. 337–346, 1997.

[28] J. M. Anderson, A. Rodriguez, and D. T. Chang, "Foreign body reaction to biomaterials," *Seminars in Immunology*, vol. 20, no. 2, pp. 86–100, 2008.

[29] N. A. Athanasou and J. Quinn, "Immunophenotypic differences between osteoclasts and macrophage polykaryons: immunohistological distinction and implications for osteoclast ontogeny and function," *Journal of Clinical Pathology*, vol. 43, no. 12, pp. 997–1003, 1990.

[30] F. Y. McWhorter, T. Wang, P. Nguyen, T. Chung, and W. F. Liu, "Modulation of macrophage phenotype by cell shape," *Proceedings of the National Academy of Sciences of the United States of America*, vol. 110, no. 43, pp. 17253–17258, 2013.

[31] T. Albrektsson and C. Johansson, "Osteoinduction, osteoconduction and osseointegration," *European Spine Journal*, vol. 10, supplement 2, pp. S96–S101, 2001.

[32] P. Palmqvist, E. Persson, H. H. Conaway, and U. H. Lerner, "IL-6, leukemia inhibitory factor, and oncostatin M stimulate bone resorption and regulate the expression of receptor activator of NF-kappaB ligand, osteoprotegerin, and receptor activator of NF-kappaB in mouse calvariae," *Journal of Immunology*, vol. 169, no. 6, pp. 3353–3362, 2002.

[33] A. L. Theiss, J. G. Simmons, C. Jobin, and P. K. Lund, "Tumor necrosis factor (TNF) alpha increases collagen accumulation and proliferation in intestinal myofibroblasts via TNF receptor 2," *The Journal of Biological Chemistry*, vol. 280, no. 43, pp. 36099–36109, 2005.

[34] Z. Chen, Y. Liu, B. Sun et al., "Polyhydroxylated metallofullerenols stimulate IL-1β secretion of macrophage through TLRs/MyD88/NF-κB pathway and NLRP$_3$ inflammasome activation," *Small*, vol. 10, no. 12, pp. 2362–2372, 2014.

[35] C. Bogdan, Y. Vodovotz, and C. Nathan, "Macrophage deactivation by interleukin 10," *The Journal of Experimental Medicine*, vol. 174, no. 6, pp. 1549–1555, 1991.

[36] D. E. Sullivan, M. Ferris, D. Pociask, and A. R. Brody, "Tumor necrosis factor-α induces transforming growth factor-β1 expression in lung fibroblasts through the extracellular signal-regulated kinase pathway," *The American Journal of Respiratory Cell and Molecular Biology*, vol. 32, no. 4, pp. 342–349, 2005.

[37] S. Lee, J. Choi, S. Shin et al., "Analysis on migration and activation of live macrophages on transparent flat and nanostructured titanium," *Acta Biomaterialia*, vol. 7, no. 5, pp. 2337–2344, 2011.

[38] M. Tsang, Y. W. Chun, Y. M. Im, D. Khang, and T. J. Webster, "Effects of increasing carbon nanofiber density in polyurethane composites for inhibiting bladder cancer cell functions," *Tissue Engineering—Part A*, vol. 17, no. 13-14, pp. 1879–1889, 2011.

Research Article

Preparation and Photocatalytic Performance of Nano-TiO$_2$ Codoped with Iron III and Lanthanum III

Wei Guan, Fangying Ji, Zhigang Xie, Rongan Li, and Nan Mei

Chongqing Key Laboratory of Environmental Materials & Remediation Technologies,
Chongqing University of Arts and Sciences, Chongqing 402160, China

Correspondence should be addressed to Fangying Ji; jfy@cqu.edu.cn

Nanoscale titanium dioxide (nano-TiO$_2$) was modified via metal doping to improve its photocatalytic activity and utilization of visible light. Nano-TiO$_2$ doped with iron III (Fe^{3+}) only, lanthanum III (La^{3+}) only, and both Fe^{3+}/La^{3+} was prepared using the sol-gel method. The photocatalytic activities of the three forms of doped nano-TiO$_2$ were evaluated. Metal codoping limited crystal growth of crystal, and the sol-gel method was shown to be an effective technique for doping the lattice of TiO$_2$ with Fe^{3+} and La^{3+}. Codoping of nano-TiO$_2$ with the tombarthite metal mixture had a synergistic effect of the photocatalytic performance, with the codoped nano-TiO$_2$ exhibiting a performance greater than the sum of those of the single-doped nano-TiO$_2$ samples. Kinetic studies showed that the photodegradation reaction of methyl orange by nano-TiO$_2$ follows the Langmuir-Hinshelwood first order mechanism.

1. Introduction

Global environmental pollution and energy shortages are becoming increasingly serious problems [1, 2]. The control of environmental pollution has become a major and urgent topic of concern. In 1972, Fujishima and Honda published the first article in *Nature* declaring that the semiconductor titanium dioxide crystal electrode has the ability to photocatalytically split water to produce hydrogen [3, 4]. This discovery signaled the beginning of heterogeneous photocatalysis research in the area of semiconductors. Photocatalysis technology, as a representative of green chemistry, is widely applied in many areas, such as wastewater treatment, air purification, and solar energy transfer and storage [5–7].

Nanoscale titanium dioxide (nano-TiO$_2$) has become a preferred material for these applications due to its high catalytic activity and stable chemical properties and because it is cheap and nontoxic [8–10]. However, there are some disadvantages of using nano-TiO$_2$, such as the high recombination rate of photoproduced electron-hole pairs, low quantum efficiency, and poor photocatalytic performance [9–12]. Nano-TiO$_2$ can only use the ultraviolet portion of the solar spectrum range (only 3–5% of the total range) due to a wide band gap (3.2 eV), which leads to low effective utilization of sunlight [13–15]. Researchers have used a variety of methods to modify nano-TiO$_2$, including noble metal modification, compound semiconductor, dye sensitization, metal ion doping, and others [16–19]. With these modification methods, the recombination rate of photogenerated electron-hole pairs of nano-TiO$_2$ photocatalyst is decreased, and the photocatalysis efficiency and range of visible light that generates a response are increased [20–23]. Our research group found that modification by codoping with two elements can increase the visible light photocatalytic activity of nano-TiO$_2$.

The main aim of the present study was to increase the visible light photocatalytic activity of nano-TiO$_2$. The originality and significance of this study are described as follows.

(1) We prepared nano-TiO$_2$ photocatalysts by doping of nano-TiO$_2$ powder with iron III ions (Fe^{3+}), lanthanum III ions (La^{3+}), or both via the sol-gel method.

(2) The microstructure and chemical composition of the prepared nano-TiO$_2$ photocatalysts were analyzed by X-ray diffraction (XRD), X-ray photoelectron

spectroscopy (XPS), fluorescence spectroscopy (FS), and UV-Visible absorption spectroscopy (UV-Vis). Furthermore, the catalytic mechanism was revealed in the present study.

(3) The effects of various parameters, such as the roasting temperature, roasting time, catalyst dosage, initial pH value, doping amount, and doping type on the photocatalytic activity were investigated. In conclusion, a new mechanism for metal doping of nano-TiO_2 was proposed.

2. Experimental Section

2.1. Preparation of Nano-TiO_2 Photocatalysts. The preparation process for nano-TiO_2 photocatalysts is shown in Figure 1. First, 100 mL absolute ethanol and 5 mL glacial acetic acid were added to a 250 mL beaker. After magnetic stirring for 30 min, the pH value of the solution was adjusted to 2 using nitric acid. The obtained mixture was designated solution A. Then, 15 mL ethanol and different doses (doping percentage is described as mole ratio) of modifier (Fe^{3+} and/or La^{3+}) were added to a separate beaker to obtain solution B. Solution B was then added to solution A to obtain solution C. Then, 20 mL tetrabutyl titanate was added to the mixed solution C, followed by the addition of 5 mL distilled water. This solution was then stirred for 4 h. Sol TiO_2 was obtained after sealing the container for 2 days. The sol TiO_2 gradually formed nano-TiO_2 upon drying, grinding, and heat treatment.

2.2. Characterization of Photocatalysts. The phase of the as-prepared samples was analyzed using a Shimazu XRD-6000 X-ray diffractometer with a copper target (Cu Kα, λ = 0.15406 nm), a voltage of 40.0 KV, and a current of 30.0 mA.

Surface charge analysis was conducted using a British Kratos XPSAM800 multifunctional surface analysis electron spectrometer, with an Al target (1486.6 ev) X-ray gun operating under 12 kv × 15 ma power. The analysis chamber background vacuum was 2×10^{-7} Pa, adopting FAT working style. The spectrometer was operated with Cu2P3/2 (932.67 ev), Ag3d5 (368.30 ev), and Au4f7/2 (84.00 ev) prototype correction, and data were corrected using carbon pollution Cls (284.8 ev).

The compounds produced in photocatalyzed reactions were identified using UV-Vis absorption spectroscopic analysis. This study used a Shimadzu UV-Vis 2550 spectrophotometer (integrating sphere method) for fixed UV-Vis spectroscopy. A fixed amount of photocatalyst powder was placed in a quartz ware, using standard $BaSO_4$ powder as a reference. Spectra were collected with a sweep rate of 1800 nm/min and a scanning range of 300–650 nm.

The molecular structures of reaction produces were analyzed by fluorescence spectroscopy (FS). This study used solid form testing with a fixed fluorescence intensity at a certain incident light wavelength (275 nm), and the results were combined with the experimentally determined photocatalytic activity to analyze the fluorescent light characteristics of the photocatalysts.
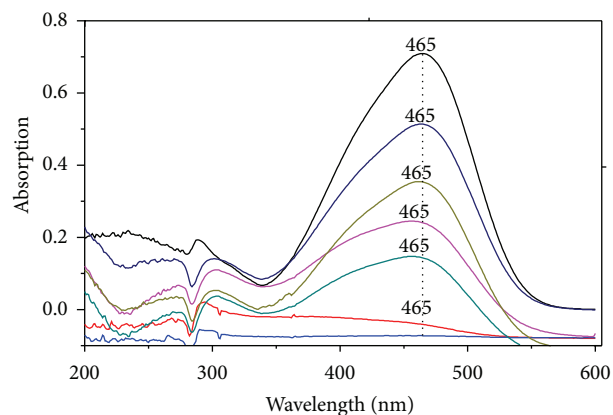
$(CH_3)_2N$——————N = N —————SO_3Na
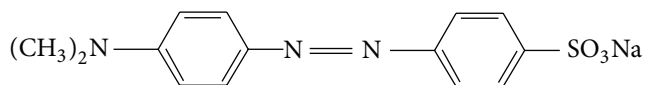
SCHEME 1

FIGURE 1: UV-Vis absorption spectra of methyl orange degradation catalyzed by TiO_2.

2.3. Evaluation of Photocatalyst Activity

2.3.1. Target Compounds. This study used methyl orange (chemical name, dimethylamino azo benzene sulfonic acid sodium), which is produced by nitriding aminobenzene sulfonic acid via N, N-dimethylaniline coupling, as the target compound for assessing photocatalyst activity. The molecular formula of methyl orange is $C_{14}H_{14}O_3N_3SNa$. Its molecular weight is 327.34 Da, and its molecular structural contains a benzene group and N and S heteroatoms as shown in Scheme 1 [24].

Its molecular structure has certain representativeness. Remediation of methyl orange is a widespread problem, because this material is widely used as an industrial dye and is harmful to the aquatic environment. Methyl orange shows obvious absorption of visible light, as its absorbance and concentration have a linear relationship within a certain range, according to the Lambert-Beer law. In the continual degradation process of methyl orange, the maximum absorption wavelength has been at near 465 nm, almost without deviation. The UV-Vis absorption spectra of methyl orange solution undergoing degradation with TiO_2 photocatalyst is shown in Figure 1.

2.3.2. Photocatalytic Reaction Experiment. In a typical photocatalytic experiment, with a 30-W UV lamp and 35-W xenon lamp as light sources, 100 mL methyl orange solution (10 mg/L) and photocatalyst were added to five 300 mL beakers to form separate mixed suspensions. Prior to illumination, these mixed suspensions were stirred using a magnetic stirrer for 30 min. Then, the mixed suspensions were illuminated (the distance from the liquid level to the UV lamp was 10 cm) for 180 min. The mixtures obtained after illumination were separated by centrifugation for 20 min.

2.3.3. Photocatalytic Activity Experiment. The photocatalytic activity of the as-prepared TiO_2 samples was evaluated according to the decolorization rate of methyl orange solution. First, 100 mL methyl orange solution and a specified amount of TiO_2 photocatalyst were placed in a homemade photocatalytic reaction container. After 30 min of magnetic stirring, the reaction mixture was illuminated using the UV lamp and xenon lamp. By measuring the absorbance of the solution at the maximum absorption wavelength of methyl orange ($\lambda_{max} = 465$ nm), the decoloring rate can be calculated as follows:

$$\eta = \frac{A_0 - A_t}{A_0} \times 100\%, \quad (1)$$

where η is the decoloring rate, A_0 is the initial absorbance before illumination, and A_t is the absorbance after illumination time, t.

3. Results and Discussion

3.1. Phase Distribution, Particle Size, and Lattice Distortion of the Prepared Nano-TiO_2 Photocatalysts. Figure 2 shows the XRD spectra for the different types of nano-TiO_2 photocatalyst treated at 500°C for 2 h. Compared to the standard X-ray spectrum of TiO_2, it can be seen that the nano-TiO_2 powders and Fe^{3+}/La^{3+} co-doped nano-TiO_2 powders were anatase phase. As shown in Figure 2, the peak shapes of (101), (004), and (200) crystal plane diffraction was sharp, indicating that anatase phase had completely developed. Due to the small amounts of iron and lanthanide used for doping, no metal oxide diffraction peaks were observed corresponding to Fe^{3+} or La^{3+}. According to previous reports, in the La^{3+}-doped nano-TiO_2, La^{3+} ions on the surface of nano-TiO_2 are oxidized and form a single layer of lanthanide oxide, which is difficult to detect by XRD. According to the solid physical band theory, in the nano-TiO_2 crystal, the ionic radius of Ti^{4+} is 0.074 nm, and the ionic radius of Fe^{3+} is 0.069 nm. Thus, Fe^{3+} can easily spread into the nano-TiO_2 lattice and replace Ti^{4+} in the nano-TiO_2 lattice. The ionic sizes of Fe^{3+} and Ti^{4+} ions are different, leading to nano-scale TiO_2 crystal lattice deformation. Upon La^{3+} doping onto nano-TiO_2, La^{3+} replaces the lattice Ti^{4+}. The ionic radius of La^{3+} is 0.115 nm, which is larger than that of Ti^{4+}. Thus, the substitution of La^{3+} for Ti^{4+} will cause distortion and inflation of the nano-TiO_2 crystal lattice, which will improve the photocatalytic activity of the material.

The size of the nanoscale grain obtained using this formula, that is, the first particle size of oriented crystal growth, cannot reflect particle agglomeration. The calculation results are shown in Table 1.

The calculation results show that the average particle size of Fe^{3+}/La^{3+} codoped nano-TiO_2 was lower than that of pure TiO_2. The particle size of 0.01% $Fe^{3+}/0.6\%$ La^{3+}-doped TiO_2 was the smallest among those tested (6.1 nm). According to the results of photocatalytic degradation of methyl orange solution, the photocatalytic activity of 0.01% $Fe^{3+}/0.6\%$ La^{3+}-doped TiO_2 was the best among the photocatalysts tested. The average grain size of tombarthite-doped TiO_2 was smaller
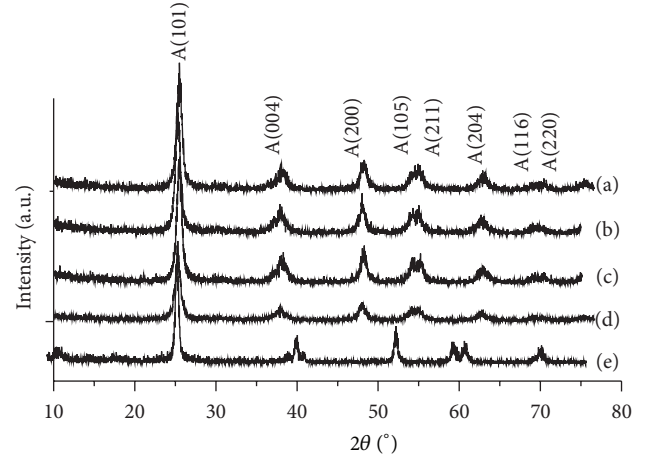

FIGURE 2: XRD spectra of the prepared nano-TiO_2 photocatalysts, (a) La-TiO_2, (b) 0.01% Fe/1.0% La-TiO_2, (c) 0.01% Fe/0.6% La-TiO_2, (d) Fe-TiO_2, and (e) TiO_2.

TABLE 1: XRD analysis results (A: anatase).

Temperature (°C)	Particle size (nm)	Crystal phase
500°C pure TiO_2	20.0	100% A
500°C Fe-TiO_2	8.2	100% A
500°C La-TiO_2	7.4	100% A
500°C 0.01% Fe 0.6La-TiO_2	6.1	100% A
500°C 0.01% Fe/1.0La-TiO_2	7.7	100% A

than that of pure TiO_2, indicating that the mixture of tombarthite ions inhibited the growth of the nanocrystalline phase. The average grain size of nano-TiO_2 codoped with tombarthite ions and transition metal ions was smaller, indicating that doping improved this inhibition.

Doping with metal ions will affect the phase transition temperature, grain size, and other parameters and cause lattice distortion. Fe^{3+} partly replaced lattice Ti^{4+}, inevitably causing oxygen defects, and the existence of oxygen vacancies is thought to promote grain growth of the rutile phase. Therefore, Fe^{3+} doping has a beneficial effect on the transformation of nano-TiO_2 from anatase to rutile type. Doping with La^{3+} can inhibit the transformation of TiO_2 from anatase to rutile and thereby increase the content of the highly photocatalytic anatase phase, causing the grain size of nano-TiO_2 to decrease and thus the quantization effect to increase. Therefore, the synergistic effect of codoping with Fe^{3+} and La^{3+} makes the photocatalyst activity higher than the sum of the activities with single ion doping. According to Figure 2, upon doping with a small amount of Fe^{3+} and La^{3+}, the diffraction peaks of nano-TiO_2 shift towards the low angle direction, indicating that the diffraction peaks of Fe^{3+}/La^{3+} codoped nano-TiO_2 catalyst are wider than those of pure TiO_2. Compared with pure nano-TiO_2, the particle size of doped nano-TiO_2 was reduced. This is because a certain amount Fe^{3+} and La^{3+} penetrates the nano-TiO_2 crystal lattice, restricting the transfer and rearrangement of Ti and
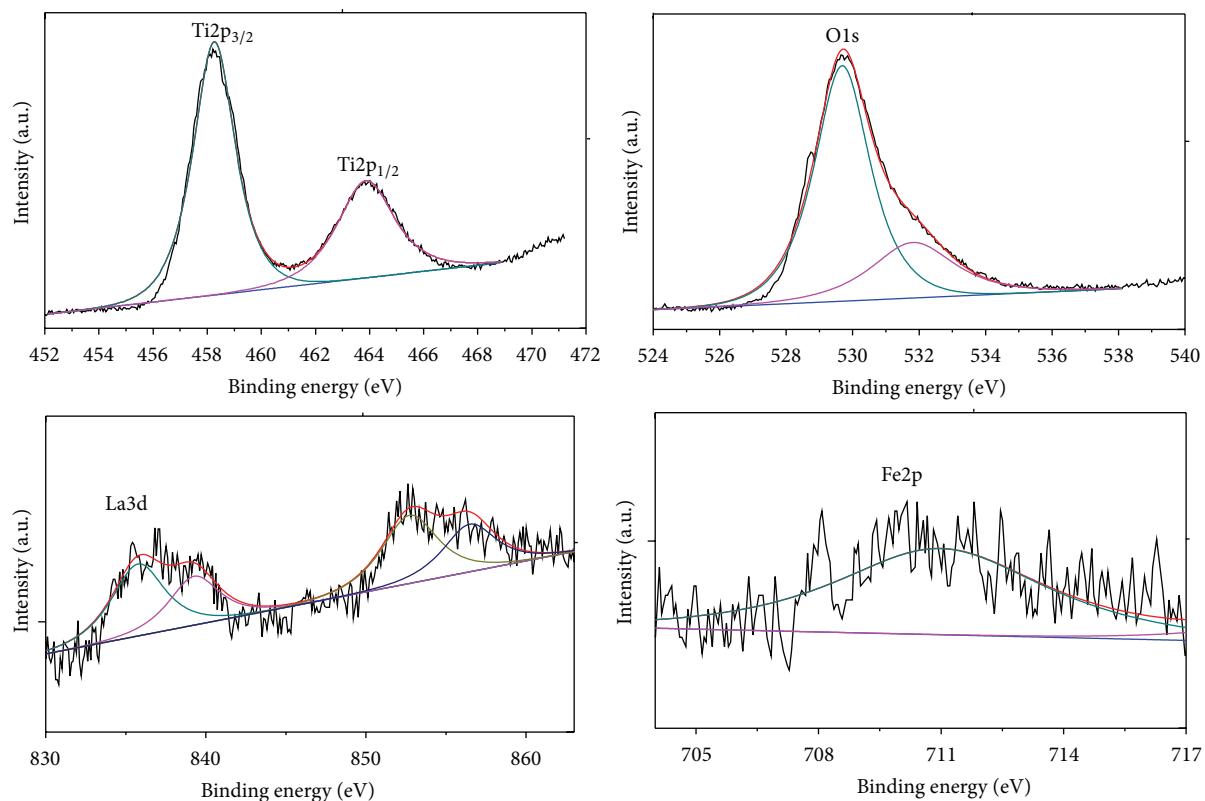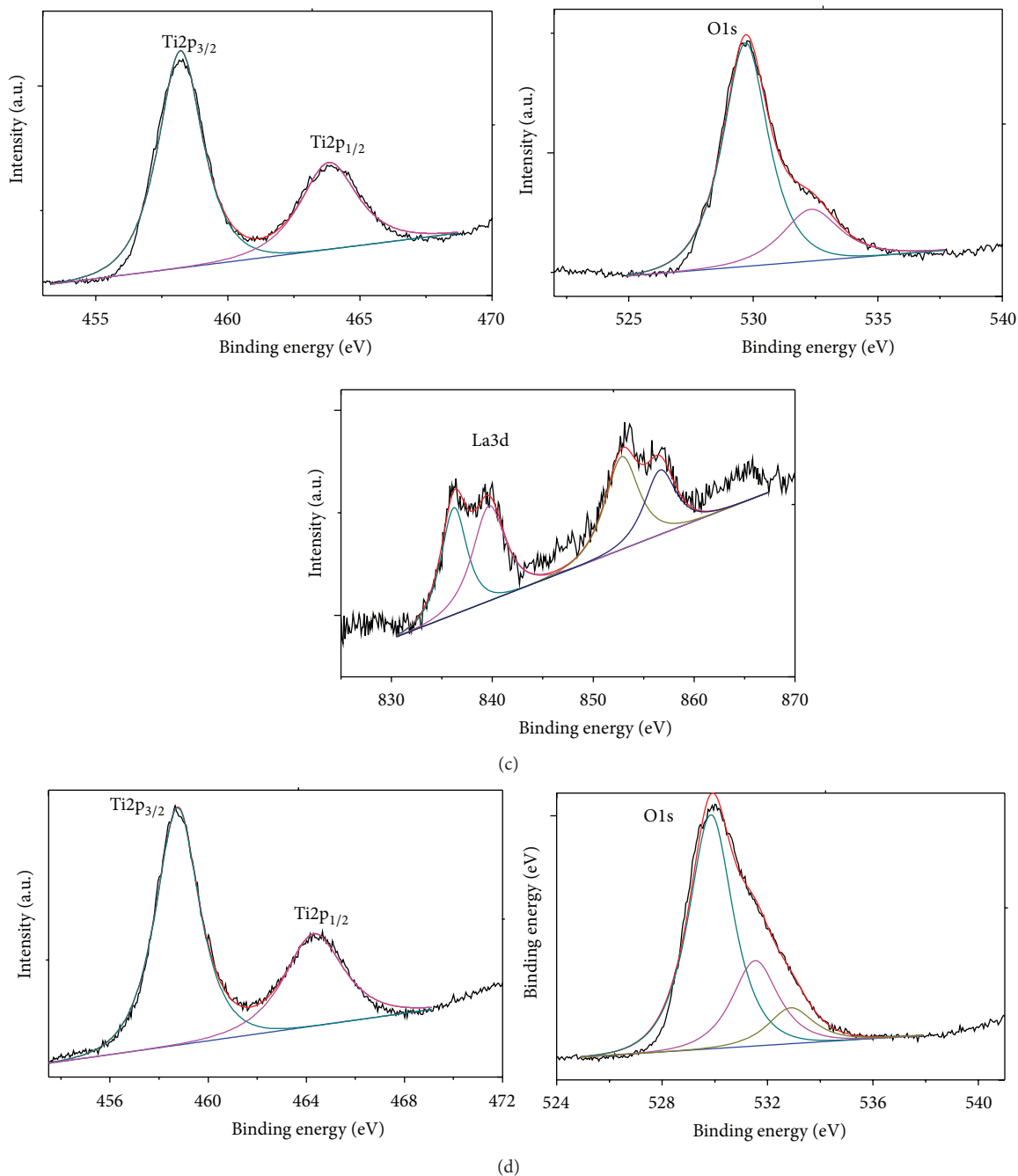
(a)
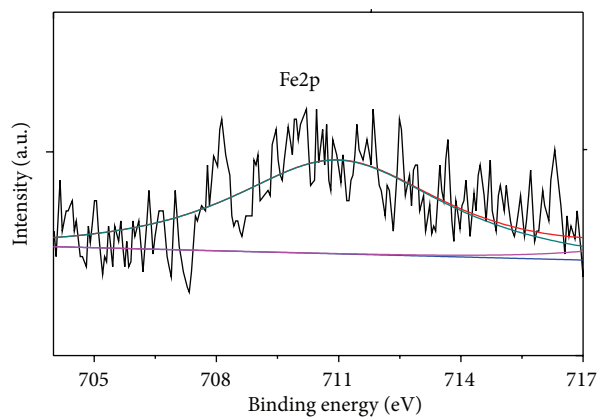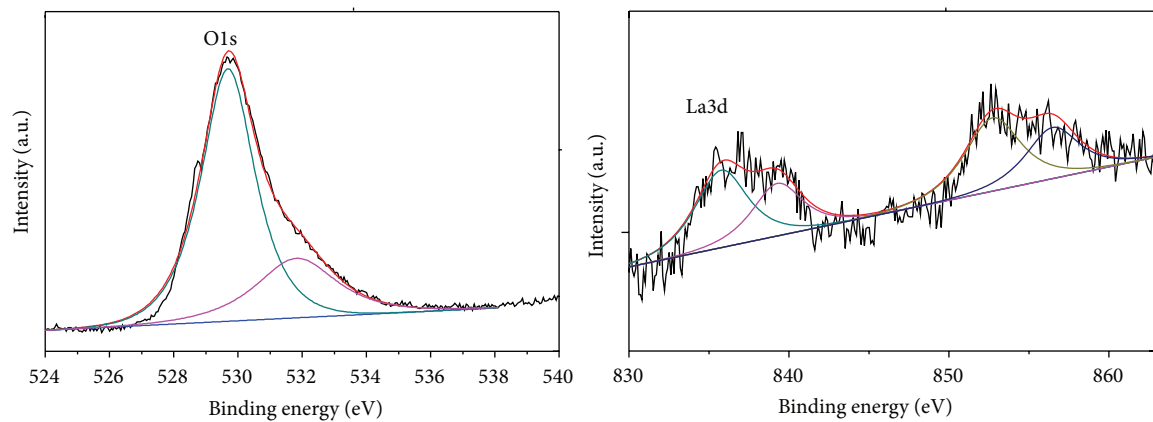
(b)

Figure 3: Continued.

(c)

(d)

FIGURE 3: XPS spectra for different elements in (a) 0.01% Fe^{3+}/0.6% La^{3+} codoped nano-TiO_2, (b) 0.01% Fe^{3+} doped TiO_2, (c) 0.6% La^{3+} doped TiO_2, and (d) TiO_2.

O ions, inhibiting the growth of nano-TiO_2 crystals and decreasing the particle size.

3.2. Elemental Analysis of the Prepared Nano-TiO_2 Photocatalyst.
Figures 3(a), 8(b), and 8(c) show the XPS spectra of different elements in 0.01% Fe^{3+}/0.6% La^{3+} codoped nano-TiO_2, 0.01% Fe^{3+} doped TiO_2, and 0.6% La^{3+} doped TiO_2, respectively. Figure 3(d) shows XPS spectrum of different elements in TiO_2. According to the high-resolution XPS patterns

of Ti2p in these four spectra, there are two characteristic peaks of the same type at 463 eV and 458 eV. These two peaks correspond to the absorption peaks of $Ti2p_{1/2}$ and $Ti2p_{2/3}$ in anatase type TiO_2, respectively, indicating that elemental Ti exists in the form of Ti^{4+} and the titanium oxide bond is stable. In Fe^{3+} doped nano-TiO_2, the combining capacities of $Ti2p_{2/3}$ and $Ti2p_{1/2}$ are 458.28 eV and 463.90 eV, respectively. In 0.6% La^{3+} doped nano-TiO_2, the combining capacities of $Ti2p_{2/3}$ and $Ti2p_{1/2}$ are 458.20 eV and 463.82 eV,

respectively. In 0.01% Fe^{3+}/0.6% La^{3+} doped nano-TiO_2, the combining capacities of $Ti2p_{2/3}$ and $Ti2p_{1/2}$ are 458.25 eV and 463.88 eV, respectively. The values of combining capacity of these samples are different from those of pure TiO_2 (combining capacities of $Ti2p_{2/3}$ and $Ti2p_{1/2}$ equal to 458.74 eV and 463.31 eV, resp.). This is due to doping with Fe^{3+} and La^{3+}. In the Fe^{3+}/La^{3+} codoped TiO_2, these two peaks shift 0.5 eV toward the higher energy direction, indicating that the effective positive charge of Ti was increased. Upon doping with elemental Fe and La, on the surface or in the lattice of nano-TiO_2, electronic redistribution occurs and leads to a decrease in the Ti outer electron density, a reduction in the shielding effect, and an increase in the electron binding energy. These effects are beneficial for increasing photocatalytic activity. The binding energy difference between catalyst Ti2p and O1s is 71.3 eV, which indicates that Ti in the three prepared catalysts is in the tetravalent form (TiO_2).

According to Figures 3(a)–3(c), the peaks at 529.6–529.8 eV in the O1s high-resolution XPS patterns are mostly related to Ti, and the surface hydroxyl or oxygen in oxide defects is the key. Hydroxyl groups on the surface of the catalyst are considered to be an important factor affecting photocatalytic activity. A hydroxyl group on the nano-TiO_2 catalyst surface can capture light and generate an ·OH free radical, which has strong oxidation ability. The ·OH free radical is the main strong oxidizer in the photocatalytic reaction. Therefore, as the hydroxyl content on the surface of nano-TiO_2 catalyst increases, the surface becomes more conducive to the generation of ·OH free radicals and the quantization efficiency is further improved, thereby effectively improving the catalytic activity of the nano-TiO_2 catalyst.

According to Figures 3(a) and 8(b), in the Fe2p high-resolution XPS patterns for 0.01% Fe^{3+} doped nano-TiO_2 and 0.01% Fe^{3+}/0.6% La^{3+} doped nano-TiO_2, Fe2p peaks appear at 710.68 eV and 710.98 eV. This is trivalent iron, indicating that iron doped on TiO_2 is in the form of Fe_2O_3. In addition, as shown in Figure 3(c), no Fe2p peak appears in the TiO_2 XPS spectrum, indicating that elemental Fe exists only in crystalline Fe^{3+}/La^{3+} doped nano-TiO_2. Elemental Fe in the three prepared catalysts is in the tetravalent form.

According to Figures 3(a) and 3(c), in the La3d high-resolution XPS patterns of 0.6% La^{3+} doped nano-TiO_2 and 0.01% Fe^{3+}/0.6% La^{3+} doped nano-TiO_2, La3d peaks appear at 835.75 eV and 836.20 eV. In Figure 3(d), no La3d peaks appear in the TiO_2 XPS spectrum at these positions, confirming that elemental La was present only in La^{3+} doped nano-TiO_2 and Fe^{3+}/La^{3+} codoped nano-TiO_2 powders. The difference in the binding energies of La^{3+} doped nano-TiO_2 and Fe^{3+}/La^{3+} codoped nano-TiO_2 is 0.5 eV. This suggests that La^{3+} doping changed the electronic distribution on the nano-TiO_2 surface or lattice, thus improving photocatalytic performance. In the La3d spectrum, two peaks appear for $La3d_{3/2}$ and $La3d_{5/2}$. According to previous reports, La exists in the form of La_2O_3 [25, 26]. Thus, La^{3+} ions did not enter into the lattice of TiO_2. This is because the ionic radius of La^{3+} ions is bigger than that of Ti^{4+} ions, and thus, La^{3+} ions cannot enter into the lattice of TiO_2.

3.3. FS Analysis of the Prepared Nano-TiO_2 Photocatalyst.
Figure 4 shows the fluorescence spectra of TiO_2 and the three prepared nano-TiO_2 photocatalysts. According to Figure 4(a)(A–D), the fluorescence spectra for Fe^{3+}/La^{3+} codoped nano-TiO_2 and pure TiO_2 have a fluorescence peak at 417 nm. The intensity of this peak for Fe^{3+}/La^{3+} codoped nano-TiO_2 is lower than that in the spectra for nano-TiO_2 doped with either metal or pure TiO_2. Combined with the experimental results for methyl orange solution decolorization, this decrease in fluorescence intensity indicates a reduced recombination rate of photo-produced electron-hole pairs, and thus, an increased photocatalytic activity. The above results show that the improvement in visible light catalytic activity is due to the reduction of the light carrier recombination rate by doping.

Figure 4(b) shows the fluorescence spectra of nano-TiO_2 doped with different amounts of La^{3+}. Figure 4(c) shows the fluorescence spectra of nano-TiO_2 doped with different amounts of Fe^{3+}. Figure 4(d) shows the fluorescence spectra of nano-TiO_2 doped with different amounts of Fe^{3+} and La^{3+}. According to these spectra, TiO_2 shows a strong peak at 417 nm, and the position of this peak is not affected by doping of the nano-TiO_2 with any amount of Fe^{3+} and/or La^{3+}. The intensity of this peak is weaker in the spectra for Fe^{3+}/La^{3+} codoped nano-TiO_2. La and Fe exist in the form of La_2O_3 and Fe_2O_3, respectively, and these metal oxides can function as agents to capture photo-produced electrons. After capture of a photo-produced electron, it is difficult for the electron to recombine with a hole. Together with the results of the methyl orange decolorization experiments, these results showing that the fluorescence intensity of codoped samples is smaller indicate that their photocatalytic activity is better. Codoping with Fe^{3+} and La^{3+} reduces the recombination rate of photo-produced electron-hole pair and improves the quantum efficiency, thus leading to improvement in the photocatalytic efficiency.

3.4. UV-Vis Analysis.
Figure 5(a) shows UV-Vis absorption spectra of nano-TiO_2 doped with different amounts of Fe^{3+}. Relative to the absorption spectra of pure TiO_2, the absorption band edge of Fe^{3+} doped nano-TiO_2 shows an obvious red-shift. The obviously enhanced absorption strength in the visible area is beneficial for improving the utilization of sunlight and the photocatalytic efficiency. The main reason for this improvement is that the radius of Fe^{3+} (0.064 nm) is similar to that of Ti^{4+} (0.068 nm), and thus, Fe^{3+} can replace some Ti^{4+} in the lattice and create lattice defects. Impurity level formed in nano-TiO_2 band gap, and the energy of semiconductor optical electronic transiting to guide reduced, smaller energy photoproduction electronic can also transit, so the spectrum redshift, light response range extended.

Figure 5(b) shows the UV-Vis absorption spectra of nano-TiO_2 doped with different amounts of La^{3+}. The absorption sideband of La^{3+} doped nano-TiO_2 moved towards the longer wavelengths, and the absorption rate of light increased. This is because the radius of La^{3+} is 0.115 nm, which is larger than that of Ti^{4+} (0.068 nm). Thus, La^{3+} has difficultly entering the
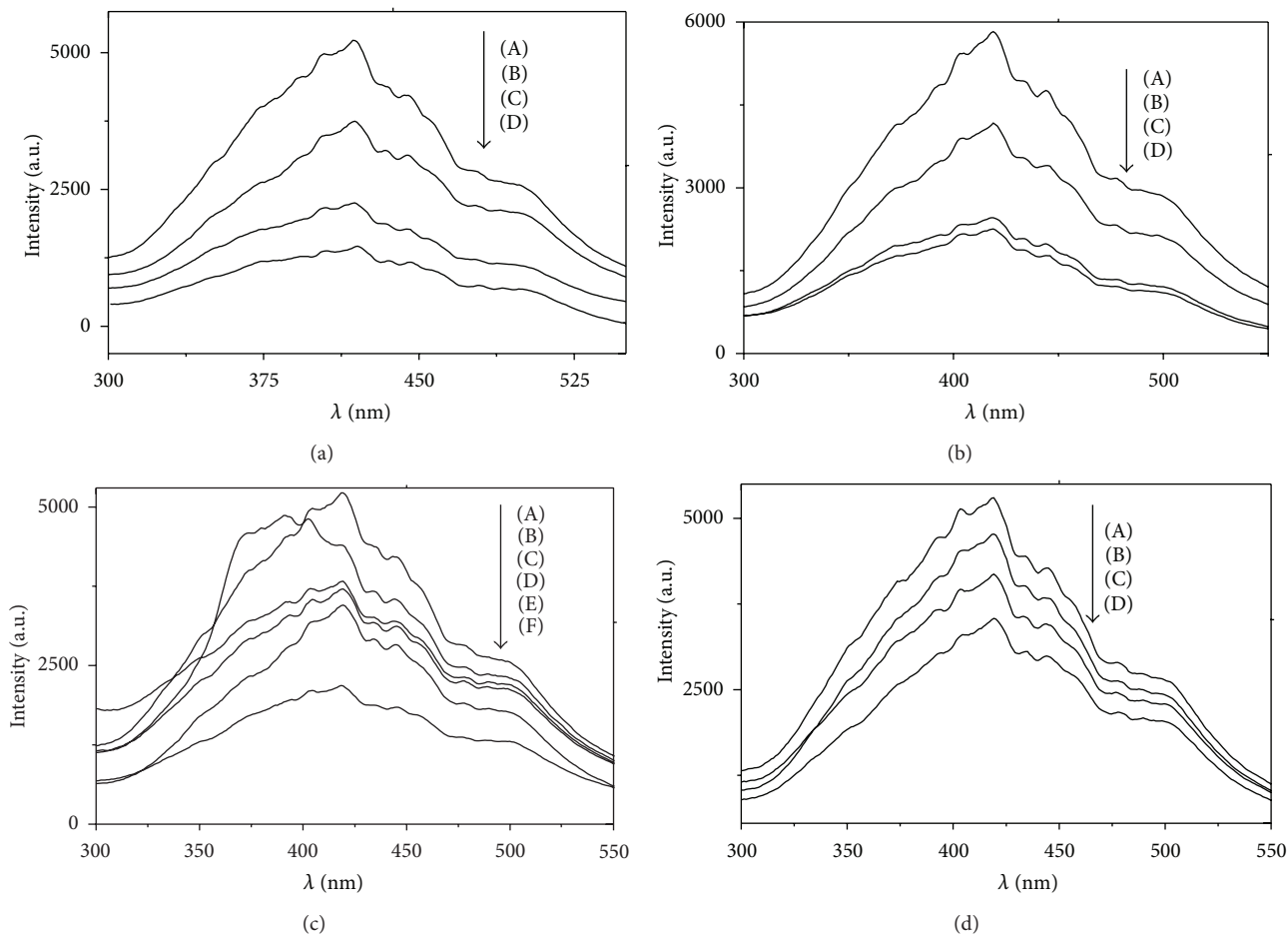
FIGURE 4: (a) Fluorescence spectra of (A) TiO_2, (B) 0.01% Fe^{3+} doped nano-TiO_2, (C) 0.6% La^{3+} doped nano-TiO_2, and (D) 0.01% Fe^{3+}/0.6% La^{3+} codoped nano-TiO_2; (b) fluorescence spectra of (A) 1.5% La^{3+}, (B) 1.0% La^{3+}, (C) 0.3% La^{3+}, and (D) 0.6% La^{3+} doped nano-TiO_2, (c) fluorescence spectra of (A) 0.005% Fe^{3+}, (B) 0.1% Fe^{3+}, (C) 0.05% Fe^{3+}, (D) 0.2% Fe^{3+}, (E) 0.15% Fe^{3+}, and (F) 0.01% Fe^{3+} doped nano-TiO_2; (d) fluorescence spectra of nano-TiO_2 codoped with (A) 0.15% Fe^{3+} and 0.6 % La^{3+}, (B) 0.01% Fe^{3+} and 1.0% La^{3+}, (C) 0.01% Fe^{3+} and 0.5% La^{3+}, and (D) 0.01% Fe^{3+} and 0.6% La^{3+}.
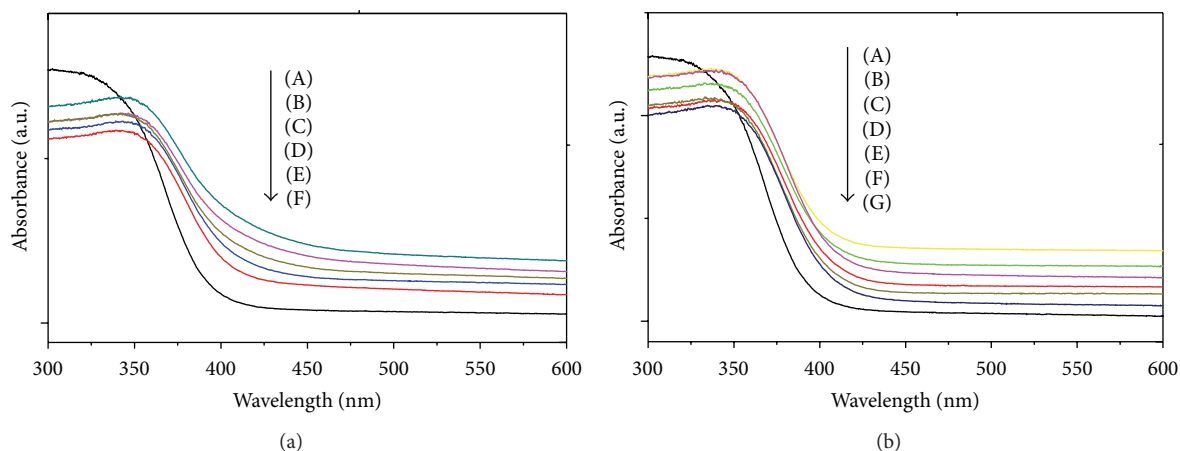

FIGURE 5: (a) UV-Vis absorption spectra of nano-TiO_2 doped with (A) 0.1% Fe^{3+}, (B) 0.15% Fe^{3+}, (C) 0.2% Fe^{3+}, (D) 0.05% Fe^{3+}, and (E) 0.01% Fe^{3+}, and (F) pure TiO_2; (b) UV-Vis absorption spectra of nano-TiO_2 doped with (A) 0.6% La^{3+}, (B) 0.5% La^{3+}, (C) 0.7% La^{3+}, (D) 0.3% La^{3+}, (E) 1.0% La^{3+}, (F) 1.5% La^{3+}, and (G) pure TiO_2.
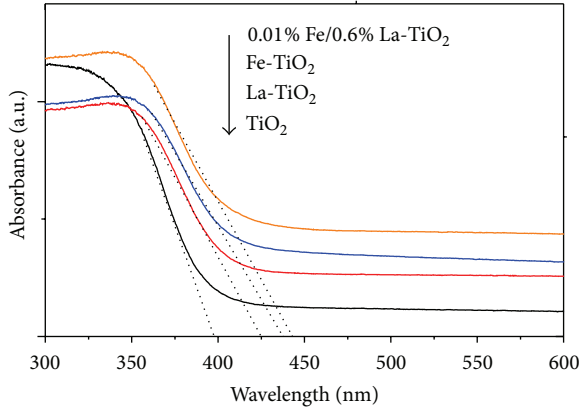
FIGURE 6: UV-Vis absorption spectra for nano-TiO_2.

lattice of nano-TiO_2. When the quantity of doped La was very small, La covered the surface of nano-TiO_2 mainly in its oxide form, hindering grain growth. This led to the particles of La-doped nano-TiO_2 being smaller than those of nondoped nano-TiO_2. The tombarthite elements covering the surface of nano-TiO_2 particles can absorb light over a wide range and transfer the energy to the nano-TiO_2, thus improving the photocatalytic reactivity.

Figure 6 shows the UV-Vis absorption spectra for single- and codoped nano-TiO_2 photocatalysts. The absorption bands for these nano-TiO_2 catalysts shifted to the visible light region at varying degrees. For catalyst doped with La^{3+} and Fe^{3+} individually, the absorption edge moved 35 nm and 41 nm toward the visible light region, respectively. That for nano-TiO_2 photocatalyst codoped with 0.01% Fe^{3+} and 0.6% La^{3+} moved 49 nm toward the visible light region. Therefore, the absorption sideband of Fe/La codoped nano-TiO_2 red-shifted more than that for the Fe^{3+} or La^{3+} single-doped nano-TiO_2, and the absorption of visible light by the codoped catalyst is stronger than that by the single-doped catalysts. This indicated that the codoping with both elements has a synergistic effect. The main reasons are as follows: the 3d orbital of Fe^{3+} is above the valence band of nano-TiO_2. Electrons on the 3d orbital can absorb 415 nm visible light and transit it to nano-TiO_2 to create Fe^{4+}, and thus, Fe^{3+} acts as an electron trap. The vacant 5d orbital of La^{3+} serves as a good electron transfer orbital. This orbital can be used to transfer the photo-produced electrons in the TiO_2 photocatalytic reaction, and thus, La^{3+} also acts as an electron trap. Therefore, codoping with Fe^{3+} and La^{3+} inhibited recombination of photo-produced electrons and holes, and thereby improved the quantum efficiency of photo-production.

3.5. Influence of Doping Amount on the Photocatalytic Activity of Nano-TiO_2

3.5.1. Influence of Doping with Fe^{3+} or La^{3+} on the Photocatalytic Activity of Nano-TiO_2. Figure 7(a) demonstrates the influence of Fe^{3+} doping concentration on the photocatalytic

activity of nano-TiO_2. According to Figure 7(a), the optimum doping amount of Fe^{3+} is 0.01%, which gives methyl orange decolorization rates of 93.5% with 3 h of UV illumination (versus 56.88% for pure TiO_2) and 29.8% with 5 h of visible light illumination (versus 4.2% for pure TiO_2). Doping with Fe^{3+} causes the nano-TiO_2 to not only be able to capture electrons, but also to capture holes and the carrier is easily released. Thus, doping with Fe^{3+} can increase the photocatalytic activity of the nano-TiO_2 catalyst. Doping with a small amount of Fe^{3+} can reduce the recombination rate of electrons and holes and enhance the photocatalytic activity of nano-TiO_2 in the visible region, by improving the visible light utilization efficiency. At a low doping concentration, Fe^{3+} can play a dual role as an electron and a hole trap, and thereby improve the photocatalytic activity of the catalyst. At a high doping concentration, Fe^{3+} can reduce the quantum efficiency of photo-produced electrons and holes, leading to a decrease in the photocatalytic activity of the catalyst. This also can explain the influence of the doping amount on the photocatalytic activity via the process of capturing electrons and holes crossing the barrier. The recombination rate depends on the distance, R, of separation between the electron and hole [27]:

$$K_{composite} \propto \exp\left(-\frac{2R}{\alpha_0}\right), \tag{2}$$

where $K_{composite}$ is the recombination rate constant, α_0 is the capture carrier hydrogen-like wave equation, and R is the distance of separation between the electron and hole.

According to the formula above, when the doping concentration is less than the optimum value, the semiconductor does not have enough traps to catch carriers. When the doping concentration is larger than the optimum value, due to the reduction in the average distance between the electrons and traps, the recombination rate K grows exponentially as the doping concentration is increased. Thus, use of the optimum doping amount of transition metal ions is critical.

Figure 7(b) shows the influence of La^{3+} doping concentration on the photocatalytic activity of nano-TiO_2. As shown in Figure 7(b), doping with tombarthite element La^{3+} improved the photocatalytic activity of nano-TiO_2. The methyl orange degradation rate under visible light illumination is greatly improved by La doping. The methyl orange decolorization rate increased as the doping amount of La^{3+} increased. The highest photocatalytic activity was observed for a doping concentration of La^{3+} of 0.6%. The methyl orange decolorization rate was 88.1% with 3 h of UV irradiation (pure TiO_2) and 27.4% with 5 h of visible light irradiation (versus 4.2% for pure TiO_2). With greater doping amounts, the photocatalytic activity did not continue to increase, but instead decreased. Doping with La ions increased catalytic activity, because tombarthite elements can produce electron configuration, polycrystalline type, and thermal stability. Doping with the appropriate amount of a tombarthite element has a positive role in improving the crystal type and photocatalytic properties of nano-TiO_2. Because the La^{3+} radius is 0.106 nm, which is different from that of Ti^{4+} (0.068 nm), doping with La ions caused an increase in oxygen vacancy and defects on the
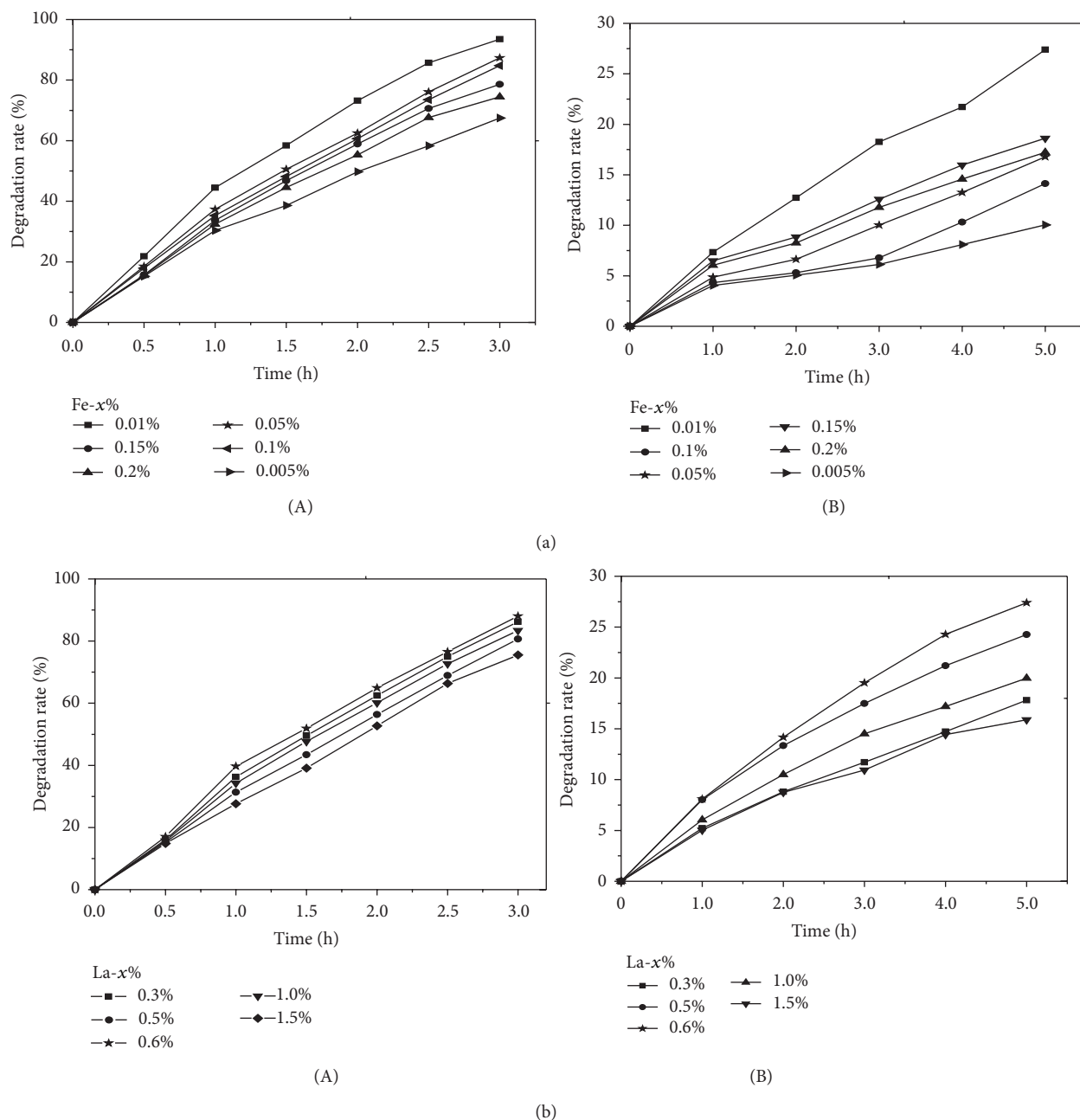
FIGURE 7: (a) Influence of Fe^{3+} doping concentration on photocatalytic activity of TiO_2, (A) UV irradiation, (B) visible light irradiation; (b) influence of La^{3+} doping on the photocatalytic activity of nano-TiO_2, (A) UV irradiation, (B) visible light irradiation.

surface of the nano-TiO_2, effectively inhibiting the nano-TiO_2 photo-production of electron-hole pairs, thereby improving the photocatalytic activity. However, too much tombarthite element also may cause a free electron transfer center to become a free electron recombination center and increase the photo-production of electron-hole pairs, thus reducing the photocatalytic activity.

The f orbital of tombarthite elements can have a coordination effect with the degradation substrate, and doping with a certain amount of La ions can effectively separate the nano-TiO_2 photo-produced electrons and holes, generating many active groups with strong oxidizing ability involved in the

photocatalytic oxidation reduction reaction, thereby improving the photocatalytic activity of the catalyst. However, when the doping amount exceeds a certain concentration, too much tombarthite metal ion deposition on the surface of nano-TiO_2 hinders electron and hole transfer from the surface of the catalyst. Thus, tombarthite metal ions on the surface of the nano-TiO_2 become charge carrier recombination centers, resulting in a decrease in catalytic activity.

3.6. The Influence of Fe^{3+}/La^{3+} Codoping on Nano-TiO_2 Photocatalytic Activity. Figure 8 shows the influence of
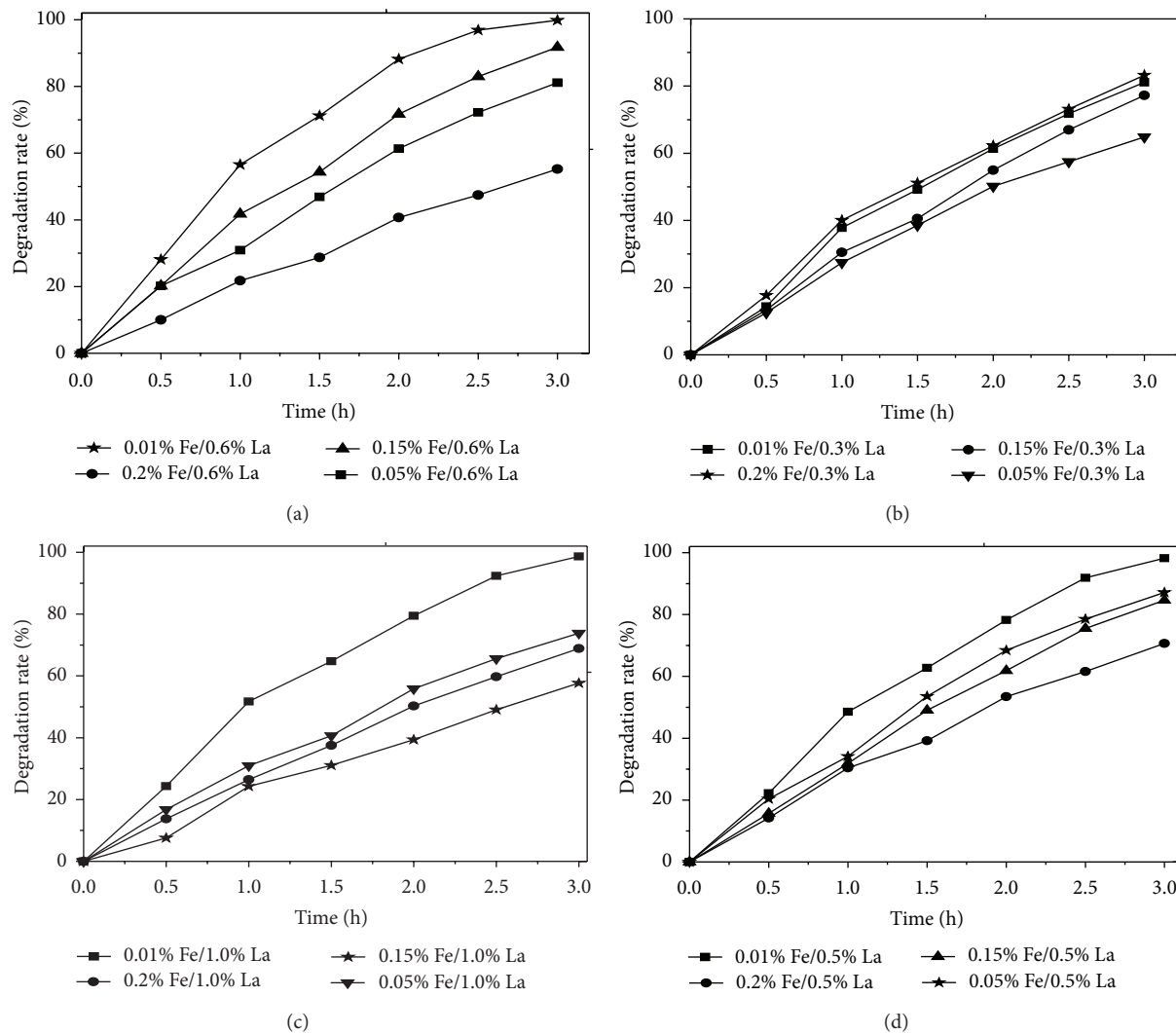
FIGURE 8: Effect of Fe/La codoping on the photocatalytic activity of nano-TiO$_2$ under UV light irradiation.

Fe^{3+}/La^{3+} codoping on the photocatalytic activity of nano-TiO$_2$ under UV illumination, and Figure 9(a) shows the effect of Fe^{3+}/La^{3+} codoping on the photocatalytic activity of nano-TiO$_2$ under visible light illumination. According to the results shown in these figures, the catalytic activity of codoped nano-TiO$_2$ is higher than that of catalyst doped with either Fe^{3+} or La^{3+}. The 0.01% Fe^{3+} and 0.6% La^{3+} codoped nano-TiO$_2$ possessed the highest photocatalytic activity. After 3 h of UV irradiation, the decolorization rate of methyl orange for 0.01% Fe^{3+} and 0.6% La^{3+} codoped nano-TiO$_2$ was 99.8%. After 5 h of visible light irradiation, the decolorization rate of methyl orange for 0.01% Fe^{3+} and 0.6% La^{3+} codoped nano-TiO$_2$ was 40.7%. Both of these rates are greatly improved over those achieved by pure TiO$_2$. Doping with transition metal Fe^{3+} ions alone did not hinder the modification of tombarthite ions, but worked together with tombarthite La^{3+} ions to further improve the activity of the photocatalyst.

The experimental results show that there are optimum doping amounts for both Fe^{3+} and La^{3+}. A high concentration of doping ions can reduce the photocatalytic activity. Under the conditions of high concentrations, neither Fe^{3+} nor La^{3+} can effectively penetrate the crystal lattice of nano-TiO$_2$, and therefore, these ions gather on the surface of crystals. An excessive of doping ions can catch large numbers of electrons and holes, reduce the quantum efficiency, and reduce the activity of catalysts. For low doping concentration, an increase in the doping ion concentration can improve the optical carrier separation effect. Therefore, because the thickness of the space between electrons and the surface of nano-TiO$_2$ decreases with an increasing amount of doping tombarthite element, when the optimum concentration of doping metal is reached, the distance between the electrons and the surface is equal to the penetration depth of incident light into the solid and photoproduction of electrons and holes is achieved by optimal light irradiation, benefiting the photocatalytic reaction. The combined effects of Fe^{3+} and La^{3+} upon codoping of nano-TiO$_2$ photocatalyst promoted the optimum separation of photoproduced electrons and
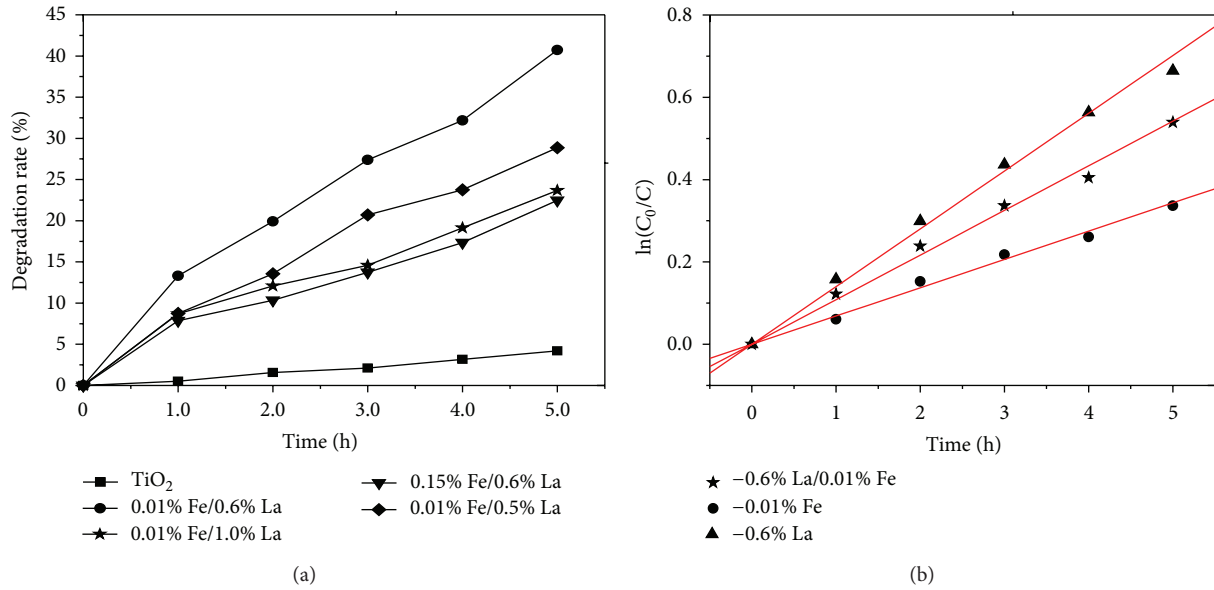
FIGURE 9: (a) Effect of Fe/La codoping on the photocatalytic activity of nano-TiO$_2$ under visible light irradiation; (b) relationship between ln(C_0/C) and photocatalysis time for the different doped nano-TiO$_2$ catalysts.

holes and thus improved the photocatalytic activity of the photocatalyst.

3.7. Kinetics of the Photocatalytic Activity of Codoped Nano-TiO$_2$. For a heterogeneous photocatalytic system, such as the nano-TiO$_2$ photocatalytic system, the reaction rate of photocatalytic oxidation can be described by the Langmuir-Hinshelwood dynamics equation as follows [28]:

$$-\frac{dC}{dt} = \frac{kKC}{1 + KC}, \tag{3}$$

where C is the concentration of reactant, k is the activity constant, and K is the adsorption equilibrium constant of the reaction. Integration of (3) gives

$$t = \frac{1}{Kk} \ln \frac{C_0}{C} + \frac{1}{k}(C_0 - C). \tag{4}$$

When the concentration C is small, (4) can be transformed into

$$\ln \frac{C_0}{C} = k't + A, \tag{5}$$

where k' is the apparent rate constant and A is a constant.

The kinetics for the degradation of methyl orange by the different prepared nano-TiO$_2$ photocatalysts were investigated in the present study. The relationship between ln(C_0/C) (C_0 is the initial concentration and C is the concentration at time t) and photocatalysis time t is shown in Figure 9(b). The fitting of the data for the photocatalytic degradation of methyl orange with a first-order kinetic curve is shown in Table 2.

According to Table 2, the P value for the fitted straight line is far less than 0.01, indicating that ln(C_0/C) and t are significantly linearly correlated. As shown in Figure 9, under visible light irradiation, the degradation of methyl orange by different doped nano-TiO$_2$ catalysts is well described by first-order reaction kinetics. The high correlation coefficients indicate that this model can be used to describe this photodegradation reaction.

4. Conclusions

In the present study, nano-TiO$_2$ powder photocatalyst was prepared and modified via a sol-gel method by doping with either Fe^{3+} or La^{3+} individually or codoping with both Fe^{3+} and La^{3+}. Codoping of nano-TiO$_2$ photocatalysts with both Fe^{3+} and La^{3+} resulted in better catalytic performance than that achieved by doping with either Fe^{3+} or La^{3+}, as well as better inhibition of nanocrystal growth and better refinement of grain size. Doping with tombarthite ions can effectively inhibit the shift of nano-TiO$_2$ from anatase to rutile. La^{3+} doping changed the nano-TiO$_2$ surface or lattice electron distribution. The sol-gel method can be used to effectively dope the lattice of nano-TiO$_2$ with Fe^{3+} and La^{3+}. Compared with catalyst doped with only Fe^{3+} or La^{3+}, the light absorption intensity of Fe^{3+}/La^{3+} codoped nano-TiO$_2$ photocatalyst was stronger. This is because the absorption band edge redshifted obviously, and the spectral response range was extended into the visible light region, increasing the utilization of visible light. Fe^{3+}/La^{3+} codoped nano-TiO$_2$ photocatalyst showed superior photocatalytic performance compared to the single-doped samples. Because nano-TiO$_2$ codoped with two elements can achieve higher catalytic activity under visible light, this approach increases the potential utility of nano-TiO$_2$ photocatalyst materials in important environmental purification processes.

TABLE 2: Results of first-order kinetic fitting of the data for methyl orange degradation under visible light irradiation with the different doped nano-TiO_2 catalysts.

Photocatalyst	Kr	R	SD	N	P
0.6% La-TiO_2	0.1336	0.9977	0.0189	6	<0.0001
0.01% Fe-TiO_2	0.0671	0.9961	0.0125	6	<0.0001
0.6% La 0.01% Fe-TiO_2	0.1041	0.9967	0.0177	6	<0.0001

Conflict of Interests

The authors declare no conflict of interests.

References

[1] A. L. Giraldo, G. A. Peñuela, R. A. Torres-Palma, N. J. Pino, R. A. Palominos, and H. D. Mansilla, "Degradation of the antibiotic oxolinic acid by photocatalysis with TiO_2 in suspension," *Water Research*, vol. 44, no. 18, pp. 5158–5167, 2010.

[2] L. Rizzo, A. D. Sala, A. Fiorentino, and G. Li Puma, "Disinfection of urban wastewater by solar driven and UV lamp—TiO_2 photocatalysis: effect on a multi drug resistant *Escherichia coli* strain," *Water Research*, vol. 53, pp. 145–152, 2014.

[3] H. Tong, S. Ouyang, Y. P. Bi, N. Umezawa, M. Oshikiri, and J. H. Ye, "Nano-photocatalytic materials: possibilities and challenges," *Advanced Materials*, vol. 24, no. 2, pp. 229–251, 2012.

[4] C. E. Barrera-Díaz, V. Lugo-Lugo, and B. Bilyeu, "A review of chemical, electrochemical and biological methods for aqueous Cr(VI) reduction," *Journal of Hazardous Materials*, vol. 223-224, pp. 1–12, 2012.

[5] V. K. Gupta, "Application of low-cost adsorbents for dye removal—a review," *Journal of Environmental Management*, vol. 90, no. 8, pp. 2313–2342, 2009.

[6] I. Nandi, P. Mitra, P. Banerjee, A. Chakrabarti, M. Ghosh, and S. Chakrabarti, "Ecotoxicological impact of sunlight assisted photoreduction of hexavalent chromium present in wastewater with zinc oxide nanoparticles on common *Anabaena flosaquae*," *Ecotoxicology and Environmental Safety*, vol. 86, pp. 7–12, 2012.

[7] Y. M. Tzou, S. L. Wang, and M. K. Wang, "Fluorescent light induced Cr(VI) reduction by citrate in the presence of TiO_2 and ferric ions," *Colloids and Surfaces A: Physicochemical and Engineering Aspects*, vol. 253, no. 1–3, pp. 15–22, 2005.

[8] L. Liu, Z. Ji, W. Zou et al., "In situ loading transition metal oxide clusters on TiO_2 nanosheets as co-catalysts for exceptional high photoactivity," *ACS Catalysis*, vol. 3, no. 9, pp. 2052–2061, 2013.

[9] M. A. Barakat, "New trends in removing heavy metals from industrial wastewater," *Arabian Journal of Chemistry*, vol. 4, no. 4, pp. 361–377, 2011.

[10] P. S. Suchithra, C. P. Shadiya, A. P. Mohamed, P. Velusamy, and S. Ananthakumar, "One-pot microwave mediated growth of heterostructured ZnO@AlSi as a potential dual-function eco-catalyst for treating hazardous pollutants in water resources," *Applied Catalysis B: Environmental*, vol. 130-131, pp. 44–53, 2013.

[11] V. V. Guliants, M. A. Carreon, and Y. S. Lin, "Ordered mesoporous and macroporous inorganic films and membranes," *Journal of Membrane Science*, vol. 235, no. 1-2, pp. 53–72, 2004.

[12] A. Idris, E. Misran, and N. Mohd Yusof, "Photocatalytic reduction of Cr(VI) by PVA-alginate encapsulated γFe_2O_3 magnetic beads using different types of illumination lamp and light," *Journal of Industrial and Engineering Chemistry*, vol. 18, no. 6, pp. 2151–2156, 2012.

[13] R. Gherbi, N. Nasrallah, A. Amrane, R. Maachi, and M. Trari, "Photocatalytic reduction of Cr(VI) on the new hetero-system $CuAl_2O_4/TiO_2$," *Journal of Hazardous Materials*, vol. 186, no. 2-3, pp. 1124–1130, 2011.

[14] D. P. Das, K. Parida, and B. R. De, "Photocatalytic reduction of hexavalent chromium in aqueous solution over titania pillared zirconium phosphate and titanium phosphate under solar radiation," *Journal of Molecular Catalysis A: Chemical*, vol. 245, no. 1-2, pp. 217–224, 2006.

[15] K. M. Parida, S. S. Dash, and D. P. Das, "Physico-chemical characterization and photocatalytic activity of zinc oxide prepared by various methods," *Journal of Colloid and Interface Science*, vol. 298, no. 2, pp. 787–793, 2006.

[16] J. Li, T. X. Wang, and X. H. Du, "Preparation of visible light-driven SnS_2/TiO_2 nanocomposite photocatalyst for the reduction of aqueous Cr(VI)," *Separation and Purification Technology*, vol. 101, pp. 11–17, 2012.

[17] D. W. Chen and K. R. Ajay, "Removal of toxic metal ions from wastewater by semiconductor photocatalysis," *Chemical Engineering Science*, vol. 56, no. 4, pp. 1561–1570, 2001.

[18] L. Qi, H. Li, and L. Dong, "Simple synthesis of flower-like ZnO by a dextran assisted solution route and their photocatalytic degradation property," *Materials Letters*, vol. 107, pp. 354–356, 2013.

[19] L. Mohapatra and K. M. Parida, "Zn-Cr layered double hydroxide: visible light responsive photocatalyst for photocatalytic degradation of organic pollutants," *Separation and Purification Technology*, vol. 91, pp. 73–80, 2012.

[20] J. Hirayama, R. Abe, and Y. Kamiya, "Combinational effect of Pt/$SrTiO_3$: Rh photocatalyst and SnPd/Al_2O_3 non-photocatalyst for photocatalytic reduction of nitrate to nitrogen in water under visible light irradiation," *Applied Catalysis B: Environmental*, vol. 144, pp. 721–729, 2014.

[21] D. Dimitrakopoulou, I. Rethemiotaki, Z. Frontistis, N. P. Xekoukoulotakis, D. Venieri, and D. Mantzavinos, "Degradation, mineralization and antibiotic inactivation of amoxicillin by UV-A/TiO_2 photocatalysis," *Journal of Environmental Management*, vol. 98, no. 1, pp. 168–174, 2012.

[22] M. Chen and W. Chu, "Degradation of antibiotic norfloxacin in aqueous solution by visible-light-mediated C-TiO$_2$ photocatalysis," *Journal of Hazardous Materials*, vol. 219-220, pp. 183–189, 2012.

[23] S. Yahiat, F. Fourcade, S. Brosillon, and A. Amrane, "Removal of antibiotics by an integrated process coupling photocatalysis and biological treatment—case of tetracycline and tylosin," *International Biodeterioration & Biodegradation*, vol. 65, no. 7, pp. 997–1003, 2011.

[24] D. Nasuhoglu, A. Rodayan, D. Berk, and V. Yargeau, "Removal of the antibiotic levofloxacin (LEVO) in water by ozonation and TiO$_2$ photocatalysis," *Chemical Engineering Journal*, vol. 189-190, pp. 41–48, 2012.

[25] N. A. Ramos-Delgado, M. A. Gracia-Pinilla, L. Maya-Treviño, L. Hinojosa-Reyes, J. L. Guzman-Mar, and A. Hernández-Ramírez, "Solar photocatalytic activity of TiO$_2$ modified with WO$_3$ on the degradation of an organophosphorus pesticide," *Journal of Hazardous Materials*, vol. 263, pp. 36–44, 2013.

[26] J. Wang, W. Sun, Z. Zhang et al., "Preparation of Fe-doped mixed crystal TiO$_2$ catalyst and investigation of its sonocatalytic activity during degradation of azo fuchsine under ultrasonic irradiation," *Journal of Colloid and Interface Science*, vol. 320, no. 1, pp. 202–209, 2008.

[27] C.-H. Chiou and R.-S. Juang, "Photocatalytic degradation of phenol in aqueous solutions by Pr-doped TiO$_2$ nanoparticles," *Journal of Hazardous Materials*, vol. 149, no. 1, pp. 1–7, 2007.

[28] M. Stylidi, D. I. Kondarides, and X. E. Verykios, "Visible light-induced photocatalytic degradation of Acid Orange 7 in aqueous TiO$_2$ suspensions," *Applied Catalysis B: Environmental*, vol. 47, no. 3, pp. 189–201, 2004.